High sensitivity optical spectroscopy of plasma and gases

Peter Cermak

UNIVERSITÉ DE GRENOBLE

COMENIUS UNIVERSITY

THESE

Pour obtenir le grade de

DOCTEUR DE L'UNIVERSITE DE GRENOBLE
Spécialité Physique des materiaux

Préparée dans le cadre d'une cotutelle entre
L'UNIVERSITE DE GRENOBLE ET COMENIUS UNIVERSITY
BRATISLAVA

Arrêtés ministériels : 6 janvier 2005 - 7 août 2006

Présentée et soutenue publiquement par

ČERMÁK PETER

Soutenue le 1 Septembre 2010

SPECTROSCOPIE OPTIQUE DE HAUTE SENSIBILITE DANS LES PLASMAS ET LES GAZES

Thèse dirigée par **Romanini Daniele** et codirigé par **Veis Pavel**

JURY

M.	Noga Jozef	Professeur, CU (Bratislava)	Président
M.	Cacciani Patrice	CR-CNRS, PhLam (Lille)	Rapporteur
M.	Kovac Jaroslav	Professeur, STU (Bratislava)	Rapporteur
M.^{me}	Massines Françoise	DR-CNRS, (Perpignan)	Rapporteur
M.	Kassi Samir	CR-CNRS, SPECTRO (Grenoble)	Examinateur
M.	Romanini Daniele	DR-CNRS, SPECTRO (Grenoble)	Examinateur
M.	Veis Pavel	Professeur, CU (Bratislava)	Examinateur

Thèse préparée au sein du Laboratoire SPECTRO et de l' Ecole Doctorale
Physique de Grenoble

UNIVERSITÉ DE GRENOBLE

COMENIUS UNIVERSITY

THESE

Pour obtenir le grade de

DOCTEUR DE L'UNIVERSITE DE GRENOBLE
Spécialité Physique des materiaux

Préparée dans le cadre d'une cotutelle entre
L'UNIVERSITE DE GRENOBLE ET COMENIUS UNIVERSITY
BRATISLAVA

Arrêtés ministériels : 6 janvier 2005 - 7 août 2006

Présentée et soutenue publiquement par

ČERMÁK PETER

Soutenue le 1 Septembre 2010

SPECTROSCOPIE OPTIQUE DE HAUTE SENSIBILITE DANS LES PLASMAS ET LES GAZES

Thèse dirigée par **Romanini Daniele** et codirigé par **Veis Pavel**

JURY

M.	Noga Jozef	Professeur, CU (Bratislava)	Président
M.	Cacciani Patrice	CR-CNRS, PhLam (Lille)	Rapporteur
M.	Kovac Jaroslav	Professeur, STU (Bratislava)	Rapporteur
M.^{me}	Massines Françoise	DR-CNRS, (Perpignan)	Rapporteur
M.	Kassi Samir	CR-CNRS, SPECTRO (Grenoble)	Examinateur
M.	Romanini Daniele	DR-CNRS, SPECTRO (Grenoble)	Examinateur
M.	Veis Pavel	Professeur, CU (Bratislava)	Examinateur

Thèse préparée au sein du Laboratoire SPECTRO et de l' Ecole Doctorale
Physique de Grenoble

Remerciements

Je voudrais exprimer ma gratitude à toutes les institutions et projets qui ont soutenu le projet de cette thèse: l'Ambassade de France en Slovaquie, l'Association EURATOM CU[1], le projet EU- QUASAAR, le projet ANR MIREV, le projet APVV-0544-07 et le projet VEGA 1/0609/08.

Mes remerciements vont aussi aux membres du Laboratoire de spectrométrie physique et au Département de physique expérimentale qui m'ont accueilli pour réaliser ce travail, notamment à mes plus proches collègues et à mes directeurs de thèse Pavel Veis et Daniele Romanini.

Enfin je remercie toute ma famille pour m'avoir soutenu tout au long de mes études, surtout à mon épouse Kristina pour son immense patience et le soutien qu'elle m'a accordés.

[1]Le contenu de cette publication est de la seule responsabilité de ses éditeurs et il ne représente pas nécessairement les vues de la Commission de l'UE ou de ses services.

Préface

La Spectroscopie optique constitue l'un des outils de diagnostic les plus importants du domaine de la physique. La capacité de non-interférence dans les expériences et la vaste gamme de schémas de détection permettent des applications dans une variété d'expériences. En particulier, le développement récent des technologies de semi-conducteurs et de micro-fabrication repousse les limites expérimentales offrant des détecteurs meilleurs et plus rapides comme les nouveaux types de capteurs d'image (par exemple les détecteurs à couplage de charge intensifiées ou avec électrons multipliés) ou de sources de lumière comme un laser aux puits quantiques à base d'antimoine. Cela permet d'obtenir une couverture de spectres plus larges ou d'acquisitions plus rapides en gardant ou même en augmentant le rapport de signal sur bruit.

Le travail de thèse a été réalisé dans le cadre d'une cotutelle entre le *Département de Physique Expérimentale* à l'Université Comenius à Bratislava et le *Laboratoire de Spectrométrie Physique* à l'Université Joseph Fourier à Grenoble. Le but de la thèse était le développement et l'application de nouvelles méthodes spectroscopiques pour l'analyse de plasma et de gaz.

A Bratislava, mon travail était supervisé par le professeur Pevel Veis et le docteur Peter Macko. Il s'est orienté vers le diagnostic optique de plasma. Mon travail principal a été d'étudier le comportement de la décharge à barrière diélectrique (DBD) ainsi que la production d'oxygène dans l'état singulet. En parallèle, j'ai développé des méthodes de mesure des propriétés physiques liées à cette expérience. Dans le DBD, l'objectif était de décrire l'évolution temporelle des états électroniques excités au cours de la décharge. La méthode utilisée était la spectroscopie rapide à large bande. Mon travail a consisté à

mettre en place l'instrumentation ainsi que les algorithmes pour le traitement de données. Concernant l'étude de la production de l'oxygène singulet, on a développé un système CRDS (Cavity-Ring-Down Spectroscopy) capable de le détecter dans la post-décharge de plasma.

A Grenoble, sous la supervision du docteur Daniele Romanini, l'objectif principal de mon travail a consisté dans le développement d'une nouvelle source laser - Vertical External Cavity Surface Emitting Laser (VECSEL) et son application dans la spectroscopie d'absorption. Le travail a été réalisé en collaboration avec *l'Institut d'électronique du Sud* dans le cadre du projet ANR MIREV. En plus de ce travail, j'ai participé au développement d'un détecteur portable et bon marché pour l'analyse quantitative de NO_2 et NO_3 dans l'atmosphère par la technique Incoherent Broadband Cavity Enhanced Absorption Spectroscopy.

Le premier chapitre présente un aperçu des lois physiques fondamentales et des formalismes représentant la base pour la compréhension des principes et des idées de techniques spectroscopiques de haute sensibilité. À la fin du chapitre deux applications spectroscopiques la détection de l'oxygène singulet par CRDS et la détection de NO_2 et NO_3 par IBB-CEAS sont décrites plus en détail afin de fournir à la fois une application de la théorie décrite et une présentation des projets auxquels j'ai participé.

Le deuxième chapitre parle de la spectroscopie de la DBD. La théorie basique de la décharge à l'égard de ses applications possibles est présentée afin de fournir la motivation pour le travail. Dans une deuxième partie le dispositif expérimental ainsi que les méthodes de diagnostic sont discutés. Dans la dernière partie les résultats obtenus sont présentés et discutés. Le dernier chapitre est consacré à l'élaboration d'un spectromètre VECSEL. Dans l'introduction, nous décrivons la motivation pour la spectroscopie dans la région de 2,3 mum ainsi que l'état actuel de la technique et des outils spectroscopiques pour cette gamme spectral. La description du développement du spectromètre VECSEL est décrite dans l'ordre chronologique tel qu'il a été effectué au cours de la thèse. A la fin, nous parlons du principe de fonction-

nement et des exemples d'applications de l'appareil.

Preface

Optical spectroscopy represents one of the most important diagnostic tools in physics. The capability of non–interfering measurements together with the vast range of detection schemes allow applications in a variety of experiments. Notably the progressing development in the semiconductor technologies and micro–fabrication pushes the experimental limits offering better and faster detectors like the new types of imaging arrays (e.g. intensified or electron multiplied charge coupling detectors) or light sources like Sb–based multi-quantum well lasers. This allows achieving broader spectral coverages or faster acquisition times by keeping or even increasing the signal to noise ratio.

The project of this thesis was developed as a joint supervision project between the *Department of Experimental Physics* at Comenius University in Bratislava and *Laboratoire de Spectrometrie Physique* at Joseph Fourier University in Grenoble. The aim of the project is the development and application of some of these new spectroscopic methods for the study and diagnostics of gases and plasma. Both laboratories have large experience in the development and application of the optical spectroscopy techniques.

In Bratislava the work under the supervision of prof. Pavel Veis and Doc. Peter Macko was oriented towards the optical diagnostics of plasma environments. Beside the principal experiments concerning the dielectric barrier discharge (DBD) and production of the singlet oxygen state, the goal was to develop spectroscopic methods capable of providing physical measurements related to this applications. In the DBD the interest was focused on the description of the excited electronic states population variations during the period of discharge. We used fast broad–band emission spectroscopy (FEBS)

comprising the instrument and data treatment process to achieve this goal. In case of singlet oxygen production we developed a Cavity ring–down spectrometer (CRDS) to detect the singlet oxygen by its infrared absorption in the microwave plasma afterglow.

In Grenoble under the supervision of Dr. Daniele Romanini the principal line of work consisted in the development of a new laser source — Vertical external cavity surface emitting laser (VECSEL) and its application to absorption spectroscopy. The work was held in collaboration with the *Institude d'electronique du Sud* in the frame of the joint ANR MIREV project. A period was also dedicated to the developing of a small, fast, robust and low–cost NO_2 and NO_3 detector based on the Incoherent broad–band cavity enhanced absorption spectroscopy (IBB–CEAS).

The first chapter presents an overview of basic physical laws and formalisms creating the background for understanding the principles and ideas of high–sensitivity spectroscopic methods. At the end of the chapter are two spectroscopic applications: singlet oxygen detection by CRDS and IBB–CEAS detection of NO_2 and NO_3 are described in more detail to provide both an application of the discussed theory and a presentation of the project where I participated.

The second chapter deals with the spectroscopy of the DBD. The basic theory of the discharge with respect to its possible applications is presented to provide the motivation for the work. In a second part the experimental setup together with the diagnostic methods are discussed. In the last part the obtained results are presented and discussed.

The last chapter is dedicated to the development of a VECSEL-based spectrometer. In the introduction we describe the motivation for the spectroscopy in the 2.3 μm region as well as current state of the art of the spectroscopic methods and tools in this part of spectra. The description of the VECSEL-based spectrometer development is written in the chronological order as it was performed during the thesis. At the end we discuss the operation principle and examples of applications of the spectrometer.

Contents

List of Figures

List of Tables

Chapter 1

High sensitivity spectroscopy

1.1 Introduction

The basic concept of an optical spectroscopy (OS) experiment (Fig. 1.1) consists in retrieving the dependence of detected light intensity on its frequency - spectrum. Subsequently by analysing the acquired data individual spectral features are attributed to related physical processes (abundance of interacting atoms and molecules, their internal structure, temperature, *etc.*). This is done by sampling the light according to frequency either in space (by diffraction, dispersion, *etc.*) or in time (using frequency tuned monochromatic source, frequency filtering, Fourier transform, *etc.*), before or after the interaction with studied element.

Most of the experiments can be classified into two groups with respect to the origin of detected radiation. In the *emission spectroscopy* (ES) the goal is to detect photons radiated from the sample during the process of de–excitation. The emitted photons then usually manifest in the spectra as positive signal structure. The principle of the second case – *absorption spectroscopy* (AS) is in the measurement of variations in light beam, originated independently on studied sample, due to the interaction with species of interest along the beam path.

The processes of absorption and emission of radiation (between two electronic states a and b) are closely related. According to Einstein there are three ways how this interaction may occur: spontaneous emission ($b \rightarrow a + h\nu$), stim-

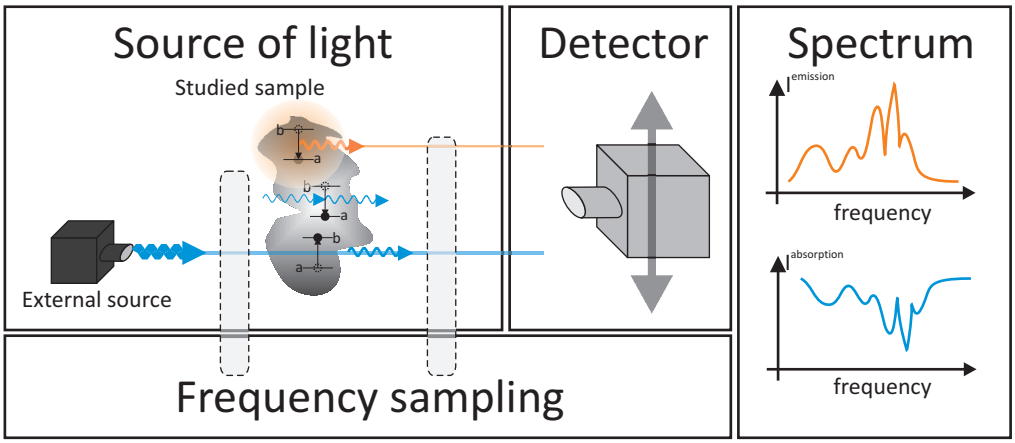

Figure 1.1: Principles of optical spectroscopy.

ulated (or induced) emission ($b + h\nu \rightarrow a + 2h\nu$) and absorption ($a + h\nu \rightarrow a$). The interactions rates $R_{interaction}$ (in s^{-1}) are described by the Einstein coefficients and in case of absorption and stimulated emission also by the spectral energy density of interacting radiation $\rho_\nu(\nu)$ [17]:

$$R_{spon.em.} = A_{ba} \tag{1.1}$$

$$R_{stim.em.} = B_{ba} \cdot \rho_\nu(\nu) = \frac{c^3}{8\pi h\nu^3} A_{ba} \cdot \rho_\nu(\nu) \tag{1.2}$$

$$R_{abs.} = B_{ab} \cdot \rho_\nu(\nu) = \frac{c^3}{8\pi h\nu^3} \frac{g_b}{g_a} A_{ba} \cdot \rho_\nu(\nu) \tag{1.3}$$

c is the speed of light and g_a and g_b represent the energy degeneracy factors of the states a and b. The total amount (from all emitters N_b to all wavelengths and whole space) of spontaneously emitted power from the system is then

$$P_{b\rightarrow a}^{emitted} = N_b \cdot A_{ba} \cdot h\nu_{ba} \tag{1.4}$$

Experimentally the quantity we detect is the intensity of radiation – irradiance [$W.m^{-2}$]. It is the incident radiation power per unit of detector surface. The relation between the radiated power and measured intensity $I^{det}(\nu)$ as a function of frequency is however not straightforward. Spectrally, the single emission 1.4 does not represent a delta function (or "stick") on frequency scale.

It forms a peak with given width. This line shape $\Phi(\nu - \nu_{ba}, \dots)$ depends on the emitter but also on the parameters of surrounding environment. Another complications arises from the detection process itself. It is the spatial coupling C_Ω describing the fraction of total emitted power towards the detector and the coupling efficiency $C_{eff.}$ representing the probability of a photon arriving to the detector surface, to be detected. The C_Ω coefficient depends mainly on the geometry of the optical setup. In most ES experiments it does not depend on frequency and is linearly proportional to $P^{emitted}$. For example when considering an emission from a point source to planar detector covering the solid angle Ω and deviated from the incident beam by an angle θ the C_Ω is equal to $\cos\theta \cdot \Omega/4\pi$ assuming a Lambert cosine law. The coefficient $C_{det.}$ unlike C_Ω is strongly dependent on the frequency ($C_{det.} = C_{det.}(\nu)$). It comprises the losses and perturbations (eg. convolution of emitted spectra with spectrometer frequency resolving function) on the way to the detector, during the sampling process of detection. So in general case we can $I^{det}_{b\to a}(\nu)$ express as

$$I^{det.}_{b\to a}(\nu) = C_{det.} \cdot C_\Omega \cdot P^{emitted}_{(b\to a)} \propto C_{det.}(\nu) \cdot n_b \cdot A_{ba} \cdot h\nu_{ba}\Phi(\nu) \tag{1.5}$$

A corresponding variable to $P^{emitted}$ in the AS measurements is the absorption coefficient α. It is the rate of radiation intensity decay when passing through the interacting environment measured in m^{-1} (or more commonly cm^{-1}). In case when the effect of absorption on the overall energy distribution in the sample is negligible (e.g. we excite only a small portion of low energy states – $n_b \ll n_a$) there is a linear dependence between absorption losses and path in the sample $\mathrm{d}I/\mathrm{d}x = -\alpha I$. The solution of this basic differential equation yields to the commonly written Beer-Lamber law

$$I = I_0 \exp\{-\alpha(\nu) \cdot L\} \tag{1.6}$$

The absorption coefficient is the product of the concentration of interacting elements n_b [molecule.cm^{-3}], transition strength S_{ba} [cm^{-1}/(molecule.cm^{-2})] and the normalized line shape function $\Phi(\nu - \nu_{ba}, \dots)$ [1/cm^{-1}]. The product $\Phi \cdot S_{ba}$

is also for its unit called the cross–section $\sigma[\mathrm{cm}^2]$. The relation with the Einstein coefficient is defined in the radiative transfer theory [66]

$$S_{ab} = \frac{h\nu_{ba}}{c}\frac{n_a}{n}\left(1 - \frac{g_a}{g_b}\frac{n_b}{n_a}\right)B_{ab} \tag{1.7}$$

where n_a and n_b are the populations of the lower and upper states, respectively, g_a and g_b are the state statistical weights, and n is the molecular number density. Similar to the ES case we need to take into account the detector efficiency $C_{det.}$ and coupling factor C_Ω

$$I^{det.} = C_\Omega \cdot C_{det.}(\nu) \cdot I^{absorption}_{(b\leftarrow a)} = C_\Omega \cdot C_{det.}(\nu) \cdot I_0 \exp\{-\alpha(\nu) \cdot L\} \tag{1.8}$$

Analysing the equations (1.5), (1.8) and the associated relations we see in both cases components representing elements concentrations and probabilities of interaction. This leads to the main applications of OS – the detection of known species concentration and probing their internal structure (energy levels, cross–sections, *etc.*). Consecutively an information about physical properties of the environment as well as the character of matter–light interaction may be deduced through their influence on measured quantities (e.g. through different line shapes). In both equations the main problem lies in the reduction of measurement influence $C_{det.}$ and C_Ω while loosing minimum information from the original signal.

Emission spectroscopy offers a very versatile tool with minimal or no requirements on observed processes – we need only access to the emitted radiation. This allows to make the interaction–free measurements. The data retrieval looks easier than in AS case where we have one additional variable to determine – the interaction length L. On the other hand after more detailed examination we find that situation is quite complicated. The ES addresses directly only the excited states of matter therefore limiting the choice of study. Moreover the ES does not have control over the emission signal (the probability of spontaneous emission 1.1 does not depend on any physical property of environment only on the internal structure of radiant) making it difficult to

apply in low energy environments (like gases) without any other interaction (excitation by discharge, plasma, *etc.*). In reality the estimation of $C_{det.}$ and C_Ω is almost never exact and requires calibration to known parameters of the system – e.g. by measuring emission for known concentration of elements.

Consequently in most experiments the best we achieve to retrieve is a value only proportional to the emitted power $P^{emitted}$. Also the lack of information about the ground states needs to be often compensated by measurement of emissions radiating from most of the abundant excited states. This puts another requirements onto the optical scheme and detectors because of the increased spectral bandwidth and often also limited recording time. As a consequence when developing the high sensitive instruments for ES the role of the optical coupling–C_Ω and the detector–$C_{det.}$ is crucial and usually is discussed more deeply than in AS case.

The reason for relatively low importance of C_Ω and $C_{det.}$ in AS lies in additional factor of absorption spectroscopy–the probing light used to interact with matter. Although it brings a higher complexity of the optical scheme it also provides the possibility to perform absolute measurements and to enhance absorption by increasing the interaction path L. Measuring the absorption along the same path with and without the absorbent ($exp(-\alpha L) \approx 1$) the factor $C_\Omega \cdot C_{det.}(\nu) \cdot I_0$ may be estimated quite precisely. With the knowledge of L one can than retrieve the absolute value of absorption. Correspondingly the information such as concentration of absorbent may be retrieved from a single line measurement. In absorption spectroscopy the amount of absorption signal could be directly moderated by the interaction path L or if possible wisely selecting the probing beam frequency to match transitions with different probabilities of absorption. This allows adapting the technique for different levels of absorption. In conclusion to achieve high sensitivity measurements in AS except the reduction of the noise level of detection the main care is given to the probing beam and the interaction path through the studied sample.

In the following text I address some of high sensitive methods both from AS and ES fields each exploiting different combinations of sensitivity enhancing

principles. In the first part the simultaneous and fast acquisition of a broad spectrum is used to enhance the description of time dependant radiating processes like pulsed plasma. In the second part the effect of a high finesse (HF) Fabry–Pérot resonators (FPR) on AS methods is discussed.

1.2 Fast–broadband emission spectroscopy

In the following text we shortly introduce some specific examples of the environments to be addressed by this method. They share a need for a tool that is able to cover a wide spectrum with a quite high resolution in a very limited time. We demonstrate the limited possibilities of standard spectroscopic tools (e.g. single grating or prism coupled with simple array detector) and describe in more detail equipment needed to fulfil the requirements set by the experiments.

The FBES method is often used to perform studies on the discharges like the dielectric barrier discharge (DBD) or the laser induced plasma (LIP). Both DBD and LIP are nowadays widely studied subjects ranging from basic research to commercial applications. Although the DBD and LIP are quite different with respect to both the physical properties and the aim of the experiments there are several common key parameters when discussing the properties of the emitted radiation. In both the energy is distributed over a large number of exited states. This produces rather complex and broad emission spectra. In figure 1.2 there are some common radiative transitions in DBD (N_2 ro-vibrational band-heads are taken from [30, 41][1] and Partidge et al. [64] in case of HIR transition) and in LIP (atomic transitions according to NIST [69]). To study the energy distribution in electronic states (DBD case) or stoichiometry of abundant elements (LIP) one need to acquire a representative part of the spectrum. This (see Fig.1.2) may cover several hundreds of nanometres from ultra–violet (UV) to near–infra–red (NIR) depending on the species present in the sample.

Another important parameter is spectral resolution. In a broad and dense spectrum we need to have a reasonable resolution to maintain the capability of unambiguous identification of spectral motives and properties. Measurement directly depending on spectral resolution are for example the determination of rotational temperature T_{rot} in DBD and the electron concentration n_e in LIP. DBD is an example of non–equilibrium environment where the energy distri-

[1] available online at http://web.ipac.caltech.edu/staff/laher/fluordir/fluorindex.html

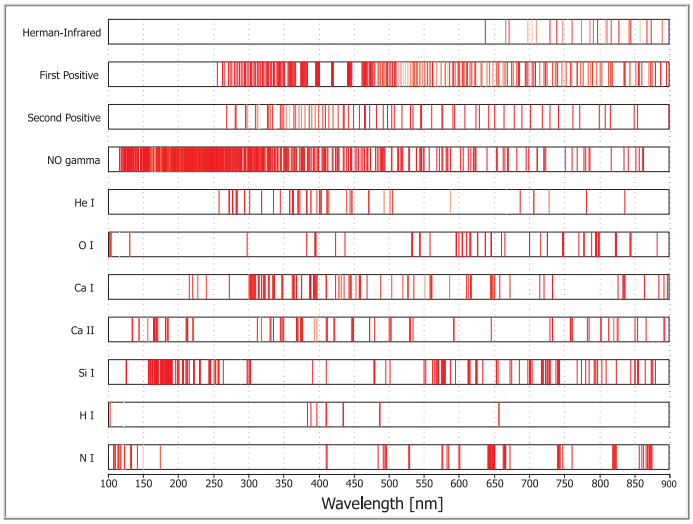

Figure 1.2: Position of some ro-vibrational electronic transitions in nitrogen and atomic emissions. The intensity of color represents the transition probability normalized within the band or states respectively.

bution does not follow the Boltzmann law for all elements (electrons, neutrals, ions). Instead, usually there may be selective equilibria within specific groups like electrons (described by electron temperature T_e), neutrals (T_g also known as kinetic gas temperature), vibrations and rotations of atoms in molecules ($T_{vib.}$ and $T_{rot.}$ respectively). T_{rot} is in most cases very close to the kinetic gas temperature T_g [60] thus often serves as probe for its estimation. The shape and structure of N_2 Second positive ro–vibrational band (2PS: $C\,^3\Pi_u - B\,^3\Pi_g$) is often used for the determination [8, 10] of T_{rot}. The figure 1.3-A shows example of the nitrogen 2PS simulated with different value of the spectral resolution ($\Delta\lambda$= 3, 0.3 and 0.03 nm) for a constant T_{rot} to point out the effect of resolution on the spectral motives of the band which directly influences the $T_{rot.}$ estimation.

Another example of the importance of a sufficient resolution is the determination of plasma electron density n_e from Stark broadening of atomic lines in LIBS experiments [4, 31]. The broadening (and a shift of the peak wavelength) is produced due to the collisions between radiating atoms and charged particles (ions and electrons) [31]. In the case of isolated spectral lines of non-

hydrogenic neutral atoms and ions the broadening could be estimated from relation $w_{Stark} = wn_e$ [4] where w is the electron-impact constant. On the figure 1.3-B there is an estimation of broadening for several Ar lines often used for n_e estimation based on electron-impact constants from Cadwell et al. [9] and common n_e values in LIBS experiments [4]. From both images one could understand the need for resolutions at least below 1 nm at 700 nm (Ar lines) and below 0.1 nm at 300 nm (2PS).

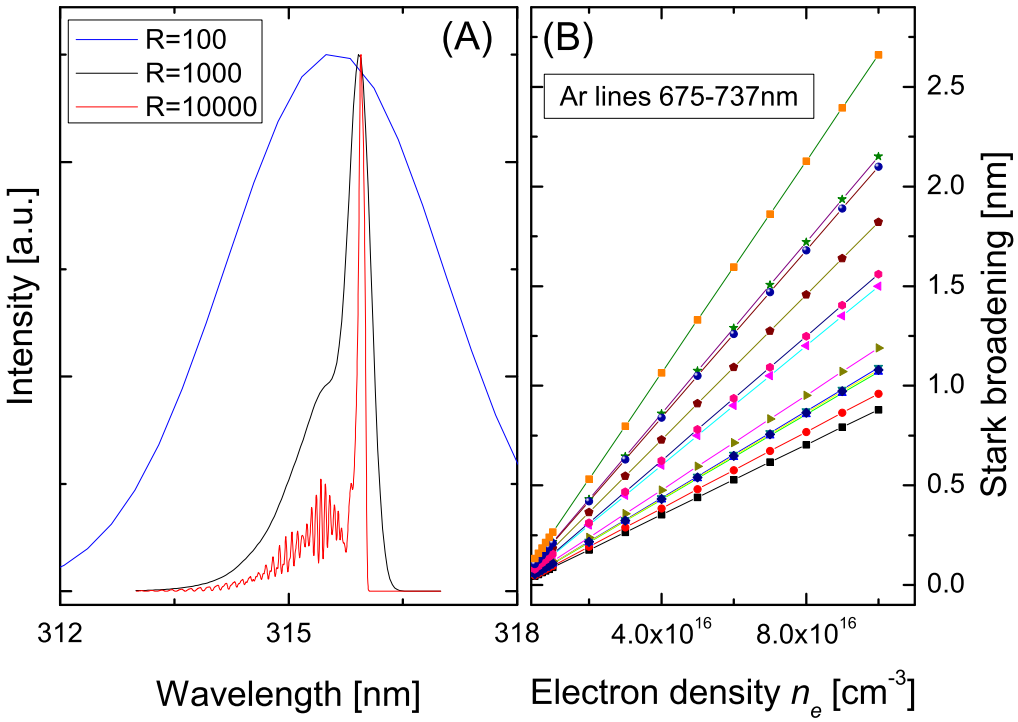

Figure 1.3: 2PS simulated for a constant rotational temperature with different spectral resolutions $\Delta\lambda$= 3, 0.3 and 0.03 nm (A). The value of Stark broadening for some Argon lines in function of the electron concentration (B).

Finally the last aspect to discuss is the temporal character of DBD and LIP. Figure 1.4-A shows the evolution of DBD current as a function of voltage period and figure 1.4-B the duration of a standard Nd:Yap pulse laser used in LIP. Both processes occurs on micro-second time scale. We can estimate the necessary time resolution for sampling around 100 ns to 1 μs.

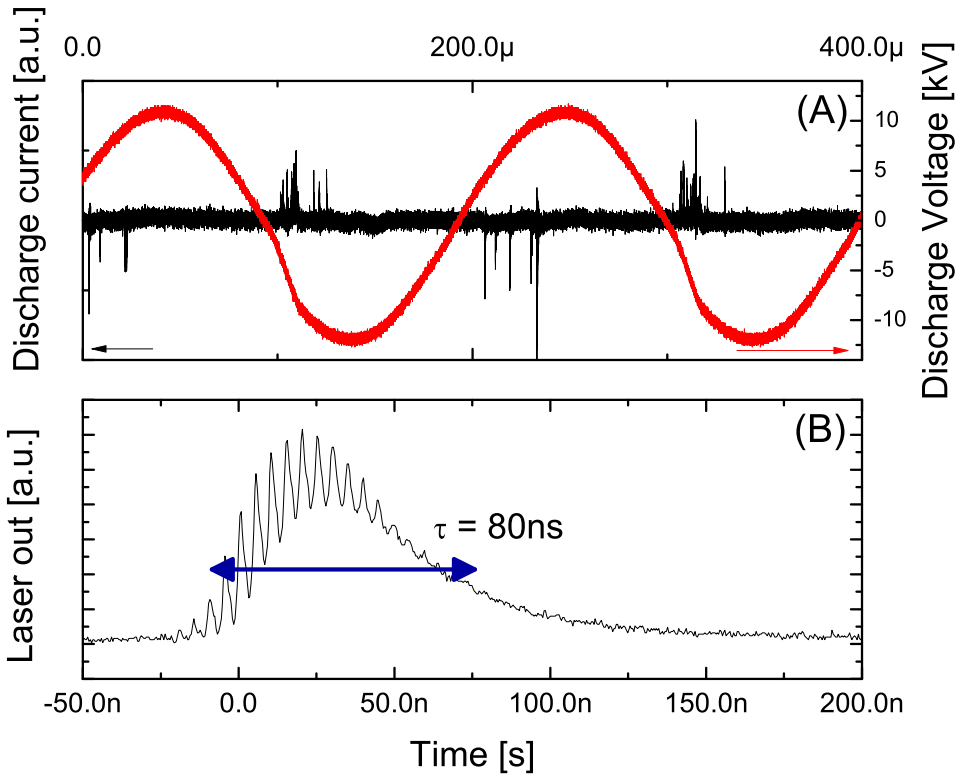

Figure 1.4: Example of laser pulse duration in LIBS experiments (A) and the discharge current in DBDs (B).

These conditions on spectrum width, resolution and timing limits the use of standard elements used in optical spectroscopy. The time dynamics of processes we want to study basically excludes the temporal frequency sampling of the spectra (e.g. Fourier transform spectroscopy). Also in low–light imaging it is preferable to have only a single instrument to analyse whole spectra. The reason is to not reduce and waste the signal by splitting it over many channels (e.g. by beam splitter) where in each channel we exploit only a given part of spectra and the rest is lost (e.g. using several gratings each for given part of spectra). To summarize we need a single dispersing element which covers efficiently a broad range (200-1000 nm) with good resolution (around 1 nm at 1000 nm and 0.1 nm at 200 nm) coupled to a low–noise detector array capable fast triggering and gating.

1.2.1 Detector

In a spectrometric system the choice of detector has a critical impact on the measurement capabilities. With respect to the presented demands both for spatial acquisition (recording the wide spectra) and timing (one shot measurements) we limit the discussion to the array–like detectors based on photoelectric conversion.

Each element of such array is a diode photo–sensor (pixel). There the radiation (containing number of incident photons n_{ip}) is transformed into photo–electrons (n_{pe}) and stored in the coupled charge storage region. Depending on the read–out architecture we recognize either charge coupled devices – *CCD* or complementary metal oxide semiconductor – *CMOS*. In CCDs the read–out of the accumulated charge is performed sequentially (pixel by pixel) by a single read–out amplifier (for all pixels). In CMOS each pixel has its own amplifier allowing the parallel read–out. The price for the parallel read-out capability is the different gain, linearity and noise level of each amplifier. This is the reason that currently in the scientific applications where the high accuracy is needed the CCDs dominates over CMOS[2] [1]. During the fifty years of development in the field of CCDs their performance pushed the boundaries in the quantum efficiency D_{QE} of light detection (n_{pe}/n_{ip} over 90% for back–illuminated CCD) and in reducing the noise from either dark signal or amplifier read–out (below 10 e^-). There are two main drawback of the architecture regarding the use of CCD in FBES.

The first drawback is the signal to noise ratio (SNR) when detecting a weak radiation. In such case the induced charge is below the read–out noise thus the SNR falls bellow 1. There are two main solutions how to enhanceg the CCD to overcome this problem. Both are based on the amplification of signal befor the read–out process (Fig. 1.5). In the electron multiplying CCD – *emCCD* accumulated charge is amplified in the multiplication register after being detected. The order of detection and amplification is switched in the

[2]Although this can be change with the arrival of new sCMOS architecture promising to overcome this limitations [12]

intensified CCD – *iCCD* where a intensification unit is placed on top of the CCD.

Second is the control over acquisition timing. In CCD this is driven by a given read clock waveform which controls sequential readout of stored charges. The highest rates are about 20 Mhz for scientific interline CCDs corresponding for a 1.3 megapixel sensor to 11 frames per second [12]. To assure the uniform exposure for each pixel either mechanic or electronic shutter is used. In case of mechanical shuttering the minimum integration time is around 1 ms. In CCDs the electronic shuttering exploits the parallel readout buffer to stock the charge prior to readout allowing faster gating down to $1/16000$ s depending upon CCD architecture [2]. The best solution is implemented in the iCCD camera.

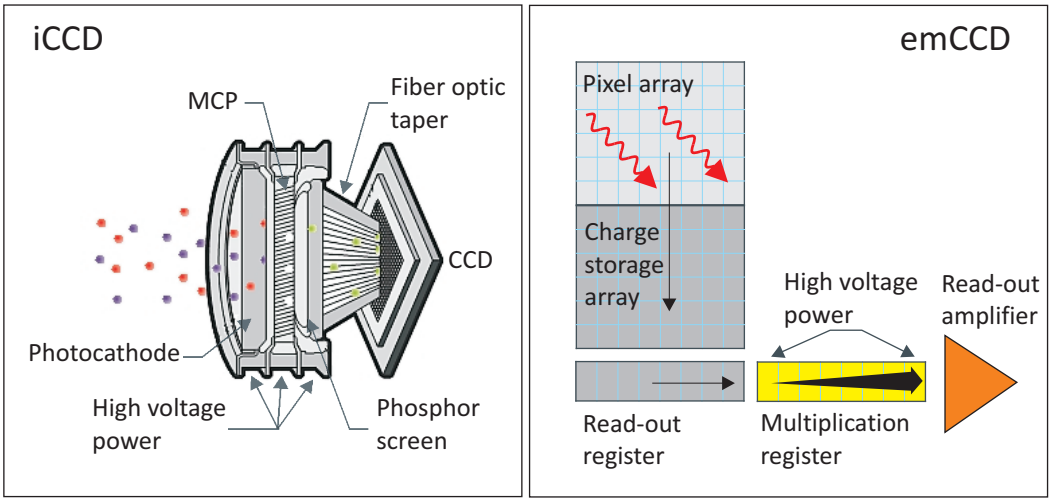

Figure 1.5: The scheme of iCCD and emCCD according to [1].

The reason of its fast and efficient gating consists in the architecture of the intensifier tube which comprises the photo–cathode, microchannel plate (MCP) and a phosphor screen (Fig. 1.5). The incoming photons hits the photo–cathod were they produce photo–electrons. These are drawn to the MCP by an electric field. The MCP is a thin disc (about 1 mm thick) with a form of honeycomb of glass channels, each with a resistive coating. The MCP has a high potential across it (500 to 1000 V) so that the photo–electron will cascade down the channel and produce secondary electrons (similar in principle to an avalanche photo-diodes). Exiting electron cloud is finally accelerated

across the small gap (∼0.5 mm) by a potential of several thousand volts where it strikes a phosphor coating producing photons to be detected by the CCD. To achieve efficient coupling to the CCD the phosphor is coated on the inside of a fibre tapper placed on the CCD. Since the photon transformation depends on the applied voltage the temporal control of this process (gating) is very precise down to nanosecond scale.

To compare the emCCD and iCCD in terms of sensitivity and noise we discuss their SNR. In amplifier devices the signal in photo-electron is expressed as

$$n_{pe} = A \cdot D_{QE} \cdot n_{ip} \tag{1.9}$$

where A is the amplification rate. The noise signal N created during the photo–conversion has five main sources [1, 20]:

- *Shot noise* – δ_{signal} or photon noise results from the inherent statistical variation of incidents photons. It follows the Poission statistic and therefore is equivalent to the square root of the number of detected photons ($\delta_{signal} = \sqrt{D_{QE} \cdot n_{ip}}$).

- *Dark noise* – δ_{dark} is thermally induced noise arising from the variations of thermally generated electrons (dark current) in the detector independently of photon-induced signal. Similarly to Shot noise Dark noise follows Poisson statistics therefore is equivalent to the square-root of the number of thermal electrons generated within the image exposure time. Level of this noise depend highly on temperature and could be significantly reduced by cooling the device.

- *Noise factor* – F comes as additional noise from amplification (ideal amplifier has noise factor equal to 1)

- *Spurious noise* – δ_s is due to the charge transfer (pixel to storage, storage to read–out register, *etc.*) on detector prior to read–out

- *Readout noise* – δ_{read} is a combination of system noises relied to the processes of electrons to voltage (read–out) and analog-to-digital (A/D)

	Ideal detector	CCD	emCCD	iCCD
Quantum eff.	100%	93%	93%	50%
Read–out noise	0	10	60	20
Amplification	1	1	1000	1000
Spurious noise	0	0.05	0.05	0
Dark noise	0	0.001	0.001	0.001
Noise factor	1	1	1.41	1.6

Table 1.1: Characteristic parameters for CCD, iCCD, emCCD and ideal array detector according to [1].

conversions

All these factors influence the total noise according their order in the photon transformation to digital signal. Realizing that, we can write the SNR equation as presented in [1]

$$\frac{S}{N} = \frac{A \cdot D_{QE} \cdot n_{ip}}{\sqrt{F^2 \cdot A^2 (D_{QE} \cdot n_{ip} + \delta_s^2 + \delta_{dark}^2) + \delta_{read}^2}} \tag{1.10}$$

To calculate this ratio for different cameras we use values given in [1] and written in table 1.2.1. Figure 1.6 shows the SNR dependence on the number of incidence photons. We see that in our range of interest – low light detection both iCCD and emCCD overcome CCD which is limited by its read–out noise. The emCCD also beats the iCCD mainly due to lower quantum efficiency of its photo cathode. Another disadvantage of the iCCD not mentioned before is the "degradation" of pixel size due to the resolution of the intensifier tube which is from 25 to 35 μm. As a consequence the smallest resolvable feature (i.e. the best case possible) on an iCCD will be approximately 1.5 to 2 times the pixel size of coupled CCD [1].

To conclude on one hand we have emCCD detectors with better SNR and resolution and on the other hand iCCD with ultimate gate controlling. The choice for the detector is often difficult to realize and further experimental requirements have to be taken into account to help to order the priorities. For example if we decide to observe DBD spectra evolution within one period, we would definitely need to gate in hundreds of nanoseconds thus the iCCD would

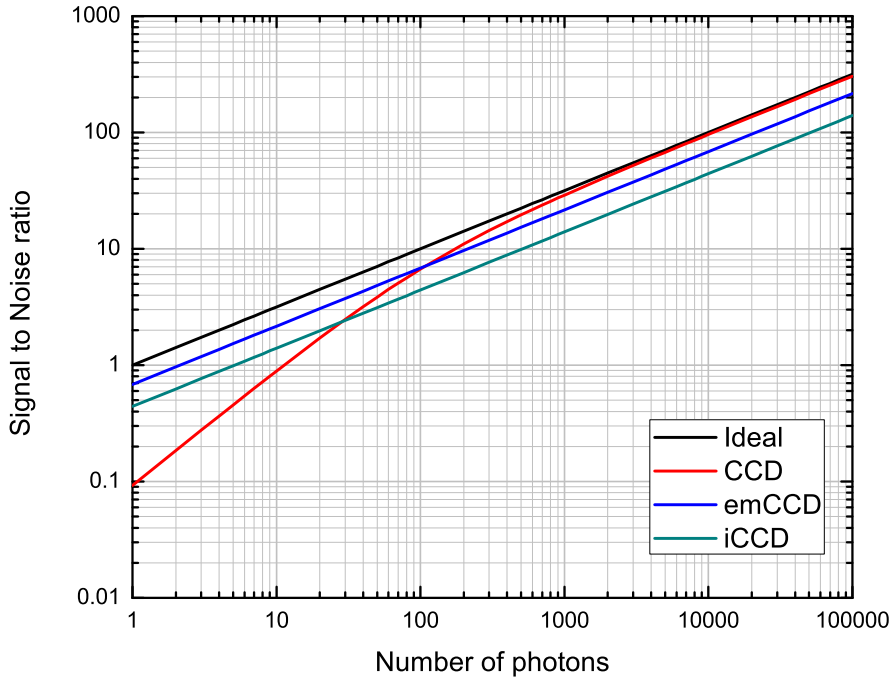

Figure 1.6: Theoretical comparison of SNR for different array detectors calculated from equation 1.10.

be the choice. Another inspiration may come from previous experiments where different camera were compared. For example Sabsabi et al. [77] compared gated CCD to iCCD in the spectrochemical analysis of metal alloys by LIP. They showed a better performance (in limits of detections) for iCCD.

1.2.2 Dispersion element

Taking the target spectral coverage (from 200-1000 nm) and resolution (0.1 nm for 200 nm) we can calculate the necessary parameters (pixel size and separation) for the detector in case of linear dispersion. A standard imaging array like CCD or CMOS may attain a physical size from 1 cm up to 5 cm (e.g. Hamamatsu C10000 TDI sensor). To plot a 800 nm wide spectrum we need a dispersion of 80 nm/mm (1 cm width) or 16 nm/mm (5 cm width). To ef-

ficiently exploit the detector the pixel distance should be about 3 times less than the spectral resolution. Taking the 0.1 nm for 200 nm we find that to fulfil this condition we need 2400 pixels/mm or 480 pixels/mm corresponding to pixel separation of 1.25 μm in 1 cm case or 6.25 μm for 5 cm image width. If we compare this dimensions to the standard pixel widths (from 6 μm to 20 μm) we find a very little coincidence. As a consequence to plot 800 nm in a single line onto a imaging array with sufficient resolution is almost impossible. The solution to this problem described in this work uses the effect of double-crossed dispersion. The idea is to exploit the whole imaging area of a matrix CCD detector (rather than just a linear array) by focusing the spectra in stripe-like regions stacked one above another. The created image in the form of ladder, in french *échelle*, gave the name to this type of spectrograph. The idea of such a spectrograph came from George R. Harrison [32]. He designed an instrument containing a grating with coarse and precise grove pattern used in wide angles and high diffraction orders (echelle grating) followed by moderate dispersion element to separate the overlapping diffraction orders (Fig. 1.7).

The groves of echelle grating (zoomed part of figure 1.7) have a step–like profile with only the steep side s illuminated. To assure the highest efficiency the angle of incidence α is equal to the blaze angle θ (beam is normal to the grove facet). As a consequence the dispersed radiation (with angle of dispersion β) is split into a number of diffraction orders in the narrow interval along the incidence angle ($\beta \simeq \alpha$) fulfilling the Littrow blaze condition [48].

In such a configuration the grating equation expressing the condition for positive interference between two parallel beams diffracted from two groves facets spaced by d has a form

$$m\lambda = 2d \sin \beta \tag{1.11}$$

In each order the maximum diffraction efficiency is achieved for β equal to the blaze angle θ. The corresponding wavelength (according to 1.11) is called the blaze wavelength λ_m^0

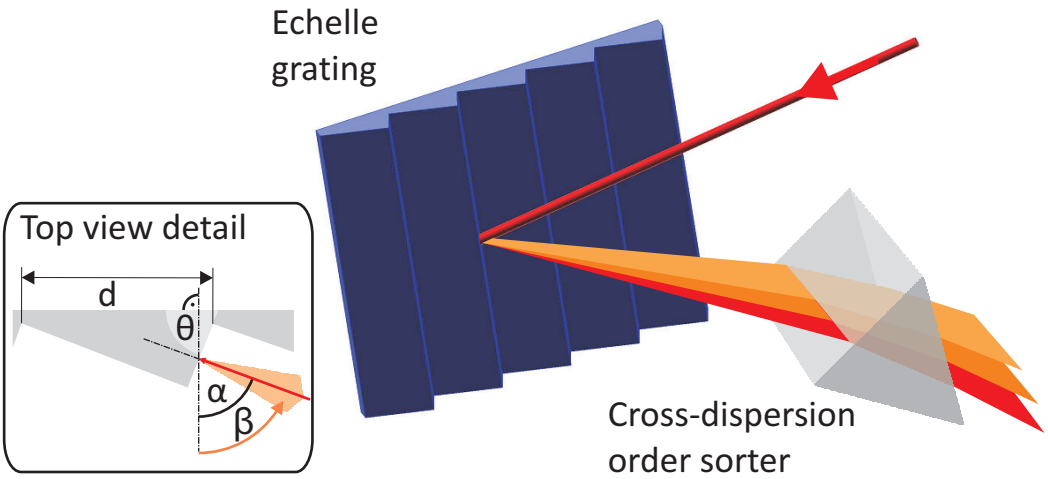

Figure 1.7: The principle of double-crossed dispersion in echelle spectrograph with detail of grove design used in Littrow blaze condition.

$$\lambda_m^0 = \frac{2d\sin\theta}{m} = \frac{2t}{m} \tag{1.12}$$

where $t = d\sin\theta$ is the projected width of the grove. Covering a broad spectral range by the use of multiple diffraction orders, each containing the central blaze wavelength is therefore a way to achieve relatively high diffraction efficiency across the whole spectral range (Fig. 1.8–a) compared to standard single order dispersion elements [47]. The relation between the λ_m^0 and the order spectral bandwidth δF_m^λ (Fig. 1.8–b) can be then found from the condition of the continuous spectral coverage $\lambda_m^{max} = \lambda_m^{min}$ and continuous spectra intensity $I(\lambda_m^{max}) = I(\lambda_m^{min})$ [19]

$$\delta F_m^\lambda = \frac{\lambda_m^0}{m\cdot[1-(2m)^{-2}]} \simeq \frac{\lambda_m^0}{m} \tag{1.13}$$

The resolving power R of the grating according to Rayleigh criterion (coincidence of the first diffraction minima for λ and diffraction maxima for $\lambda+\Delta\lambda$) is for a grating the product of the diffraction order m and the total number of

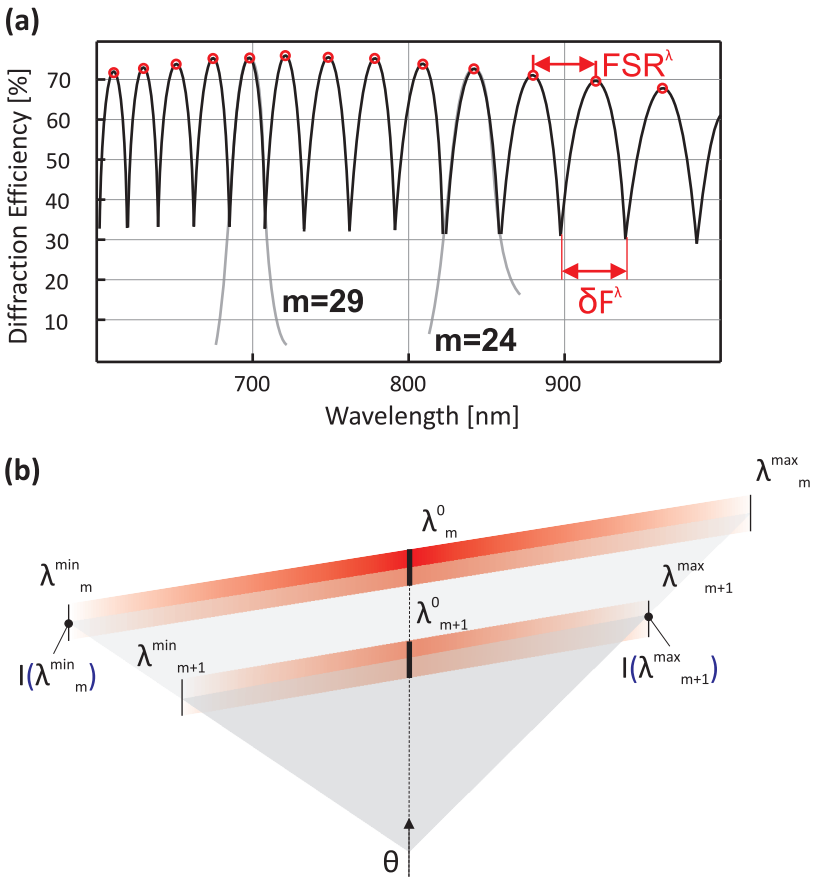

Figure 1.8: a – An example of the diffraction efficiency for echelle grating showing efficient broad spectral coverage. b – Two spectral segments of adjacent orders (m and $m+1$).

groves N. In echelle case this is equal to

$$R = 2W\frac{\sin\beta}{\lambda} \tag{1.14}$$

where we introduced the grating width $W = Nd$. Equation 1.14 shows that the resolving power for given wavelength depends fundamentally only on the grating width W and the diffraction angle β. Similarly we can show that the angular dispersion D and the linear dispersion L in the focal plane f depends

for given λ only β (and f in linear dispersion case):

$$D = \frac{\mathrm{d}\beta}{\mathrm{d}\lambda} = \frac{m}{d\cos\beta} = 2\frac{\tan\beta}{\lambda} \tag{1.15}$$

$$L = \frac{\mathrm{d}x}{\mathrm{d}\lambda} = fD = 2f\frac{\tan\beta}{\lambda} \tag{1.16}$$

In many cases the spectral resolution R_s does not attain the diffraction limit R. Instead it is determined by the size of the entrance aperture image in the focal plane – Δl_{ap}. Using the 1.16 we find the spectral width of the aperture $\Delta\lambda_{ap.}$

$$\Delta\lambda_{ap.} = \frac{\Delta l_{ap}}{L} = \frac{\Delta l_{ap}}{2f\tan\beta}\lambda \tag{1.17}$$

Realizing that the Δl_{ap} is constant for all wavelengths over the whole focal surface and β close to the blaze angle θ the spectral resolution R_s is to be found constant over the whole spectrograph range

$$R_s = \frac{\lambda}{\Delta\lambda_{ap}} = \frac{2f\tan\theta}{\Delta l_{ap}} \tag{1.18}$$

This property called CSR (constant spectral resolution) is unique for echelle spectrographs.

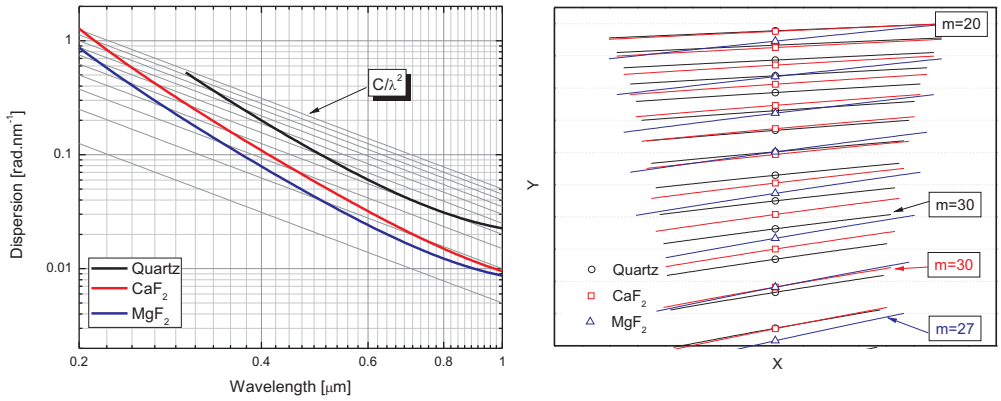

Figure 1.9: Calculated angular dispersion of equilateral prism for MgF_2, CaF_2 and Quartz and corresponding echelle double-crossed dispersion patterns (for groves density 52.13, blaze angle 32.35°) starting from order 20.

The second part of Echelle spectrograph is a dispersion element. In ideal case it should separate the overlapping orders unambiguously with a constant distance in crossed plane. Denoting $\beta_\perp$ the order–sorter dispersion angle the separation distance $l_\perp$ between two diffraction orders is

$$l_\perp = \frac{\mathrm{d}\beta_\perp}{\mathrm{d}\lambda} \cdot \delta F_m^\lambda \cdot f \simeq \frac{\mathrm{d}\beta_\perp}{\mathrm{d}\lambda} \cdot (\lambda_m^0)^2 \cdot \frac{f}{2d \sin\theta} \tag{1.19}$$

So $l_\perp$ would be close to constant if the crossed angular dispersion fulfilled relation $\mathrm{d}\beta_\perp/\mathrm{d}\lambda = C \cdot 1/\lambda^2$. This is very hard to achieve especially for broad ranges from UV to NIR. For example angular dispersion for the triangular prism (with prism angle ϵ, and index of refraction $n(\lambda)$) is

$$\frac{\mathrm{d}\beta_\perp}{\mathrm{d}\lambda} = \frac{\mathrm{d}\beta_\perp}{\mathrm{d}n}\frac{\mathrm{d}n}{\mathrm{d}\lambda} = \frac{2\sin(\epsilon/2)}{\sqrt{1 - n^2 \sin^2(\epsilon/2)}}\frac{\mathrm{d}n}{\mathrm{d}\lambda} \tag{1.20}$$

Figure 1.9 shows calculated angular dispersion for equilateral prism ($\epsilon = 60°$) composed of some common materials used in optics (MgF_2, CaF_2 and Quartz). The linear curves on the background represent the ideal function $C \cdot 1/\lambda^2$. Corresponding echelle double-crossed dispersion patterns (according to from 1.16 and 1.19) are plotted on the right. We see that principal problem arises from orders "compression" in vertical scale and stretching in the horizontal the infra–red region. Because of the limited dimensions of imaging arrays we usually find this as the practical limit when trying to achieve both high resolution and broad spectral coverage.

There are several ways how to circumvent or at least reduce these limitations. Figure 1.10 shows some of commercially available solutions Mechelle5000 from Andor, S200 from Cattalinasci and ESA4000 from LAA. Their main parameters and performance as taken from their specification sheets are listed in table 1.2.2. All of them are of short focal length (around 200 mm) destined for compact laboratory use. Compared to described theoretical model the real systems contain additional corrective optics to assure equal imaging at whole focal plane. Principal differences between the spectrographs consist in handling the cross-dispersion problem. Mechelle uses a double prism achieving

almost constant separation of orders (see Fig. 1.11) in other two cases a double passage through prism is used. The result is a broad coverage with reasonable resolution. The highest resolution is achieved by the ESA4000. The price is a half of coverage compared to Mechelle. Opposite is the S200 spectrograph with widest coverage but poorest resolution.

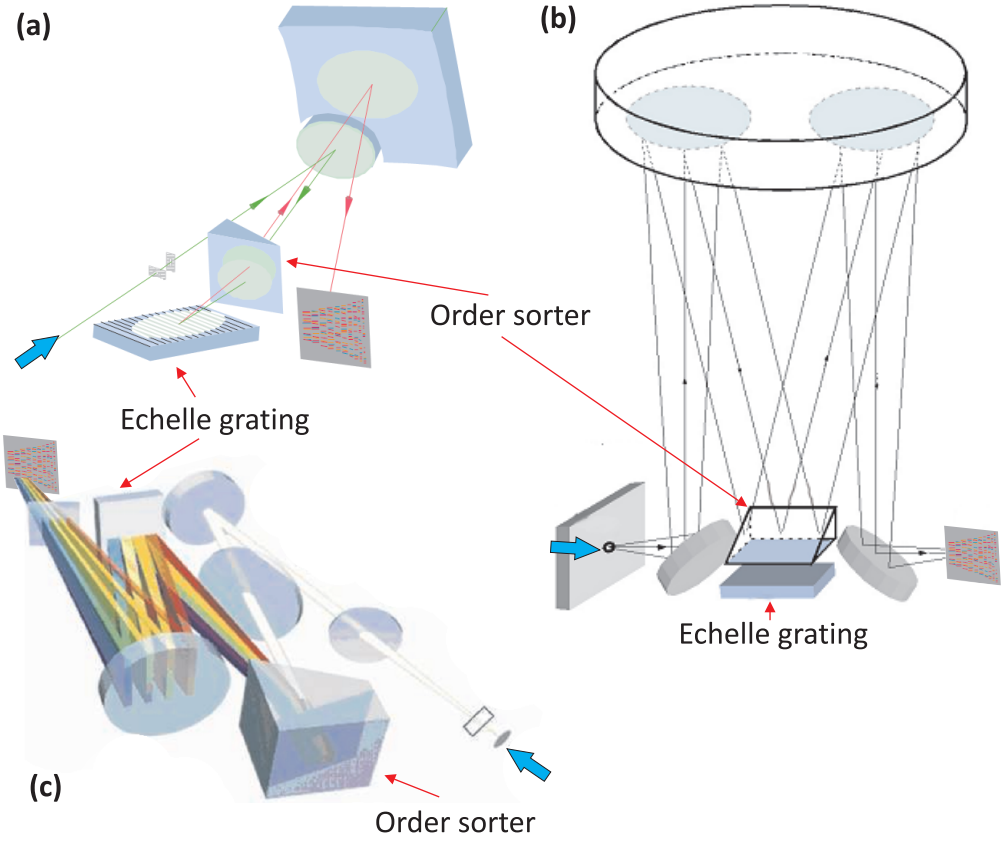

Figure 1.10: Optical design of some commercial echelle spectrographs with parameters described in table 1.2.2. a–ESA4000 , b–S200, c–Mechelle5000.

1.2.3 FBES measurement

In the last section we describe the process of the emitted spectra ($\sim P^{emitted}$) retrieval from the recorded signal. This operation – calibration is strictly device and environment depending and in case of high sensitivity – low noise operation needs to be repeated for each measurement. Especially in case of echelle spectrograph where the pattern formed in the focal plane (on the array

Model	focal[mm]	Coverage[nm]	Resolution
Mechelle 5000$^{\diamond}$	195	200–975	5000
S200*	200	190–1100	3100
ESA 4000†	250	200–780	13000

$^{\diamond}$ Andor Technology plc., http://www.andor.com
* version HO, Catalina Scientific Corp., http://www.catalinasci.com
† LLA Instruments GmbH., http://www.lla.de

Table 1.2: Parameters of some commercial echelle spectrographs.

detector) is quite temperature depending. Generally we distinguish between frequency (X–scale) and intensity (Y–scale) calibration. In this work we used the Andor Mechelle5000 spectrograph coupled with ICCD istar camera. The spectrometer is operated by provided software which also handles the reconstruction of spectra. The exact position of the 2D spectra pattern in focal plane is adjusted by calibrations to emission lines (Fig. 1.11).

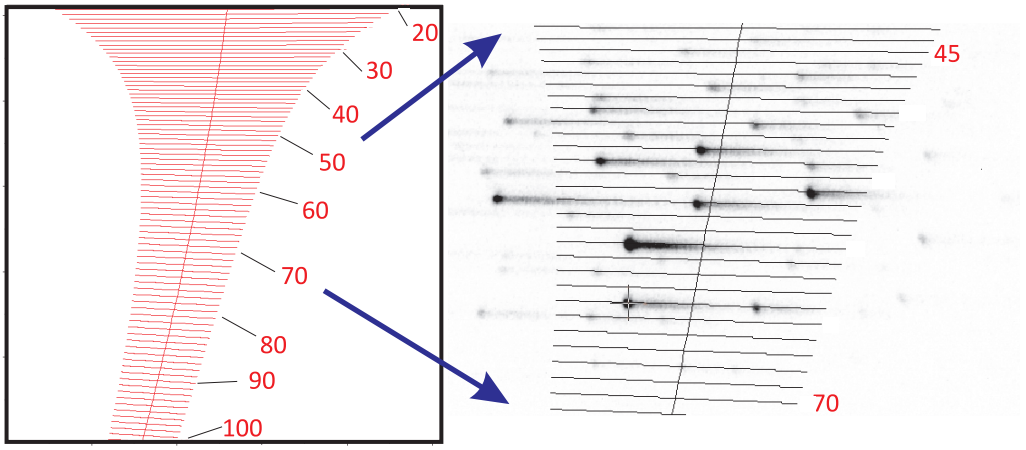

Figure 1.11: Retrieval of the recorded spectra in the Andor Mechelle 5000 spectrograph. The orders distribution on the array is on the left side and on right the example of real spectra.

To obtain a signal proportional to the emitted power we need to correct the acquired spectra to the sensitivity function as discussed in the introduction. In practice prior to the measurement we acquire spectra from well known radiative source (black body) such as Wolfram or Deuterium lamp. Comparing retrieved spectra to theoretical prediction we can estimate the sensitivity function of spectrometer $C(\lambda)$ (Fig. 1.12 in the middle). The correction of the acquired

spectra is then performed as

$$I^{\sim P^{emitted}} = \frac{I^{measured} - I^{Background}}{C} \tag{1.21}$$

here before treating the measured signal we subtract the background noise of detector. The comparison of corrected and uncorrected spectra is shown on figure 1.12. Obtained function spectra then provides a relative information about all observed emitters and can be used in various processes of physical analysis.

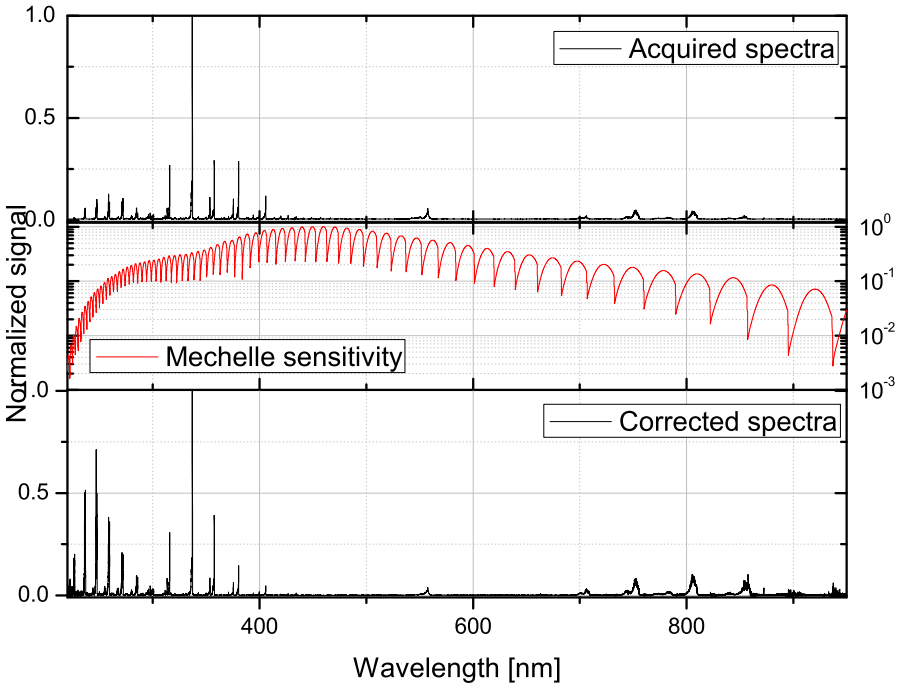

Figure 1.12: Example of sensitivity function for echelle spectrograph and its effect on the spectra.

1.3 Absorption spectroscopy with high finesse cavities

High sensitivity absorption spectroscopy techniques present a very complex tool for the trace gas detection (estimation of the concentration n), spectroscopic investigation (line strengths S measurements) or the environment metrology (e.g. temperature or pressure determination from line shapes).

Thanks to the past twenty years of exploration and theoretical calculations we can nowadays access these results through many spectroscopic databases. One of the most common is the HIRTAN (high–resolution transmission molecular absorption database) [76][3]. It contains over 2700000 lines for 41 different absorbents. Using this data one could estimate quite precisely the expected levels of absorption for different environments containing various absorbing molecules. Figure 1.13 shows example of atmospheric absorption coefficients in infra–red range for naturally most abundant molecules in atmosphere (using the model IAO, high latitude, summer[4]). In spectroscopy the concentration of molecules (of i–th element) is often expressed as the abundance ratio $a_i = N_i/N$, where N is the total number of molecules per volume or mole at given pressure. Furthermore a notation *parts per X – ppx* is introduced by multiplying the abundance by the X (e.g. ppm means parts per million – X=10^6). The most active molecule in ambient air is the water (absorption up to $10^{-3}\,\mathrm{cm}^{-1}$) due to its structure (large dipole moment) and relatively high concentration (e.g. 5900 ppm in case of the IAO, summer, high latitude model). Other molecules absorb by the orders of magnitudes less than water with local maxima in this range at $5000\,\mathrm{cm}^{-1}$ – CO_2 ($10^{-5}\,\mathrm{cm}^{-1}$), at $4300\,\mathrm{cm}^{-1}$ – CH_4 ($10^{-7}\,\mathrm{cm}^{-1}$), *etc.*.

Another aspect of air spectra is the density of spectral lines. In figure 1.14 we plotted a small portion of the air spectra with enhanced concentrations of molecules to demonstrate the complexity of the spectral pattern. The line shapes of each transition are determined by both the molecule and by the en-

[3]http://www.cfa.harvard.edu/hitran/
[4]http://spectra.iao.ru

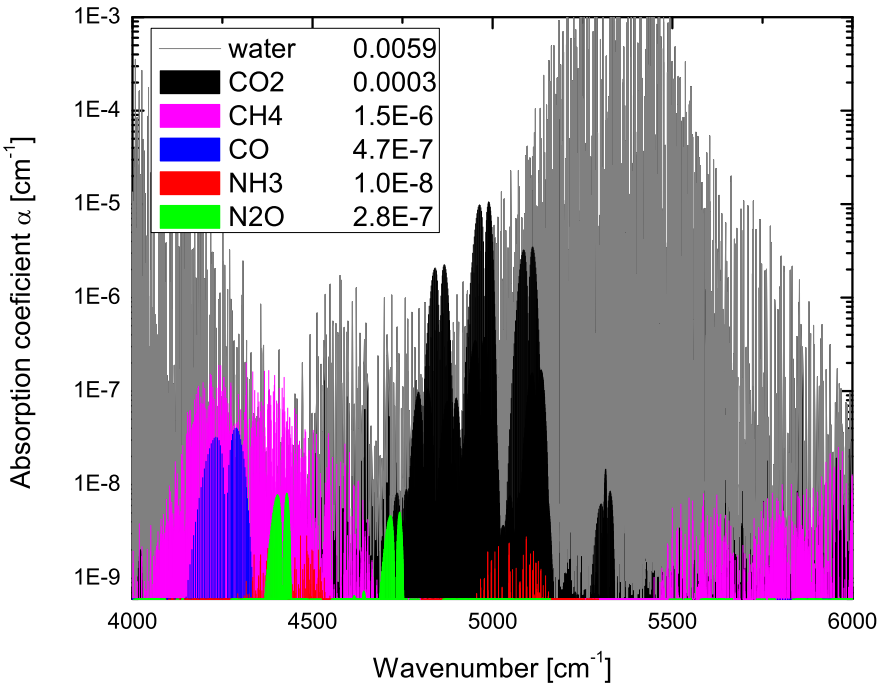

Figure 1.13: Atmospheric absorption of H_2O, CO_2, CH_4, CO, NH_3 and N_2O in the infra–red region.

Name	profile▼	FWHM	★ at 1 atm	★ at 0.1 atm
Natural w.	L	A_{ba}/π	4E-8	4E-8
Doppler w.	G	$2\nu/c \cdot \sqrt{\ln 2} \cdot \sqrt{2R\frac{T}{M}}$	0.0119	0.0119
Collision w.	L	$\gamma_{self} \cdot p_i + \gamma_{air} \cdot (p - p_i)$	0.0930	0.0093

▼ L=Lorentz, G=Gauss
★ is a H_2O at 4306.71772 cm^{-1} and 5000 ppm of H_2O

Table 1.3: Most common line shapes profiles, T – temperature [K], M – molar mass [g.mol^{-1}], p – total pressure, p_i – partial pressure, γ_{air} and γ_{self} are the pressure broadening coefficients as used in the HITRAN database [75]

vironment. In most cases we recognize three main reasons for line broadening. It is the radiative life-time of molecule (Lorentz line profile), the velocity with respect to detector (Gauss line profile) and the collisions with other molecules (Lorentz line profile). In general case a suitable approximation for line shape is a voigt function which is a convolution of Gauss and Lorentz peak functions. More detailed description can be found for example in [17], here we limit to the basic formulations for different contributions to linewidth presented in table 1.3. In the last two columns there is example of calculated widths for a water line at 4306.72 cm^{-1} – the strongest line on the figure 1.14. We simulated the same spectra for different pressures to show the domination effect of pressure broadening at high pressures (lines are practically pure Lorentz functions). At lower pressures we see that the contribution from Doppler and collisional broadening approximately equals while the natural width is still much lower.

To conclude there are several key notes to remark after the reconnaissance of molecular absorption through the HITRAN database. For the air trace detection the two main problems are the strong water absorption and the low absorption by molecules of interest. To overcome this issues two main strategies are usually used (often combined). First it is the smart choice for the probing light frequency e.g. choosing the frequencies with small water activity – water windows (one example is at 4300 cm^{-1}). Second is to enhance the detection by introducing different scheme for probing beam interaction path. In further part of the section we show how the Fabry–Pérot resonant cavity fulfils these criteria and how is this effect exploited in the absorption

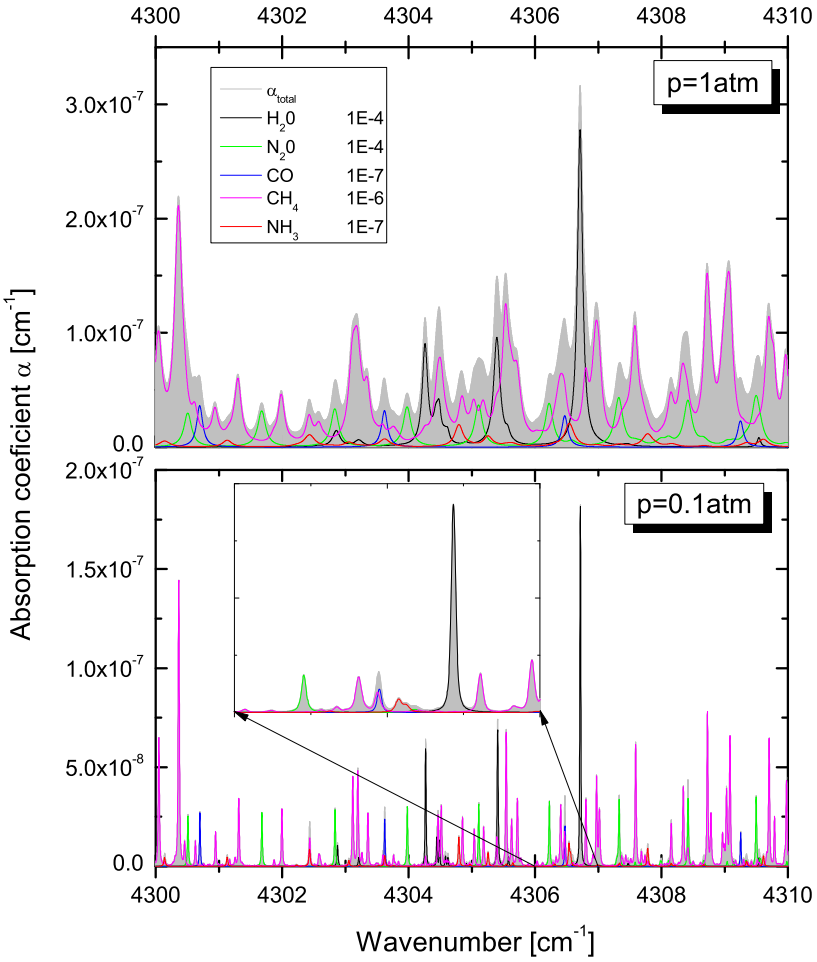

Figure 1.14: Model of absorption spectra around 4300 cm^{-1} for two pressures. The abundances are scaled to obtain similar absorption peaks for all plotted elements.

spectroscopy techniques.

1.3.1 The Fabry–Pérot resonator

The effect of the Fabry–Pérot resonator (FPR) on the capability of detection smaller absorptions with higher precision can be rigorously demonstrated. The uncertainty of the absorption coefficient α, $\delta\alpha$ can be deduced by differentiating the relation between measured transmitted signal I_{scheme} and the sample

absorption $\alpha = H^{-1}_{scheme}(I_{scheme})$

$$\delta\alpha_{scheme} = \left|\frac{\mathrm{d}H^{-1}(I)}{\mathrm{d}I}\right|_{I=I_{scheme}} \cdot \delta I \tag{1.22}$$

where H^{-1} is the inverse function to the transmittance $H(\alpha)$ defined as

$$I_{scheme} = I_0 \cdot H_{scheme}(\alpha) \tag{1.23}$$

The situation is showed on figure 1.15. In comparison we consider two scenarios of passage through the sample, the direct pass and through the FPR. In both cases the incident intensity I_0, the detection uncertainty δI and the sample length L_0 are the same. For the absorption retrieved from the direct path signal we can use the Beer–Lamber law (Eq. 1.6) to obtain

$$\alpha = H^{-1}_{direct} = -\frac{1}{L_0}\ln\frac{I_{direct}}{I_0} \tag{1.24}$$

After differentiation we get the estimation of the absorption uncertainty $\delta\alpha_{direct}$

$$\delta\alpha_{direct} = \frac{1}{L_0}\frac{\delta I}{I_{direct}} \tag{1.25}$$

In case of Fabry–Pérot resonator, with mirrors of reflectivity R, transmission T and losses L ($L+T+R=1$) the transmitted intensity $I_{F.P.}$ is a sum of interfering beams leaking from the cavity after different number of reflection. Each of this beam travelled different path and was generated at different time leading to a phase difference with respect to other beams. This strongly affects the form of the $H_{F.P.}$ function regarding different sources of light. In case of adiabatic approximation of interaction between monochromatic wave and stable resonator the response time of cavity is much shorter than the frequency variation of the source. The transmitted intensity depends on frequency as [45]

$$I_{F.P.} = I_0 \cdot T^2 \frac{\exp\left(-\alpha L_0\right)}{\left[1 - R\exp\left(-\alpha L_0\right)\right]^2 + 4R\exp\left(-\alpha L_0\right)\cdot\sin^2\left(kL\right)} \tag{1.26}$$

where $k = \omega/c$ is the wave factor responsible for frequency filter behaviour of

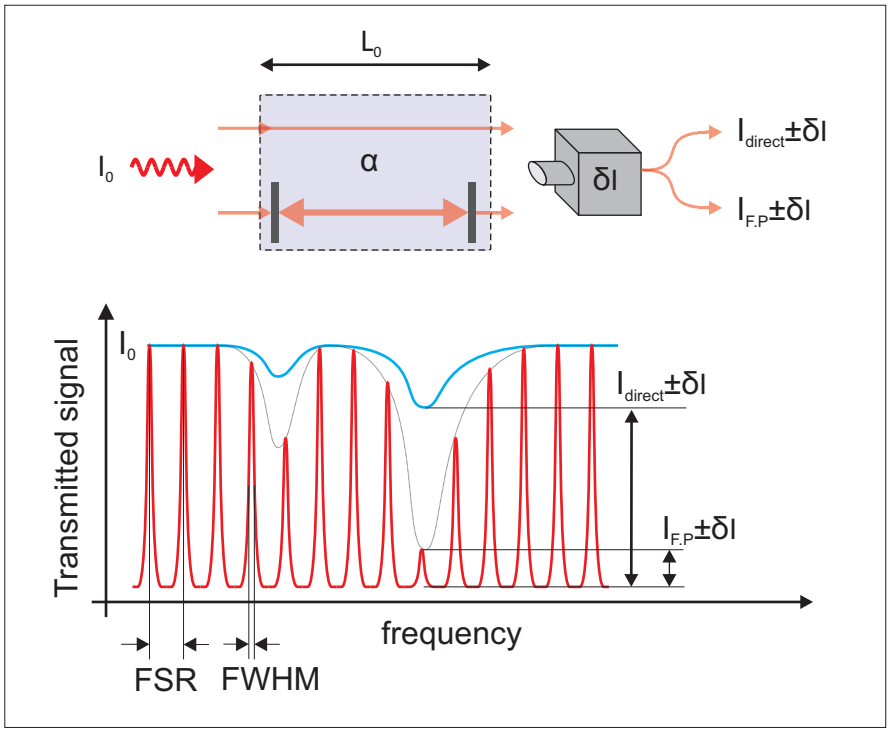

Figure 1.15: Scheme of comparison between direct path and FPR absorption.

the cavity. Every $c/2L$ frequency the beams leak out with the same phase producing positive interference maximum ($\sin(kL) = 0$). This value is called the free spectral range (FSR) of cavity. The half width at full maxima (FWHM) of cavity resonance $\delta\nu_{cav.}$ depends on the finesse $F = \pi\sqrt{R}/(1-R^2)$ or quality $Q = F/\pi$ of the resonator as $\delta\nu_{cav} = FSR/F$. In time domain the corresponding variable to line width is the cavity response time τ_{cav}

$$\tau_{cav} = \frac{1}{2\pi\delta\nu_{cav}} \tag{1.27}$$

The transmitted intensity maximum in resonance is then

$$I_{F.P.}^{Max.} = I_0 \frac{T^2}{R} \frac{R_{eff.}}{[1-R_{eff.}]^2} \tag{1.28}$$

where $R_{eff.} = R\exp(-\alpha L)$ is the effective reflectivity. Resolving this quadratic

equation for α we find

$$\alpha_{F.P.} = -\frac{1}{L_0} \ln \left\{ \frac{1}{R} \frac{1 + 2(\frac{I_{F.P.}}{I_0}\frac{R}{T^2}) - \sqrt{1 + 4(\frac{I_{F.P.}}{I_0}\frac{R}{T^2})}}{2(\frac{I_{F.P.}}{I_0}\frac{R}{T^2})} \right\} \tag{1.29}$$

Consecutively by derivation of this expression with respect to $I_F.P.$ and using equation 1.25 for $\delta\alpha_{direct}$ we get the $\delta\alpha_{direct}/\delta\alpha_{F.P.}$ dependence as a function of parameters (α, R) of the system. The exact behaviour of this function is plotted on the figure 1.16 for ideal mirrors ($R+T=1$) and L_0=1 m. In case of weak absorptions $L_0 \cdot \alpha << 1$ we can use the approximative relation for $I_{F.P.}$ thus simplifying the equation 1.29 into

$$\alpha^{approx.} = \left[1 - \frac{I_{F.P.}}{I_0} \cdot \frac{(1-R)^2}{T^2}\right] \frac{1-R}{1+R} \frac{1}{L_0} \tag{1.30}$$

in this approximation the $\delta\alpha_{direct}$ has form $1/L_0 \cdot \delta I/I_0$ which leads to

$$\delta\alpha_{F.P.}^{approx.} = \frac{1}{L_0}\frac{\delta I}{I_0}\frac{1-R}{1+R} = \frac{1-R}{1+R}\delta\alpha_{direct}^{approx.} \tag{1.31}$$

This corresponds to the linear behaviour of $\delta\alpha_{direct}/\delta\alpha_{F.P.}$ function. For a given value of α we can find an optimal value of cavity quality (mirror reflectivity). Further increase of R will result lover precision due to the faster decrease of transmitted intensity. On the other hand at high quality resonators have lower detection limits (smaller $\alpha_{min.}$) and still offers higher precision in broad scale of absorptions than single pas methods. The ratio in precision can be reduced by use of multi-pass trajectories by factor n representing the number of passes through the sample. There exist many types of cavities allowing optimal multi-pass in sample most common are the White [92, 93] or Herriot [33, 71] cells (see figure 1.17). In general they allow up to hundreds (more common is tens) of passes [3, 18] offering a better performance than single pass or resonant cavity in case of moderate absorptions and no frequency filtering like the FPR.

To conclude from the theoretical calculations it is clear that the high finesse resonant optical cavity (HFC) like FPR are a very suitable tool mainly when

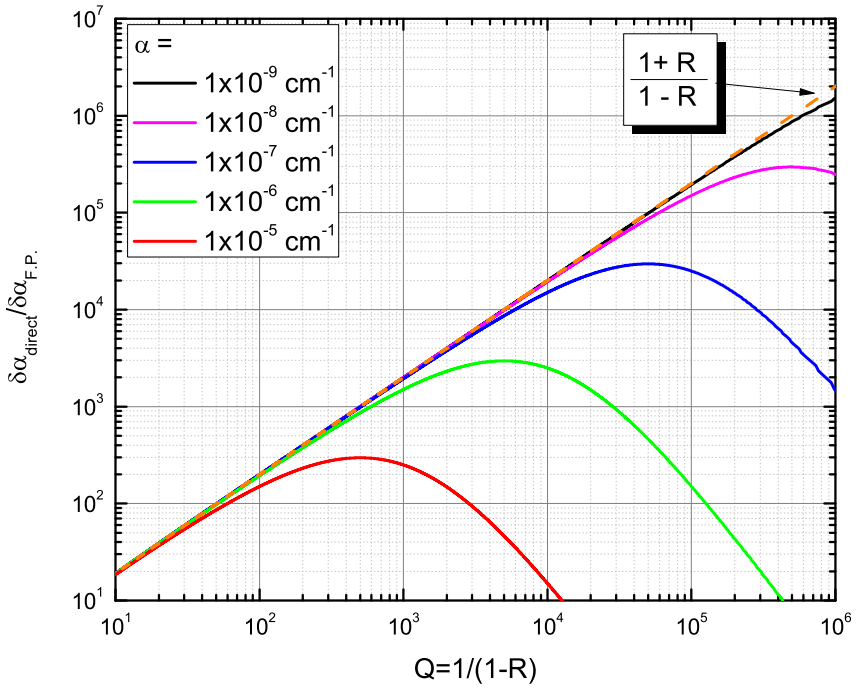

Figure 1.16: Ratio of absorption coefficient uncertainties when measured by direct path or FPR.

targeting weak absorptions. Also concentrating the interaction along a single line reduces the demands on the studied sample volume. The price we pay for the increase of interaction path is that the effect works only for frequencies resonant with the cavity. This limits the spectral resolution to one FSR of the FPR. For example in case of 1 m long cavity with air the FSR is 150 MHz or $0.005\,\mathrm{cm}^{-1}$. If we compare this value with the line widths from table 1.3 we find that for low pressures this is unsatisfactory value. Another problem arises when considering a real application. The presented model was based on the fact that all incoming light was coupled to the cavity resonance mode without loses. For a real source with given frequency width, noise and stability the mode coupling efficiency to the HFC mode is often far less than one. And last, we showed how the FPRs specially HFCs could enhance the detection but for the moment we did not show how the absolute measurements are done without further calibration (to determine the non-absorption loses and cavity length).

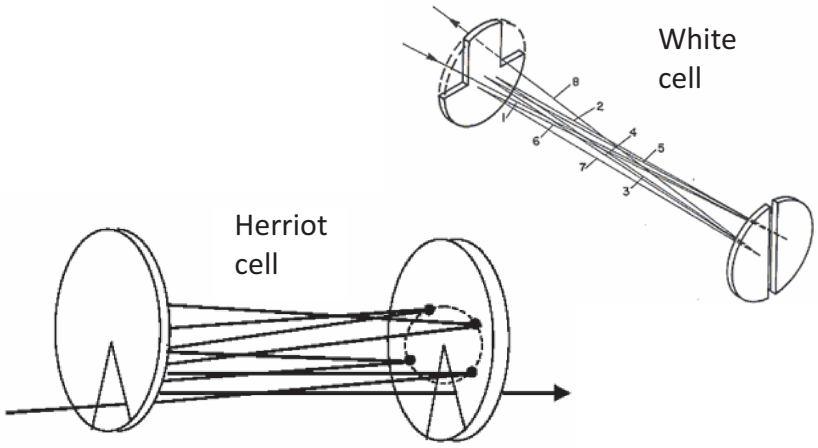

Figure 1.17: Two types of multi–pass cell arrangement, the White [93] and Herriot [33] cell.

To quantify this drawbacks or discuss the possibility of auto–calibration for HFCs we need to use more precise description for the light-HFC interaction. Namely we need to take into account the 3D space propagation because that is the real space where we operate. Next we address coupling of ideal tunable (monochromatic and coherent) source (like laser) to single HFC mode. We follow by describing the effect of source phase noise and intra–cavity absorption to obtain a real transmission function $H_{F.P.}$ for HFC. Finally in last part the effect of optical feed–back from HFC to a laser on the injection efficiency is discussed.

3D – HFC

Supposing a electromagnetic wave propagating in the direction of axis z we could write the Maxwell wave equation in par-axial approximation as

$$\frac{\partial^2 E}{\partial x^2} + \frac{\partial^2 E}{\partial y^2} - 2ki\frac{\partial E}{\partial z} = 0 \tag{1.32}$$

where $E(x, y, z)$ is the field and k is the wave factor. The solutions in Cartesian system have form of

$$\begin{aligned} E_{m,n} &= A_{m,n} \cdot \exp\left(-i\Psi_{m,n}\right) \\ A_{m,n} &= E_0 \cdot \frac{w_0}{w(z)} \cdot H_m(\sqrt{2}\frac{x}{w(z)}) \cdot H_n(\sqrt{2}\frac{y}{w(z)}) \cdot \exp\left(-\frac{x^2+y^2}{w^2(z)}\right) \\ \Psi_{m,n} &= k\frac{x^2+y^2}{2r_c(z)} + kz - (m+n+1)\arctan\frac{z}{z_0} \end{aligned} \tag{1.33}$$

The equation 1.33 describes the distribution of electromagnetic field as a product of two Hermite polynomials H_m and H_n, Gaussian function and phase term $\Psi_{m,n}$. The shape in the x–y plane is govern by the polynomial order order m and n. The beam propagation along the z axis is defined by the beam width $w(z)$ (radius where the field amplitude drops to $1/\,\mathrm{e}^2$ of maximum) and wave–front radius of curvature r_c

$$w(z) = w_0\sqrt{1+\left(\frac{\lambda z}{\pi w_0^2}\right)^2} = w_0\sqrt{1+\left(\frac{z}{z_0}\right)^2} \tag{1.34}$$

$$r_c(z) = z\left[1+\left(\frac{\pi w_0^2}{\lambda z}\right)^2\right] = z\left[1+\left(\frac{z_0}{z}\right)^2\right] \tag{1.35}$$

with the beam waist $w_0 = w(z=0)$ and the Rayleigh range z_0 indicating the collimation length of the beam (distance between origin and point where the beam width is $\sqrt{2}w_0$)

$$z_0 = \pi\frac{w_0^2}{\lambda} \tag{1.36}$$

The divergence of the beam θ – asymptote to $w(z)$ can by expressed as

$$\theta = \tan\left(\lim_{z\to\infty}\frac{w(z)}{z}\right) = \tan\frac{w_0}{z_0} \simeq \frac{\lambda}{\pi w_0} \tag{1.37}$$

For electromagnetic wave to have a steady state solution inside the resonator three conditions have to be fulfilled. First, the reflected beams must interact with the same phase $\Psi_{m,n}(z_1) - \Psi_{m,n}(z_1) = q \cdot \pi$, $q \in \mathbb{N}_0$ to produce a positive interference. Second, the wave–front curvature r_c has to match that of the cavity mirrors surfaces R_{c1}, R_{c2}. And last is that on both mirrors the beam spot ($\pi w(z_i)^2$) has finite size. From the phase condition we can deduce

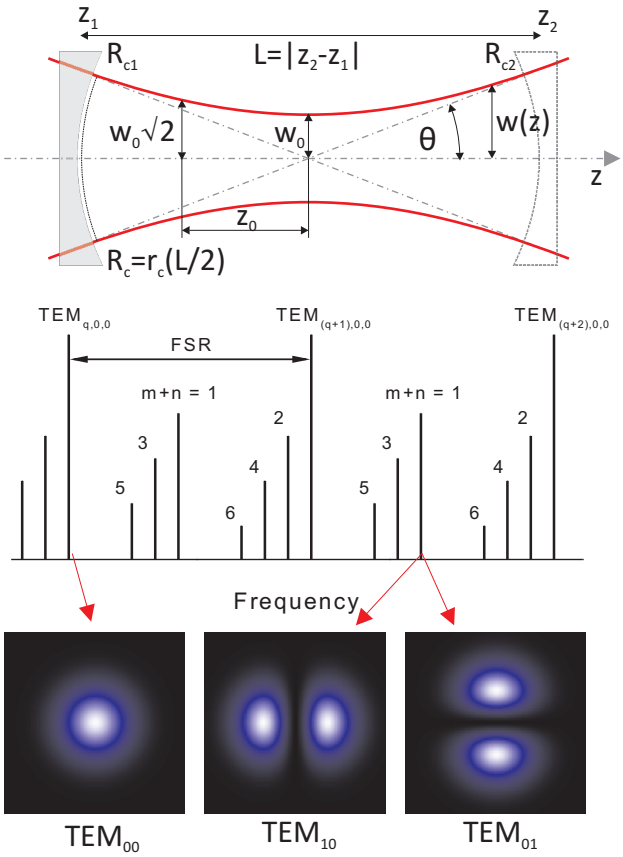

Figure 1.18: Frequency and spatial characteristics for some TEM_{qnm} FPR modes in 3D space.

the frequency eigenvalues of FPR

$$\nu_{q,m,n} = \frac{c}{2L}\left\{q + \frac{1}{\pi}(m+n+1)\left(\arctan\sqrt{\frac{z_2}{R_{c2}-z_2}} - \arctan\sqrt{\frac{z_1}{R_{c1}-z_1}}\right)\right\} \tag{1.38}$$

The situation is depicted on figure 1.18. For each q we have a family of modes (denoted as TEM_{mn}) with different x–y plane field distribution within the order (same q) but same compared to other modes for equal $m+n$. The principal mode TEM_{00} has the form of Gaussian peak and most of the field is concentrated along the principal axe of cavity, therefore has the lowest diffraction losses among all TEM_{mn} modes. The spectral distance between modes for a

symmetric cavity $R_{c1} = R_{c2} = R_c$ is

$$\nu_{q,m,n} - \nu_{q,m',n'} = \frac{c}{\pi L}\sqrt{\frac{L}{2R_c - L}}\Delta(m+n) \tag{1.39}$$

$$\nu_{q,m,n} - \nu_{q',m,n} = FSR = \frac{c}{2L} \tag{1.40}$$

From the wave–front curvature condition we can calculate the beam waist inside the cavity. Again in case of symmetric cavity we have

$$w_0 = \sqrt{\frac{\lambda}{2\pi}} \cdot [L(2R_c - L)]^{\frac{1}{4}} \tag{1.41}$$

Finally the last condition for a finite beam size limits the values of cavity length and mirror curvature in case of stable resonator to

$$0 \leq \left(1 - \frac{L}{R_{c1}}\right)\left(1 - \frac{L}{R_{c2}}\right) \leq 1 \tag{1.42}$$

We see that the situation in 3D space is much complex than in simple 1D example of FPR. We have more resonances which can be good for the frequency resolution but actually brings problems with calibration because each of different TEM_{mn} mode has different diffraction loses. This produces different sensitivity in the absorption measurements therefore in many methods we try to excite only the principal TEM_{00} whose losses are according the diffraction theory closest to the 1D case. The parameter describing the amount of energy successfully injected into this mode is called the injection efficiency H^{eff}. We use definition set by Morville et al. [56]. He proposed to normalize the measured transmission maximum $H^{max}_{exp.}$ to the maximum calculated according to the theoretical 1D model accounting for optical losses in mirrors and in case of zero absorption in cavity for corresponding optical scheme $H^{max}_{theory,\alpha=0}$

$$H^{eff} = \frac{H^{max}_{exp.}}{H^{max}_{theory,\alpha=0}} \tag{1.43}$$

Ideal model for FPR injection

Closest to the adiabatic tuning is the case of monochromatic source linear frequency sweep. The theory describing this interaction has been subject of

many studies for example for its application in the high resolution spectroscopy [45, 56], HFC finesse measurement [54, 68] or laser linewidth determination [40]. Here we show only the results and some examples for demonstration of the HFC transmission. We resumed the complete deduction in the appendix.

The temporal behaviour of radiation source frequency $\omega(t)$ and cavity length $L(t)$ is studied around a FPR resonance

$$L(t) = L_0 + v \cdot t \tag{1.44}$$

$$\omega(t) = \omega_0 + W \cdot t \tag{1.45}$$

where v and W are the cavity tuning speed in m.s^{-1} and angular frequency scanning speed in rad.Hz.s^{-1} respectively. The initial ($t = 0$) frequency ω_0 and cavity length L_0 obey the condition for FPR resonance from 1.38

$$\omega_0 = 2\pi \cdot \frac{c}{2L_0} \tag{1.46}$$

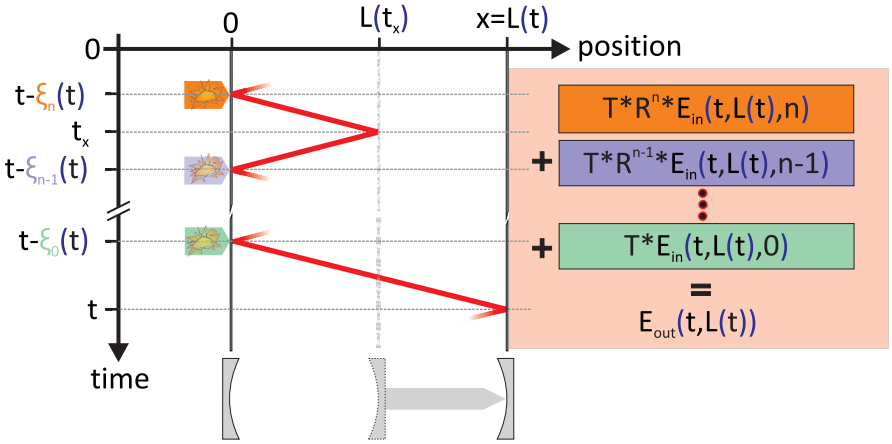

Figure 1.19: FPR output as a superposition of fields oscillating inside the resonator.

The output electromagnetic field $E_{out}(t)$ at the output mirror ($x = L(t)$) could be evaluated as a sum of all waves leaving the cavity in the time t after different number of round trips

$$E_{out}(t, L(t)) = T \cdot \sum_{n=0}^{\infty} R^n \cdot E_{in}(t, L(t), n) \tag{1.47}$$

The electromagnetic field from the source measured at position x at time t after n full round trips in cavity is

$$E_{in}(t,x,n) = \sqrt{T}\cdot R^n \cdot A \cdot \exp\left\{ i\left[\omega_0 + \frac{W}{2}\left(t - \xi_n(x,t)\right)\right]\left(t - \xi_n(x,t)\right)\right\} \quad (1.48)$$

where $\xi_n(t)$ is the residence time of wave arrived at coordinate x the time t after n round trips

$$\xi_n(t) = \xi_0 + \frac{2}{c}\left\{\left[L_0 + v\left(t - \xi_0 + \frac{L_0}{c}\right)\right]n - \frac{v}{c}L_0 n^2\right\} \quad (1.49)$$

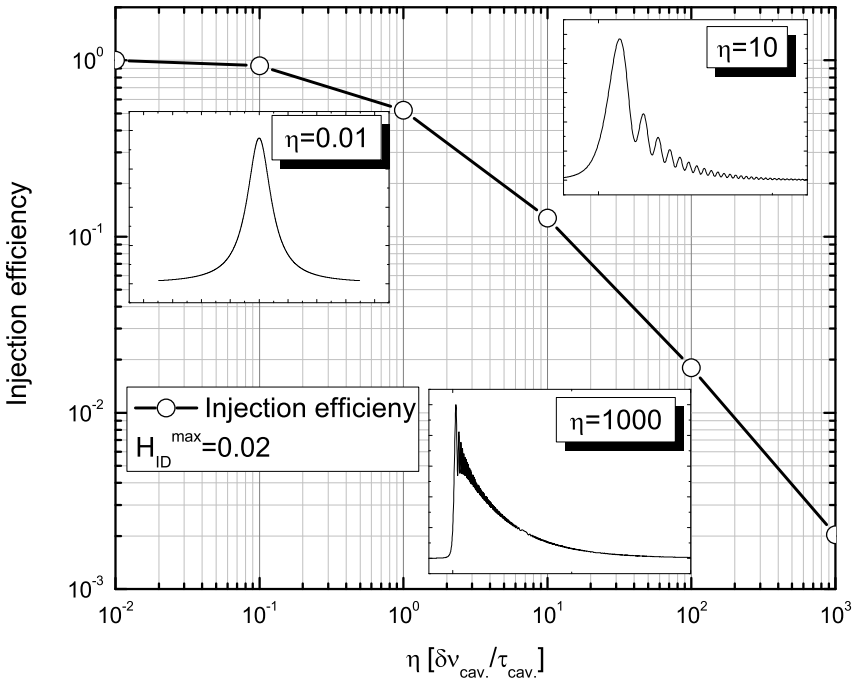

Figure 1.20: Ideal injection efficiency of monochromatic source into FPR when swept through the FPR resonance with different speed.

In simulations we considered cavity with $T = 1.6 \times 10^{-5}$ and $L = 1 \times 10^{-4}$. The theoretical maximum of $H^{max}_{theory,\alpha=0}$ was 0.02 (for $I_0 = 1$). As the pattern of the transmission depends on the FPR quality it is convenient [56] to use the reduced unit for the tuning speed η in cavity mode width per unit of cavity

response time units

$$\eta = \frac{W}{2\pi} \cdot \frac{\tau_{cav}}{\delta\nu} \tag{1.50}$$

Figure 1.20 shows simulated transmissions for various tuning speeds together with corresponding injection efficiencies. We see that for $\eta \ll 1$ the signal converge to the adiabatic case of Lorentzian peak transmission function. This is because the cavity field has enough time to response to the incidence field variations. For higher tuning rates the lack of interaction time manifests in so called ringing effects caused by beating between ongoing cavity field build–up and the incoming field. Finally at the high tuning rates $\eta \gg 1$ the ringing oscillations become very fast with small amplitudes. The transmittance function has then almost exponential form and minimal amplitude.

Realistic model for FPR injection

In this part we present a description of the cavity-light interaction with parameters describing the real situation we encounter in practice. We show in a simple approximation how the amplitude modulations and the phase variations of the interacting field and the intra–cavity absorption affect the transmittance function of the cavity. This will modify the input field from 3.7 into

$$\begin{aligned} E_{in}^{real}(t,x,n) \quad = \quad & \sqrt{T} \cdot R^n \cdot A(t - \xi_n(x,t)) \cdot \\ & \cdot \exp\left\{-\frac{\alpha}{2}\xi_n(x,t)c\right\} \cdot \\ & \cdot \exp\left\{i\left[\omega_0 + \frac{W}{2}\left(t - \xi_n(x,t)\right)\right]\left(t - \xi_n(x,t)\right)\right\} \cdot \\ & \cdot \exp\left\{i\Phi(t - \xi_n(x,t))\right\} \end{aligned} \tag{1.51}$$

where the amplitude A and phase shift Φ are now time dependant variables and α is the intra–cavity absorption coefficient. To be able to more efficiently calculate the output field sum according to 3.13 it is convenient to use the recurrent expression of this relation. We can find it by comparing the output

fields after one cavity round–trip time Δ (Fig. 1.21)

$$\begin{aligned} E_{out}^{real}(t+\Delta, L(t+\Delta)) &= T \cdot \sum_{n=0}^{\infty} R^n \cdot E_{in}^{real}(t+\Delta, L(t+\Delta), n) \\ &= T \cdot R^0 \cdot E_{in}^{real}(t+\Delta, L(t+\Delta), 0) + \\ &= +T \cdot \sum_{n=1}^{\infty} R^n \cdot E_{in}^{real}(t+\Delta, L(t+\Delta), n) \end{aligned}$$

realizing that $\xi_{n+1}(t+\Delta) = \xi_n(t) + \Delta$ from the definition of the residence time we can transform the equation 1.52 to

$$\begin{aligned} E_{out}^{real}(t+\Delta, L(t+\Delta)) &= T \cdot E_{in}^{real}(t+\Delta, L(t+\Delta), 0) + \\ &= R \cdot \exp\left\{-\frac{\alpha}{2}\Delta c\right\} \cdot E_{out}^{real}(t, L(t)) \end{aligned} \quad (1.52)$$

The graphical representation of the recurrent relation 1.52 is on figure 1.21. After each round–trip the output field is a result of interference between arriving field transmitted through cavity and stored field inside the cavity.

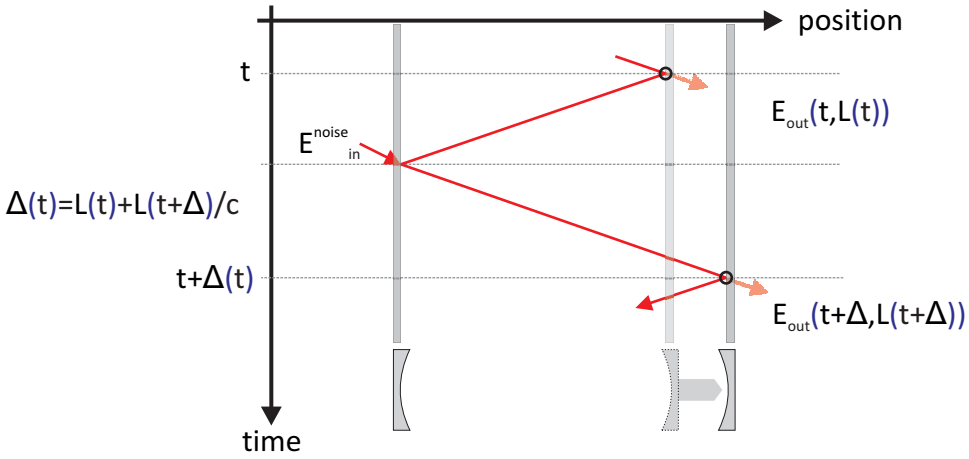

Figure 1.21: Recurrent expression for the cavity output field allowing relatively easy and efficient accounting for the noise and the absorption.

To properly introduce the phase variations of the source we follow the reasoning presented in [56]. Morville et al. studied the HFC injection efficiencies for the lasers with finite linewidth. To describe the laser random phase walk they used the Schawlow and Townes (S.T.) theory [78]. The theory shows that the laser linewidth is fundamentally limited by the laser field phase diffusion

resulting from the spontaneous emission in the laser medium. Each spontaneously emitted photon has a random phase ϕ (from 0 to 2π rad) with respect to the laser field. This causes the phase shift of the field depending on the field amplitude $\sqrt{N}$

$$\mathrm{d}\Phi = \frac{\sin\phi}{\sqrt{N}} \tag{1.53}$$

where N is number of photons confined in laser resonator. The number of the spontaneous emission events is described by the rate $R_{s.p.}$. Its value depends on the internal structure of the laser active medium. The total change of phase could be found by summing the individual phase variations over the observation time period Δ.

$$\Phi(t+\Delta) = \Phi(t) + \frac{1}{\sqrt{N}} \sum_{i=0}^{\Delta \cdot R_{s.p.}} \sin\phi_i \tag{1.54}$$

By the central-theorem limit for the sum of statistically independent events, should possess a normal distribution described by the coherence time τ_c. It is an average time needed for the phase change of 1 rad. The power spectral density of the laser field has than Lorentzian profile characterized by the S.T. linewidth [67]

$$\Delta\nu_{S.T.} = \frac{1}{\pi\tau_c} = \frac{R_{s.p.}}{2\pi N} \tag{1.55}$$

Some examples of the linewidth effect on the FPR transmission is on the figure 1.22. The signals are simulated according to the equation 1.52 for zero α. The linewidth is expressed in the relative unit κ, normalized to the FPR $\delta\nu_{cav}$. For the linewidth smaller than the $\delta\nu_{cav}$ ($\kappa < 1$) the transmission function approaches the monochromatic case. This convergence is faster for higher tuning speed. The $\eta = 1$, $\kappa = 100$ case is close to what we can expect from the standard semiconductor laser (linewidth in orders of MHz) coupled to HFC ($\delta\nu_{cav}$ in orders of 10 kHz) [56]. Better signals, like the $\eta = 1$, $\kappa = 100$ case, can be obtained with more coherent sources for example external cavity diode lasers (linewidth in orders of kHz) rapidly tuned across the FPR resonance [16].

Figure 1.23 is taken from [56] and represents overview of simulated and ex-

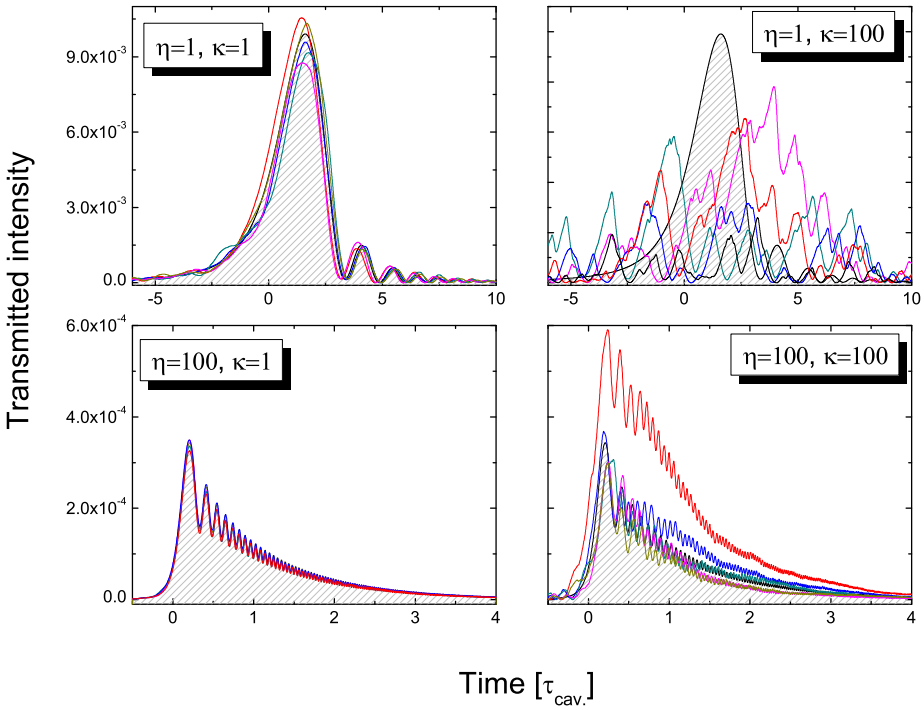

Figure 1.22: FPR transmission as a function of frequency tuning speed and laser linewidth.

perimental data of the realistic FPR injection efficiency. The theory shows to be with a good agreement with the measured points and confirms the convergence of transmission function to the monochromatic case at high tuning rates. In this case the phase change is not fast enough to sufficiently perturb the cavity laser interaction therefore the observed pattern is similar to one in the monochromatic case.

Second aspect we want to point out regarding the FPR injection is the amplitude variations of the incoming field. Particularly we show how is possible to measure the response time of the cavity even with sources producing noisy transmittance signals. The idea comes out directly from the recurrent equation 1.52. We see that if at given time the input field is suddenly turned off the output field will depend only on the decay of the field confined inside the cavity at this moment. Therefore the output will not be furthermore affected by the source phase oscillations. The followed smooth light decay is also called

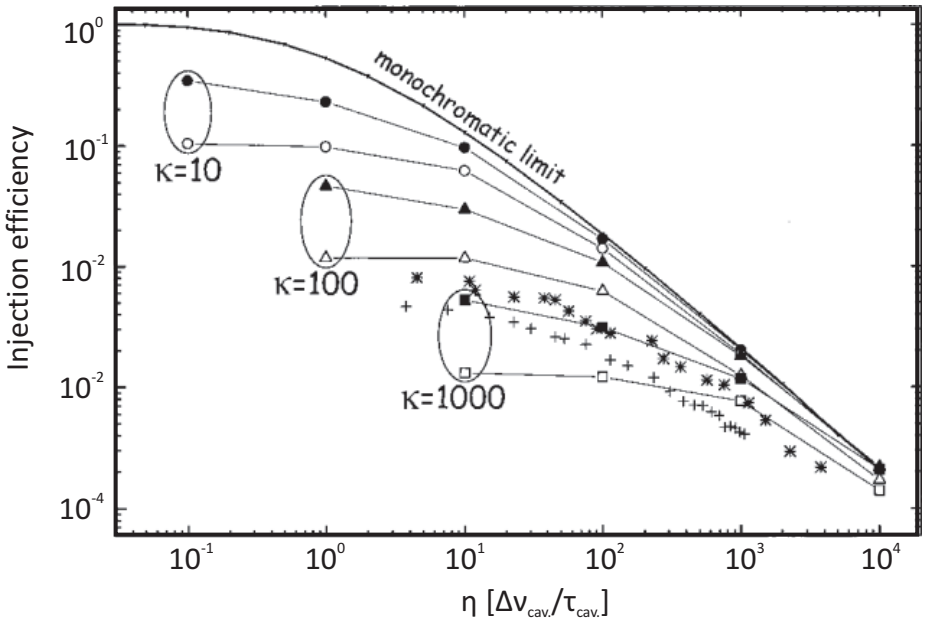

Figure 1.23: FPR injection efficiency as a function of tuning speed and laser linewidth taken from [56].

ring–down and its form can be easily deduced in steady cavity approximation ($\Delta(t) = 2L_0/c$)

$$\begin{aligned} E(t - t_{trigg}) &= E(t_{trigg}) \cdot \left(R \cdot \exp\left[-\frac{1}{2}\alpha\Delta c\right] \right)^{(t-t_{trigg})/\Delta} \\ &= E(t_{trigg}) \cdot \exp\left[(\ln R - \frac{1}{2}\alpha\Delta c)(t - t_{trigg})/\Delta \right] \\ &= E(t_{trigg}) \cdot \exp\left[-(t - t_{trigg}) \cdot \frac{c}{2L_0}(-\ln R + \alpha L_0) \right] \end{aligned}$$

For the decaying intensity (square of the field) we have than

$$I_{decay}(t) = I_0 \cdot \exp\left[-t\frac{c}{L_0}(\alpha L_0 - \ln R) \right] \tag{1.56}$$

with the decay (ring–down) time

$$\tau_{rd} = \frac{L_0}{c(\alpha L_0 - \ln R)} \tag{1.57}$$

In figure 1.24 we simulated some transmission signals for the $\nu = 1$ case for different levels of absorption and linewidth. We can see that in monochromatic case both the ring–down time and the maximal amplitude H^{max} are good

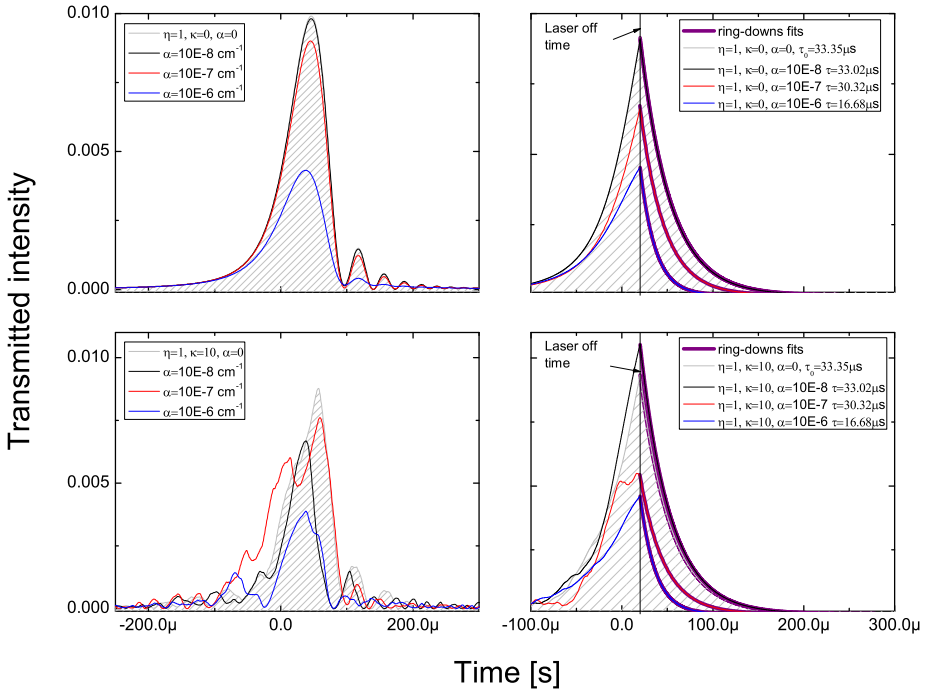

Figure 1.24: The effect of intra–cavity absorption on the transmission signal and ring–down time.

indicators for the intra–cavity absorption. For real sources is the situation different. Even for $\kappa = 10$ the maximum varies significantly and cannot be used to measure absorption coefficient from a single scan. The ring-down signals on the other hand show the same signal quality interdependency on the source therefore offer suitable tool for α determination.

To summarize the results we can conclude that the efficient injection of a standard monochromatic sources like lasers into HFCs is a real problem. For current sources (linewidth higher than kHz) the smooth transmittance signal is obtained only at high tuning rates resulting in high signal loses. Situation is better in case of ring–down measurements where the source noise affect only initial decay amplitude and not its form.

Fabry–Pérot resonator with coherent sources using OF

In previous models of light injection into a FPR mode we always considered that the source is not affected by the back–coming signal from the FPR. Usually this feedback causes a destructive perturbation into light generation. On the other hand Laurent et al. [43] pointed out that the optical feedback (OF) could have also positive effect on the emission properties of lasers. They showed that the OF from FPR could positively interfere with the laser field build up and significantly reduce the effect of random phase walk induced by spontaneous emission. To this happen they proposed a simple scheme of coupled laser FPR system (Fig. 1.25).

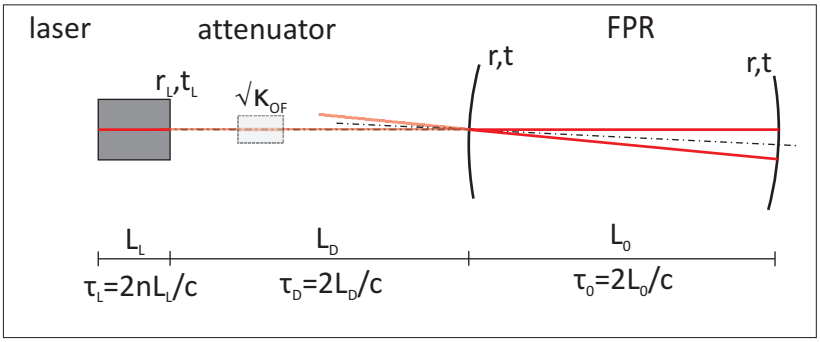

Figure 1.25: Scheme of optical layout for injecting the FPR with the help of OF according to [43].

To prevent feedback from the input mirror of the FPR the initially linear cavity is folded to form a V-shape resonator with equal arms of length L_0. The amount of OF returning to laser is controlled by the attenuator κ_{OF}=$\mathrm{I}_{OF}/\mathrm{I}_{laser}$. Laurent et al. solved the differential equation describing this system in two limit cases. The steady–state solution describes implicitly the frequency ω of the coupled system

$$\omega_{free} = \omega + K \cdot \frac{\sin\left[\omega(\tau_L + \tau_0) + \theta\right] - r^4 \sin\left[\omega(\tau_L - \tau_0) + \theta\right]}{1 + (2F_0/\pi)^2 \sin^2\left[\omega\tau_0\right]} \tag{1.58}$$

$\omega_{free} = q\pi c/nL_L$ is the laser cavity qth mode frequency and nL_L is the laser cavity optical length. τ_L and τ_0 are the round–trip times for laser cavity and

FPR respectively. The coupling constant K has in case of HFC ($r \simeq 1$) form

$$K = \sqrt{\kappa_{OF}(1+\alpha_H)^2}\frac{c}{2nL_L}\frac{F_0}{2F_L} \tag{1.59}$$

where α_H is the Henry phase–amplitude coupling factor, F_0 and F_L are the FPR and laser cavity finesses. In general case the system is multi–stable (for given frequency ω_{free} exists more than one ω satisfying the equation 1.58). We find stable periodic solution only rational values of $L_D/L_0 \simeq 1$. The figure 1.26 shows this behaviour for case $L_D/L_0 \simeq 1$. In case when the bi–stability occurs (for the red line) the laser frequency (thick grey line) will preferentially lock on a solution with smallest loss factor [43].

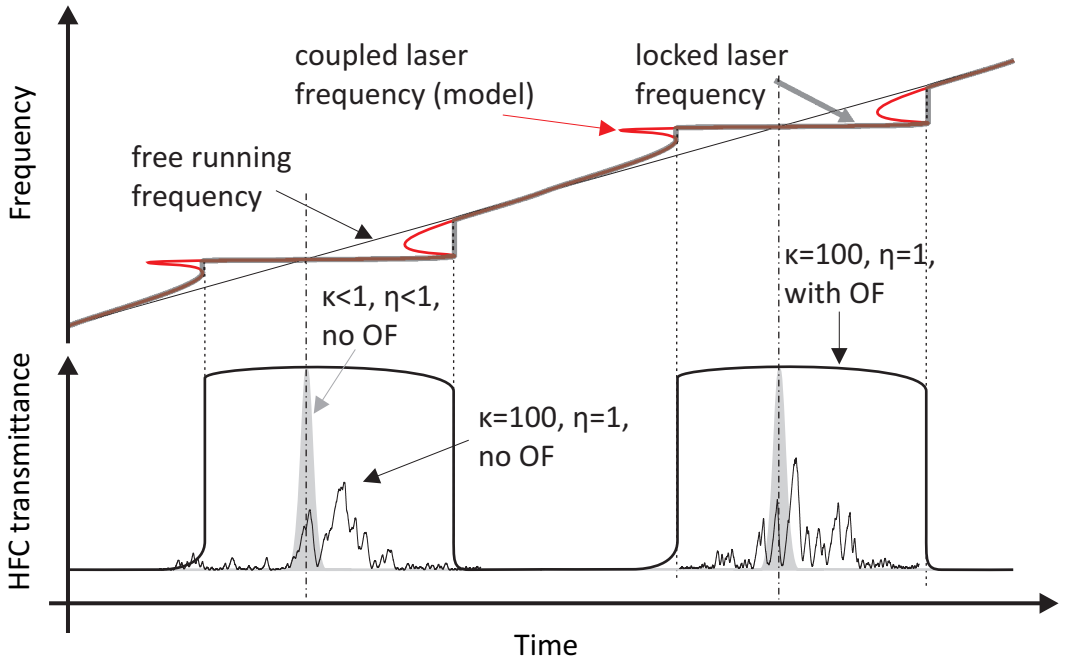

Figure 1.26: Laser frequency behaviour and its effect on the cavity transmission in the presence of OF.

Laurent at. al [43] also studied the dynamic response of the system to the amplitude and frequency fluctuations of the laser field. They found out that when the spontaneous emission is the only source of frequency noise the laser linewidth is significantly reduced to

$$\Delta\nu_{OF} = \Delta\nu_{S.T.} \cdot \left(\frac{nL_L}{L_0}\frac{F_L}{F_L}\frac{1}{\sqrt{\kappa_{OF}}}\right)^2 \tag{1.60}$$

where $\nu_{S.T.}$ is the linewidth according to S.T. theory (e.g. according to equation 1.55).

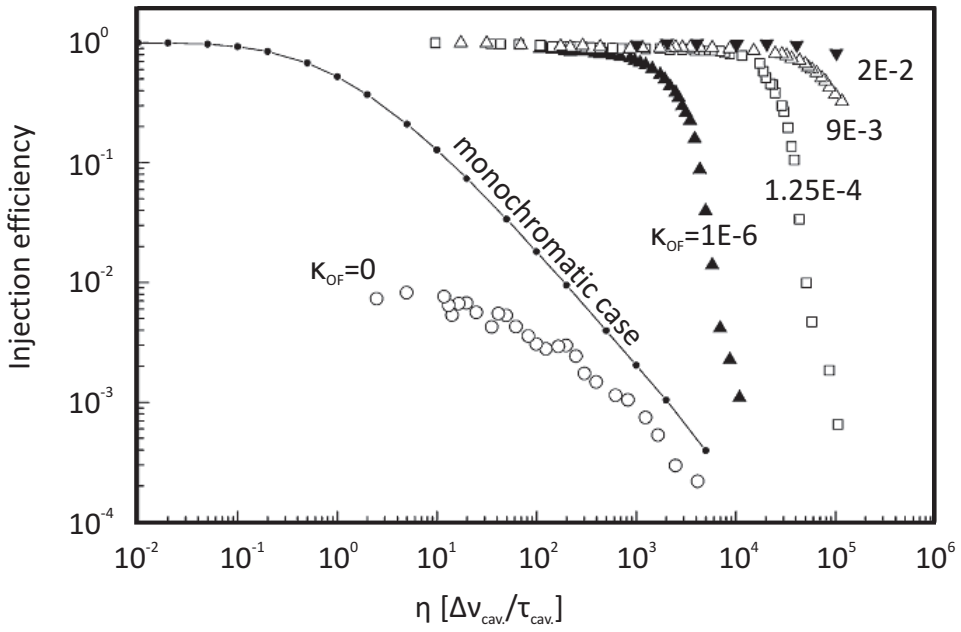

Figure 1.27: FPR injection efficiency in the presence of OF measured by Morville et al. [55].

Morville et al. [55] exploited this effect in the spectroscopic applications. They used a folded (V-shaped) cavity with maxima of the transmittance function given as

$$H_{V-cav.}^{max} = \left[\frac{T\, \mathrm{e}^{-\alpha^{max} L_1/2}}{1 - R^2\, \mathrm{e}^{-\alpha^{max}(L_1+L_2)}} \right]^2 \tag{1.61}$$

with L_1 and L_2 the cavity arms length, T and R the mirrors reflectivity and α^{max} the intra–cavity absorption at the mode maximum frequency. They also studied the injection efficiencies of the laser diode coupled to the HFC. Figure 1.27 shows measured data for different levels of OF. The results showed excellent increase of the injection efficiency compared to the case without OF (see figure 1.23). There are three main reasons behind this behaviour. First is the reduction of the locked laser linewidth below the mode width of HFC (Eq. 1.60). This assures that the transmission is close to the monochromatic case.

Second, the effective tuning rate η is "slowed" down around the resonance

$$\eta = C \cdot \frac{\mathrm{d}\omega}{\mathrm{d}t} = C \cdot \frac{\mathrm{d}\omega}{\mathrm{d}\omega_{free}} \frac{\mathrm{d}\omega_{free}}{\mathrm{d}t} = \eta_{free} \cdot (1 + 2K\tau_0)^{-1} \tag{1.62}$$

producing a wide transmission peak (Fig. 1.62). Finally the small influence of the laser cavity distance L_D (with corresponding round–trip time τ_D) on the frequency ω

$$\frac{\mathrm{d}\omega}{\omega} = \frac{\pi^2}{F_0^2} \frac{\mathrm{d}\tau_D}{\tau_D} \tag{1.63}$$

reduces the effect of the mechanical vibrations on the transmitted signal. To summarize when handled properly OF can by used to efficiently couple the lasers with HFC. The limitations are mainly in controlling the phase and the amount of OF. In order to obtain smooth transition for each HFC mode the distance between laser and cavity has to be hold constant during the frequency scan. If level of OF is too strong it may induce mode hops or event perturbation in laser operation. As a consequence depending on used source OF has to be limited to prevent such behaviour.

1.3.2 Some examples of spectroscopy techniques exploiting HFCs

In order to determine the absorption inside the HFC we found two main measurable quantities - the ring down τ (Eq. 1.57) and the transmittance H (Eq. 1.23). This fact is used to define two principal categories of spectroscopic methods exploiting HFCs. It is the Cavity Ring–Down spectroscopy (CRDS) aimed to RD measurements and the Cavity Enhanced Absorption Spectroscopy (CEAS) exploiting the transmittance function for α determination. In further text I describe some of spectroscopic methods and their application related to the subject of this thesis.

Cavity ring-down spectroscopy of singlet oxygen generated in microwave plasma.

The goal of the experiment performed at Department of Experimental Physics in Bratislava in the team of Doc. Macko and prof. Veis (including me) was to

measure the $b^1\Sigma_g^+$(v=1)-$a^1\Delta_g$(v=0) molecular oxygen transition, about which there was only few data available [95]. The details of this work have been published in [22]. This part summarizes the results focusing on the aspects of used spectroscopic technique.

Cavity ring-down spectroscopy is one of the oldest techniques exploiting HFCs. The key element in the technique is the light source interruption producing the exponential decay of light stored inside the resonator (as shown on figure 1.24). The original concept of CRDS developed by O'Keefe and Deacon used pulsed lasers achieve fast interruption [61]. Later in 1996, Lehmann proposed the use of continuous wave (CW) lasers to improve both the frequency and space mode matching [44]. The CW–CRDS scheme used for the singlet oxygen detection followed the one developed by Romanini et al. initially for the dye lasers [73] and external cavity lasers [74] and later adapted to the fibred telecom distributed feedback lasers [57].

The experimental setup (Fig. 1.28) consisted of a microwave singlet oxygen generator with gas output guided through the optical resonator. The detection part of the experiment consisted of a fibred butterfly-package DFB laser coupled into this resonator through an acousto-optic modulator(AOM) capable of fast (below 1 μs) and efficient(extinction ration over 60 dB) laser off and mode matching optics. The resonator (of 60 cm length) was composed of two high reflectivity mirrors (made by Layertec, measured reflectivity 99.993 % at 1505 nm) in a vacuum-tight glass cell. To achieve frequency overlap at given laser frequency the cavity length was modulated over a distance greater than $\lambda/2$ by mounting one of the mirrors on a piezo-electric tube. The output was monitored by an InGaAs photodiode. Once the light was effectively coupled into the cavity signal rise occurred and when it exceeded the set threshold the beam was interrupted by use of the AOM. The highest advantage of the interruption by the AOM compared to switching off the laser current is its minimal influence on laser operation (frequency stability) therefore allowing high repetition rates.

The empty-cavity ring-down time was 28 μs and the ring–down event rate

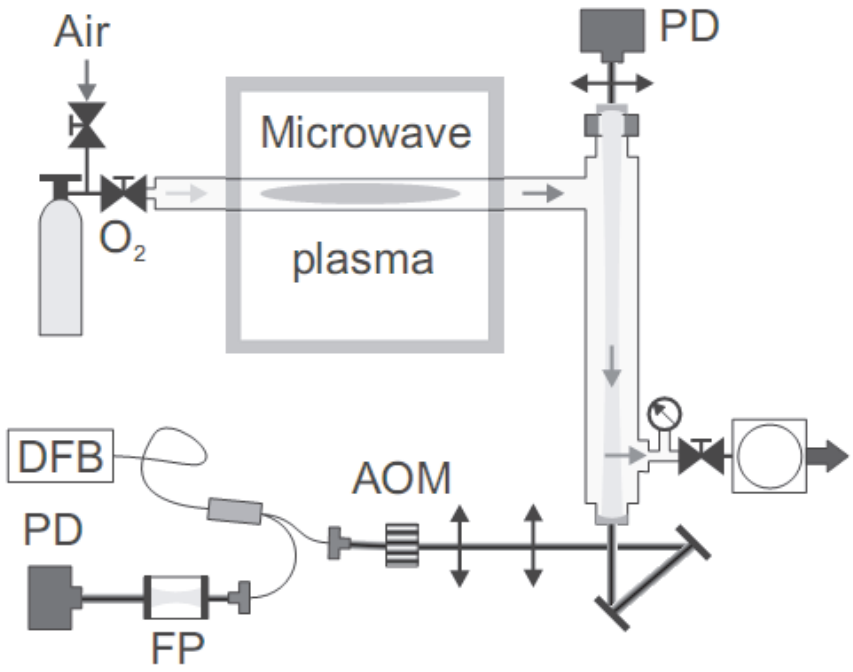

Figure 1.28: Scheme of a typical cw–CRDS setup, AOM—acousto–optical modulator, PD–photodiode, FPŰ–Fabry–Perot étalon, DFBŰ–distributed feedback laser.

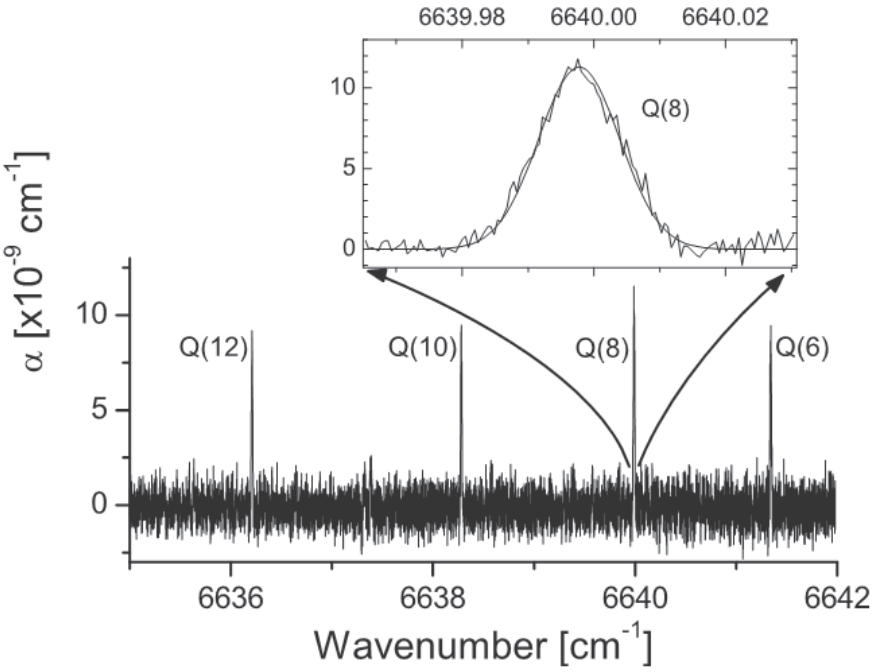

Figure 1.29: Part of the Q branch of $O_2(b^1\Sigma_g^+(v{=}1)\text{-}a^1\Delta_g(v{=}0))$ measured by CW-CRDS. The $O_2(a^1\Delta_g)$ density and the rotational temperature were $(4.6{\pm}1.0){\times}10^{15}\,\mathrm{cm}^{-3}$ and (296±5)K, respectively.

was about 500 Hz. Each ring-down event was fitted using a non–linear Levenberg-Marquardt method to a single-exponential decay function. Typically, 500 ring-downs per spectral point were fitted and their mean characteristic decay frequency was recorded. The laser was temperature tuned. The exact laser frequency and tuning rate were determined using known water absorption features (using the HITRAN database ([76])) and a Fabry-Perot étalon (FSR:986MHz). We succeeded in measuring 21 new spectroscopic transitions that we assigned to the O, P, Q and R branches of the $b^1\Sigma_g^+(v{=}1)\text{-}a^1\Delta_g(v{=}0)$ system. From the line intensities we obtained the density of $O_2(a^1\Delta_g)$ around $5{\times}10^{15}\,\mathrm{cm}^{-3}$ which means that 7 % of O_2 molecules were in singlet state (Fig. 1.29).

1.3.3 Cavity-enhanced absorption spectroscopy with a red LED source for NOx trace analysis

In this experiment the goal was to develop a simple, robust and low–cost detector based on a 643-nm LED which is of interest for the simultaneous detection of NO_3 and NO_2. The study was performed at Laboitoire de Spectrometrie Physique in collective of Dr. Romanini (including me) and published in [87].

In methods like CRDS the interaction is performed between a single FPR mode and a coherent light source. The effect of generally noisy character of the transmittance function on intra–cavity absorption measurement is reduced by the ring–down measurements (CRDS) or optical mode–locking (OF–CEAS). Another approach consist in reducing the interference of the intra–cavity and incoming electromagnetic field by minimizing the coherence of the input signal. Generally two methods are exploitable. In the off–axis Integrated–Cavity Output Spectroscopy (ICOS)[5, 65] a complex optical path inside of FPR (beam makes several round trips inside the cavity until it overlaps) to effectively suppress the cavity resonances. As a result, a minimum detectable absorption of approximately 1.4×10^{-5} cm^{-1} over an effective optical path of 4.2 km was initially obtained [5]. More recent experiments show the demonstrated the detectable sensitivity of 2.8×10^{-5} cm^{-1} [84].

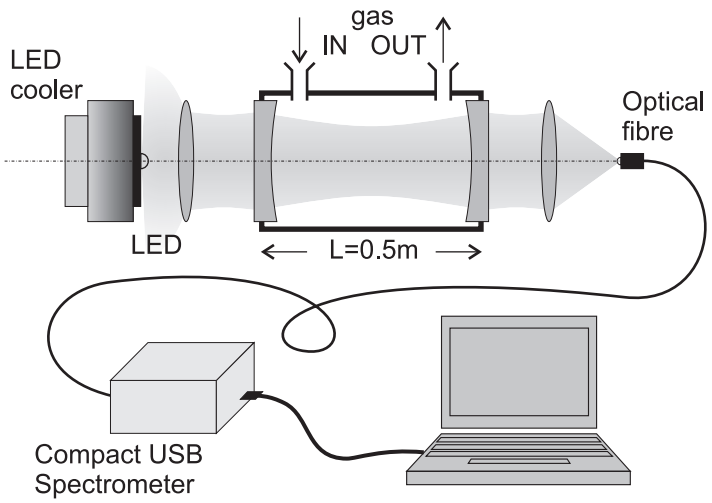

Figure 1.30: Optical layout of the LED-based IBB–CEAS setup.

The method presented in this work operates in the normal on–axis design and exploits the incoherent broad-band sources (IBB–CEAS). The transmitted signal is than integrated both in time and frequency by use of a relatively low resolution (compared to FPR FSR) spectrograph coupled a CCD (slow detector compared to the τ_{cav}). In the work we present a rigorous frequency-domain derivation of cavity transmission T_{IBB} as a function of wavelength for a broad-band spectrally smooth source, which complements the time-domain derivation by Fiedler et al.[21]

$$T_{IBB} = \frac{T^2 \exp(-\alpha L)}{1 - R^2 \exp(-2\alpha L)} \tag{1.64}$$

The transmitted spectra were retrieved by measuring with and without the sample filling the cavity, all other conditions being identical. The obtained function $s = T_{IBB}(\alpha)/T_{IBB}(0)$ could be inverted with respect to the sample absorbance (keeping only the solution making physical sense)

$$\alpha(\lambda) = -\frac{1}{L} \ln \left(\frac{R^2 - 1 + \sqrt{(R^2-1)^2 + 4s^2R^2}}{2s\,R^2} \right) \tag{1.65}$$

The optical layout (Fig. 1.30) was formed by the LED light source, optical resonator, fibred grating spectrometer and coupling optics. The LED emission was centred at 643 nm, with about 190 mW power. About 10 mW of this power was focused into the cavity by short focal lens. The cavity mirrors (50 cm radius of curvature), had a maximum reflectivity of 99.92 % at around 630 nm. The output light was focused into the multimode fibre connected to a low–resolution spectrometer (Stellar Net EPP2000, FWHM resolution 1.85 nm) controlled by a PC through a USB connection.

In order to determine sample absorbance directly from equation 1.65 we measured the cavity mirror reflectivity spectrum $R(\lambda)$. We employed a Perkin–Elmer spectrophotometer to obtain this mirror transmission profile. In figure 1.31 there is a comparison of the absorbance spectrum (1000 averages) for our 8.24 ppmv NO_2 sample with a spectrum calculated from a high-resolution, high-quality NO_2 optical cross section [89]. The latter is convoluted with a

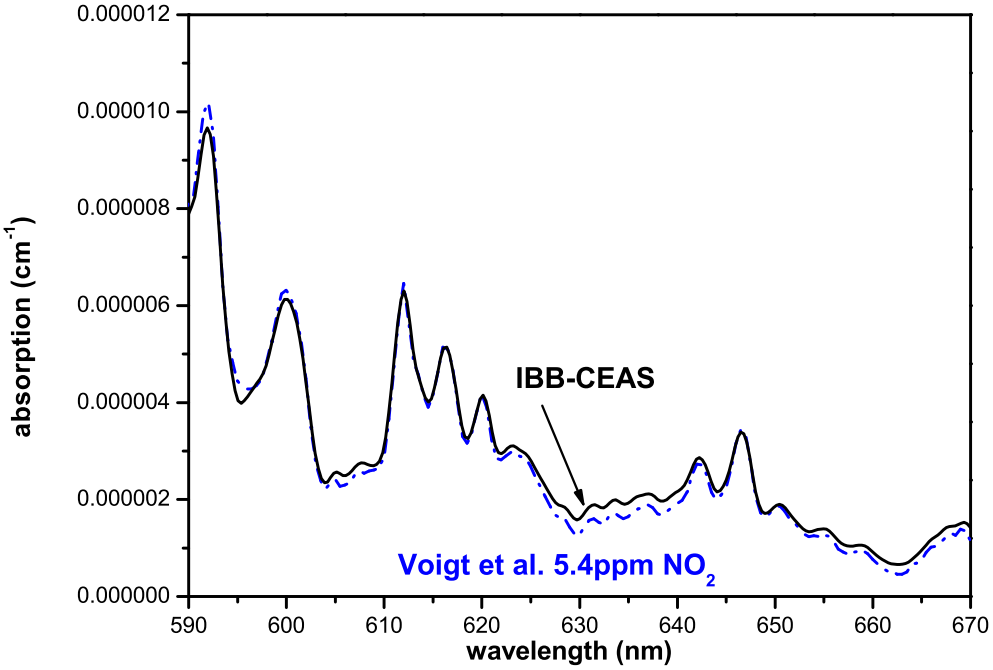

Figure 1.31: Comparison of an absorption spectrum obtained by IBB-CEAS (averaging 1000 spectra) with a spectrum calculated using a reference NO_2 absorption cross section by Voigt et al. [89], after convolution with a 1.85-nm FWHM Gaussian simulating our spectrometer response function. This ref- erence spectrum is scaled for a NO2 concentration of 5.4 ppmv, which optimizes the match with the observed spectrum

Gaussian of 1.85 nm FWHM to account for our instrumental function, and scaled for a concentration of 5.4 ppm that gives the best match with our IBB-CEAS spectrum (also shifted by 0.66 nm to compensate for spectrometer calibration error). The agreement is excellent over about 80 nm, from 590 to 670 nm, but for a concentration about 35 % lower than the certified value of our sample. This could be explained either by high reactivity of NO_2 with the steel walls of gas–handling system or by the offset in the mirror reflectivity determination due to the optical loses. A constant loss of about 5×10^{-4} needed to be included in the determination of R from T (R = 1-T-Loss), which seemed to be somewhat larger than expected for our mirrors, but still acceptable.

The sensitivity of our setup was estimated to be about $5\times10^{-9}\,\mathrm{cm}^{-1}$ for

average of 1000 spectra in the range of 615 to 655 nm (depending on the center of LED emission). The study showed high perspective of this technique notably achieving very good detection limits comparable with some CRDS experiments.

Chapter 2

Spectroscopy of dielectric barrier discharge

2.1 Introduction

In past years plasma enhanced technologies emerged rapidly into variety of applications like surface treatments, pollution control, ozone production, UV light source, *etc.*. Among large number of plasma schemes those working at high pressures (close to atmospheric) are of particular interest both for their physical properties and for no need of extensive vacuum pumping designs (often expensive and with a complicated implementation into production line). For uniform and non-destructive applications the discharges with homogeneous distribution of active species and low thermal excitation of heavy particles (atoms, ions or molecules) are of a great interest. Therefore a lot of research and development has been focused to the investigation of possibility to generate such *"cold–plasma"* discharges and their detailed characterisation.

The key aspect in achieving the diffuse character of the discharge is the control over the discharge current. At high pressures the formation of very short time ($<$100 ns) and localized (diameter bellow 200 μm) current filaments, so called micro-discharges or the transition into arc are more probable than the homogeneous discharges (on the timescale comparable with the applied voltage period). Several approaches are possible to obtain the diffuse regime (free of micro-discharges and arcs) for example by the reducing the heating of

the cathode and preventing to arc transition by supersonic gas flow through the discharge zone. Disadvantage of this technique is the instability of the discharge due to the fact that the residence time of the gas in the discharge zone is comparable to the time necessary for the discharge initialisation [6, 7, 23]. In the dielectric barrier discharge (DBD) a dielectric barrier is placed into the reactor to maintain current densities below the arc transition threshold (Fig. 2.1). The dielectrics surface acts as a charge trap during the voltage pulse generating a self-induced field in the gas gap that inhibits the discharge before the current densities exceed the threshold. Also by properly controlling either the breakdown phase (e.g. by enhancing the electron emission from the cathode compared to the effective ionisation rate of gas) or by the discharge development (e.g. by discharge current limitation by inserting a choke coil or resistance in the discharge electric circuit) the homogeneous character of the discharge could be obtained [51].

A broad study of DBD properties concerning filamentary or diffuse character of the discharge, investigation and modelling of its physical and chemical properties and application has been done by Massines et al. e.g. [29, 50, 52, 53]. There are also other publications dedicated to electric or spectroscopic simulation of DBD e.g. [11, 94].

In this work we focused on the comparison of two types of DBD with respect to the production of excited states of nitrogen mainly the $N_2(A^3\Sigma_u^+)$ metastable state. As showed by Simek et al. [80–82] or by Gherardi et al. [28] simultaneous observation of emitted spectra could by used as an efficient monitoring tool for discharge behaviour (metastable states concentration). In the second part of work we were investigating the possibility to use our DBD reactor for the singlet oxygen production. To detect the state we were measuring the infrared absorption spectra in the DBD afterglow similarly as we did in the afterglow of a microwave discharge [22].

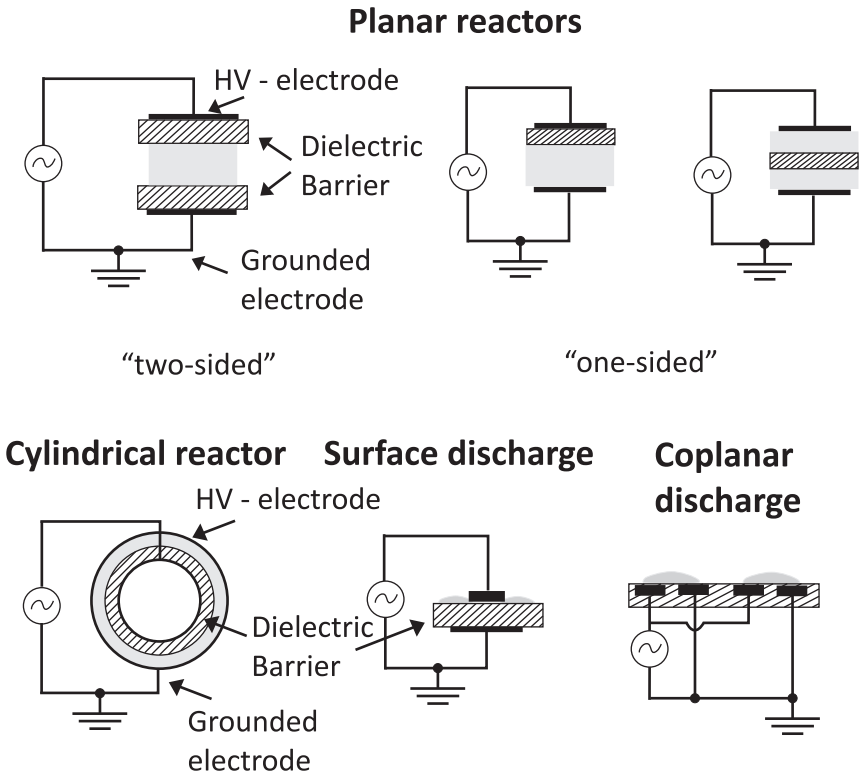

Figure 2.1: Common DBD schemes according to [90].

2.2 Experimental

A simple scheme of our experiment is presented in figure 2.2. The setup was designed to achieve variable conditions for discharge generation at different pressures, gas flow, input power and discharge configurations. Gas was injected into the system after the flow regulation just over the discharge gap. The output was situated on the opposite side of the reactor. A system composed of a pressure gauge, a regulation valve and a rotational pump was used to control the pressure from 0.1 to 2 atmospheres.

2.2.1 Discharge reactor

The discharge reactor (Fig. 2.3) had a rigid steel construction suitable for both low and high pressure (up to 2 atm.) measurements. The discharge was generated between two parallel electrodes covered by Al_2O_3 dielectric barriers. We used two shapes of barriers first in a form of a round cup (with 2 cm bottom

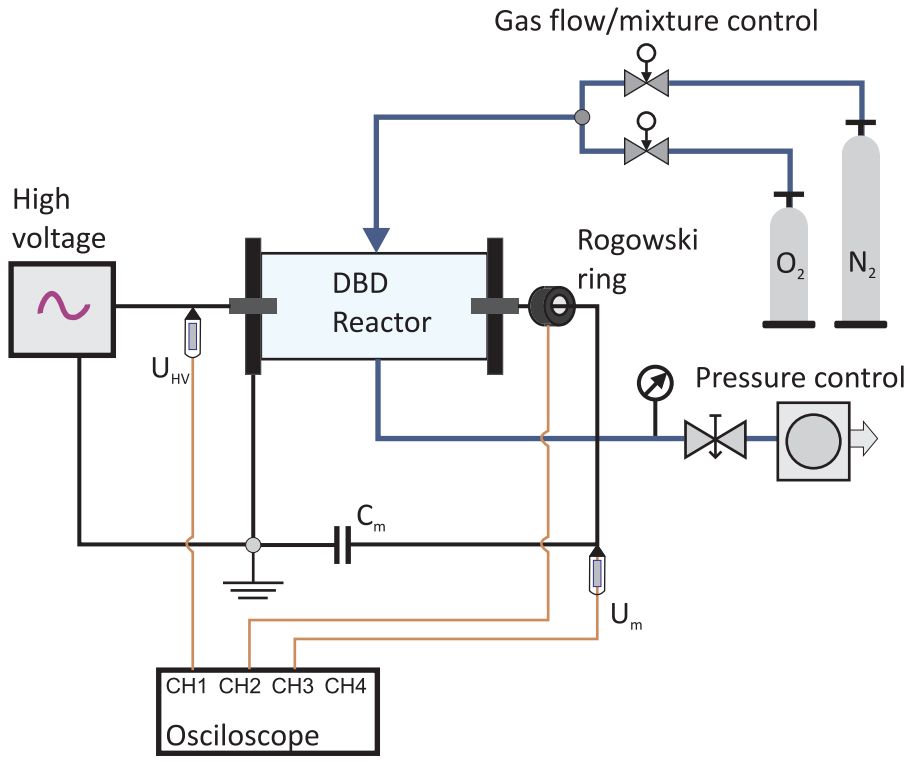

Figure 2.2: Experimental scheme of DBD. C_m is the charge transfer measuring capacitor, U_{HV} is applied high voltage measured by the 1:1000 probe and U_m is the drop of voltage on the C_m capacitor.

diameter and 2 mm dielectric thickness) and second in a form of a 1 mm thick plate. The length of the discharge gap was variable up to several mm.

2.2.2 Power supply and measurements

For powering the discharge we used a sinusoidal high-voltage generator operating at the frequency of 4.85 kHz with a single-ended electrode connection (one grounded electrode). The applied voltage U was measured by a high voltage (1:1000) probe.

A Rogowski ring (LILCO 13G-1000, 10 ns rise time) was used to monitor the discharge current behaviour. The power consumed by the discharge was monitored by a capacitor (150 nF) connected in series with the DBD (Fig. 2.4. According to the theory based on the equivalent electronic circuit of the DBD described in [90] (Fig. 2.4) the consumed power in the discharge is determined by the area of the transferred charge Q and applied voltage U diagram (in

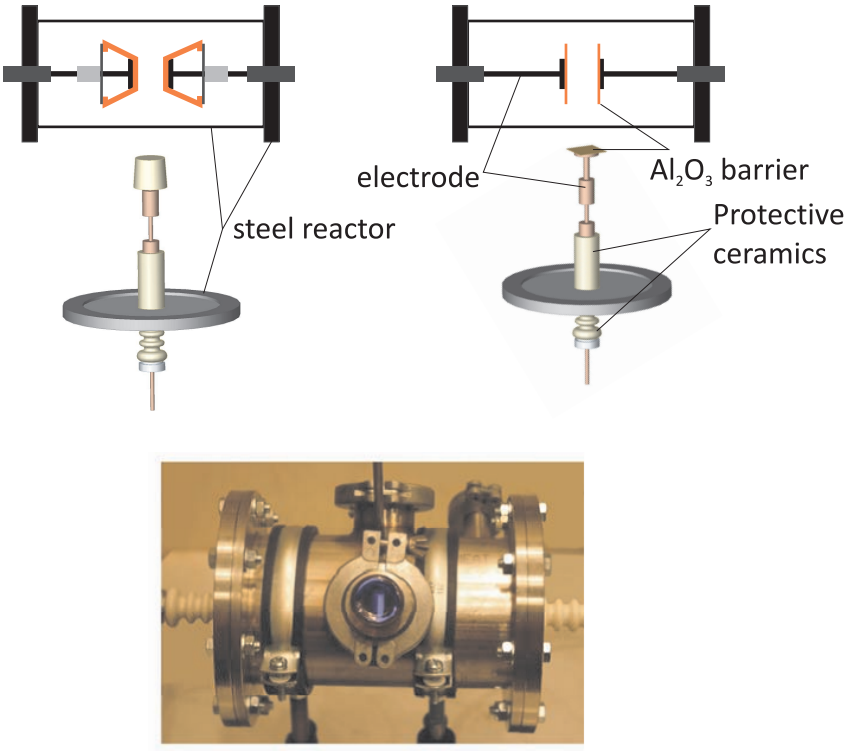

Figure 2.3: DBD reactor with two types of dielectric barrier used.

the form of Lissajous figure). Furthermore from the measurement of U_{min} the discharge voltage U_D could be retrieved as

$$U_D = U_{min} \cdot \frac{1}{1 + C_{gap}/C_{bar.}} \tag{2.1}$$

where C_{gap} and $C_{bar.}$ are the capacitances of the discharge gas gap and of the electrodes barriers, respectively.

2.2.3 Optical Coupling

To perform the spectroscopic measurements we used two types of detection schemes (Fig. 2.5). First to characterize the discharge composition the FBES method was used. In the second part the CRDS technique was used to monitor the singlet oxygen production.

The light emitted from discharge passed through a MgF_2 window and was focalized by a MgF_2 lens into the optical fiber connected to the Andor Mechelle-5000 spectrometer coupled with an intensified CCD camera (Andor iStar DH

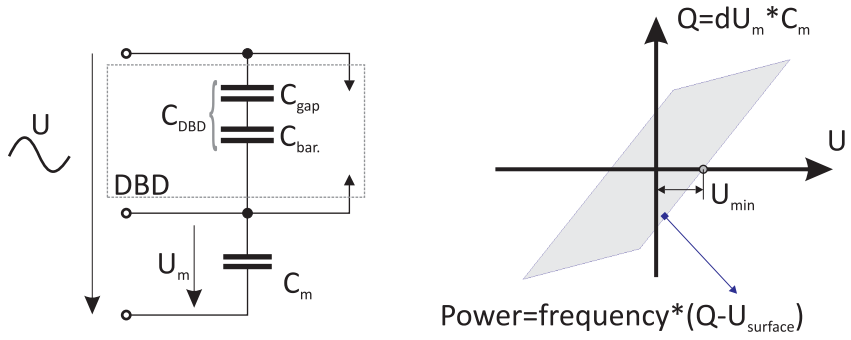

Figure 2.4: Equivalent scheme of DBD setup and the Q-U diagram.

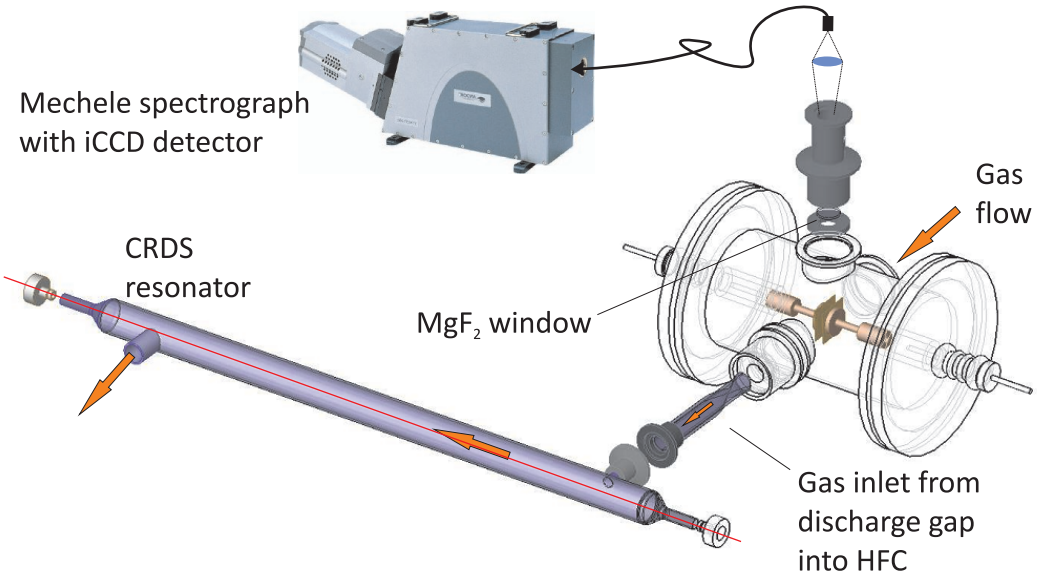

Figure 2.5: Optical layout of the DBD experiment. The parts are disassembled for better clarity.

734). Spectral acquisition was made in the range from 200 nm to 900 nm with a resolution $\Delta\lambda/\lambda$=4000. The iCCD gate was controlled with an external analogue trigger synchronized by the applied voltage.

The CRDS detector was the same as we described in the introduction (see Fig. 1.28). To connect the DBD we reversed the pumping direction and the gas was introduced to the cavity through thin inlet slit placed next to the discharge zone.

2.3 Results and discussion

In the first part we focused on the investigation of properties of the discharge formed between the two types of electrodes. Here we present four sets of measurements. All data were acquired at atmospheric pressure in pure nitrogen with impurities of oxygen. The case A corresponds to the thick cup electrodes with the gap of 2 mm. The B,C,D cases were done with the thin plate electrodes and the discharge gap of 1mm for different value of applied voltage. The measured power were 7.1 W, 6.3 W, 8.6 W and 2.9 W in A,B,C and D cases respectively (Fig. 2.6).

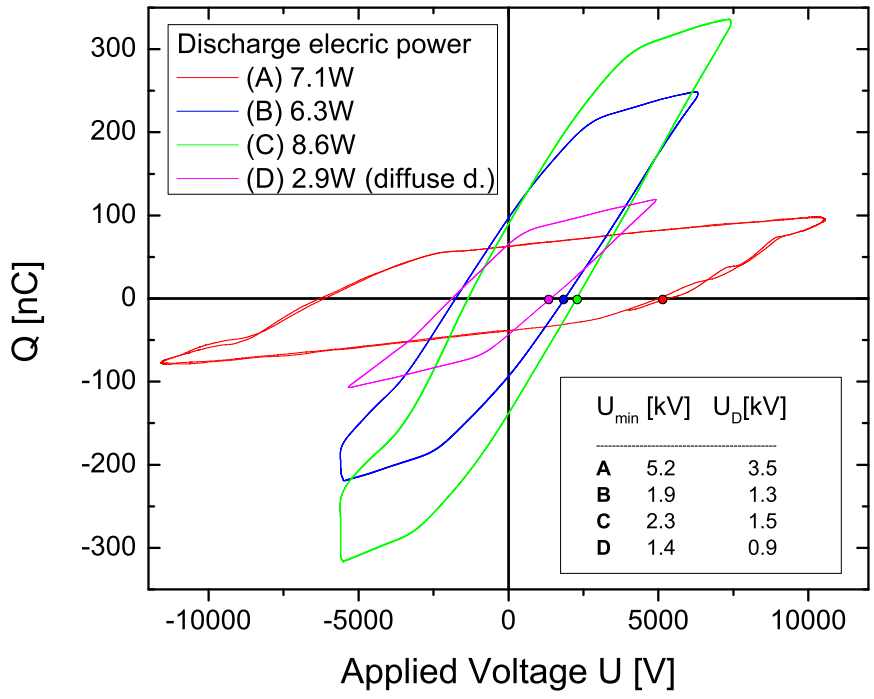

Figure 2.6: Measured DBD power by integrating the Q-U dependence (Lissajous figure).

The measurements of the discharge current (Fig. 2.7) showed that we produced the diffuse discharge only in the case of thinner barriers. Experimentally we determined that the U_D threshold needed for the diffuse-to-filamentary discharge transition was around 1 kV (case D). According to the volt-ampere

characteristics (no cathode fall was observed after the discharge ignition) and discharge power density (about $1\,\mathrm{W.cm^{-3}}$) we could assume that we had a Townsend DBD (also known as atmospheric pressure Townsend discharge - APTD) [51]. Further increase of the applied voltage over the 1 kV threshold led to the filamentary mode of discharge (cases B,C). For the thicker electrodes we were unable to produce the diffuse discharge mainly due to the thickness of the barriers forming together 4 mm of ceramics in the discharge gap (case A).

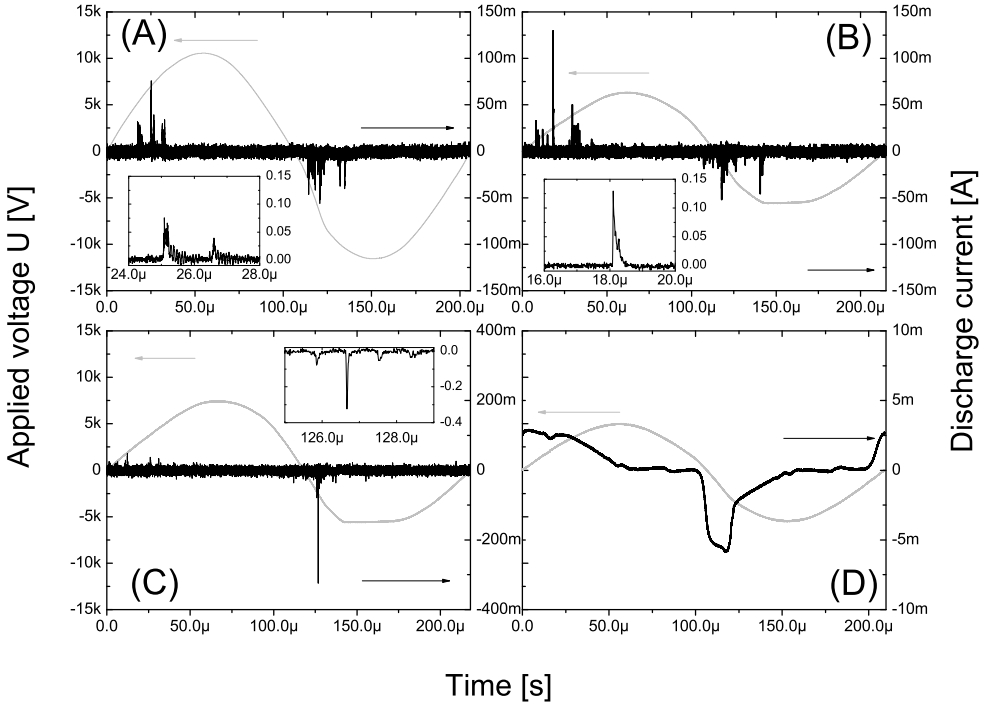

Figure 2.7: DBD current with respect to applied voltage as measured by the Rogowski ring. In the case D we observed the discharge in the diffuse mode.

The spectral acquisition was made in consecutive 5 μs windows for a whole period ($\sim$200 μs). In the acquired spectra two pure nitrogen systems the 2^{nd}positive (2PS, Eq.2.2) and the Herman-infrared (HIR, Eq.2.3) were observed. Thanks to the presence of impurities the NOγ (NOγ Eq.2.4) and Green (O-N_2) O(^{1}S)N_2 $\rightarrow$ O(^{1}D)N_2 at 557 nm transition were also recognized

(Fig. 2.8).

$$N_2(C^3\Pi_g) \rightarrow N_2(B^3\Pi_g) + h\nu(2PS) \quad (2.2)$$

$$N_2(C''^5\Pi_u) \rightarrow N_2(A'^5\Sigma_g^+) + h\nu(HIR) \quad (2.3)$$

$$NO(A^2\Sigma^+) \rightarrow NO(X^2\Pi^+) + h\nu(NO\gamma) \quad (2.4)$$

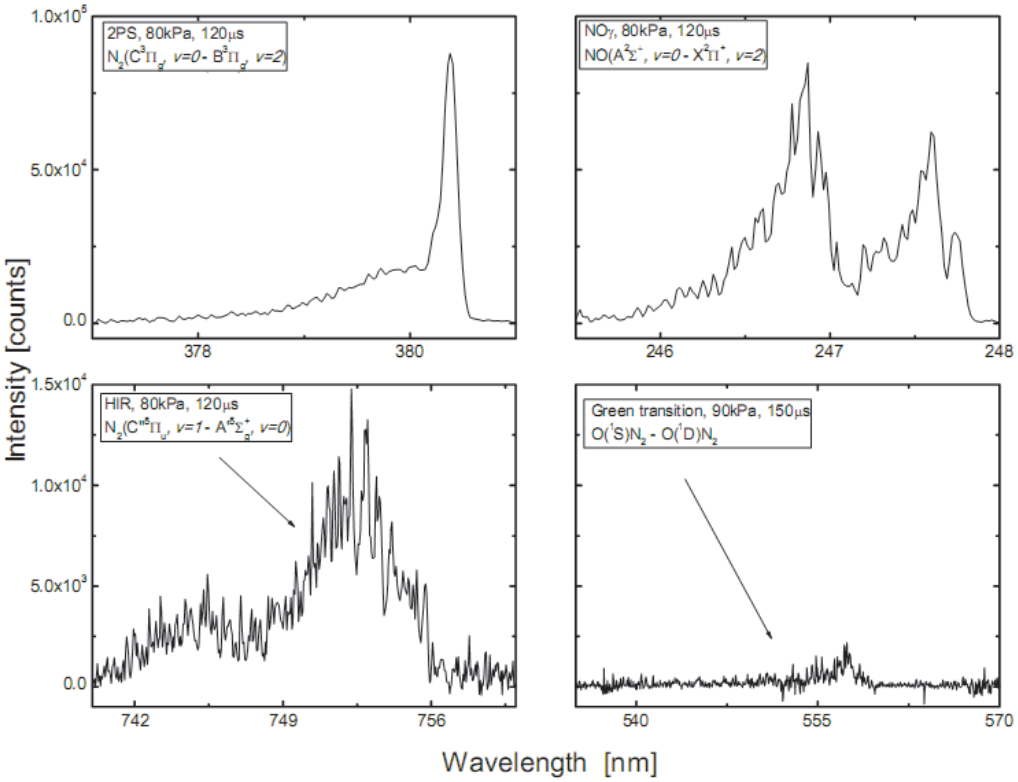

Figure 2.8: Example of observed spectra.

Emissivity of systems was monitored through a non-perturbed vibrational band lines (due to emissions from different species or Mechelle orders crossings) so we could obtain their time evolution over one period the sinusoidal discharge high voltage for all systems except for the Green transition where the noise dominated over the emissivity signal(Fig. 2.9). The spectra were normalized to the 2PS(v'=0, v''=0) ro–vibrational band. According to Simek et al. [82] the square root of the HIR emission is proportional to the $N_2(A^3\Sigma_u^+)$ concentration. Following this assumption we see that most of the metastable was produced in the case A where significant emission from HIR system occurred during both

half-periods of the applied voltage.

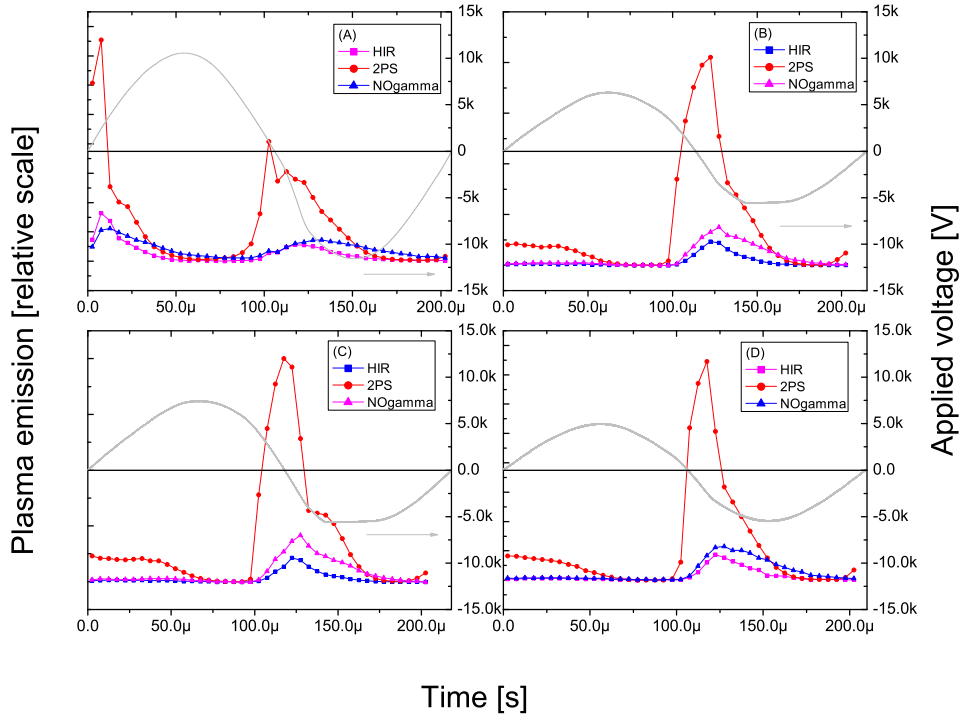

Figure 2.9: Emission of Herman infrared, 2nd positive and NOγ for two types of electrodes (A and B,C,D).

In the last part we used the DBD reactor with the A-case electrode to produce singlet oxygen in the oxygen-helium mixtures. To facilitate the detection the system was differentially pumped allowing us to have 100 torr pressure inside the CRDS resonator and about 450 torr pressure in the DBD reactor. The gas mixture was composed of 200 sccm O_2 and 6100 sccm He. Figure 2.10 shows measured absorption spectra around the position of the Q(10) line (spectra recorded with microwave discharge are on the background to facilitate the transition recognition). On top of the water lines we detected a very weak line near the expected position of the Q(10) line. However, as its low amplitude is comparable to the background noise we can hardly prove any formation of singlet oxygen in the DBD.

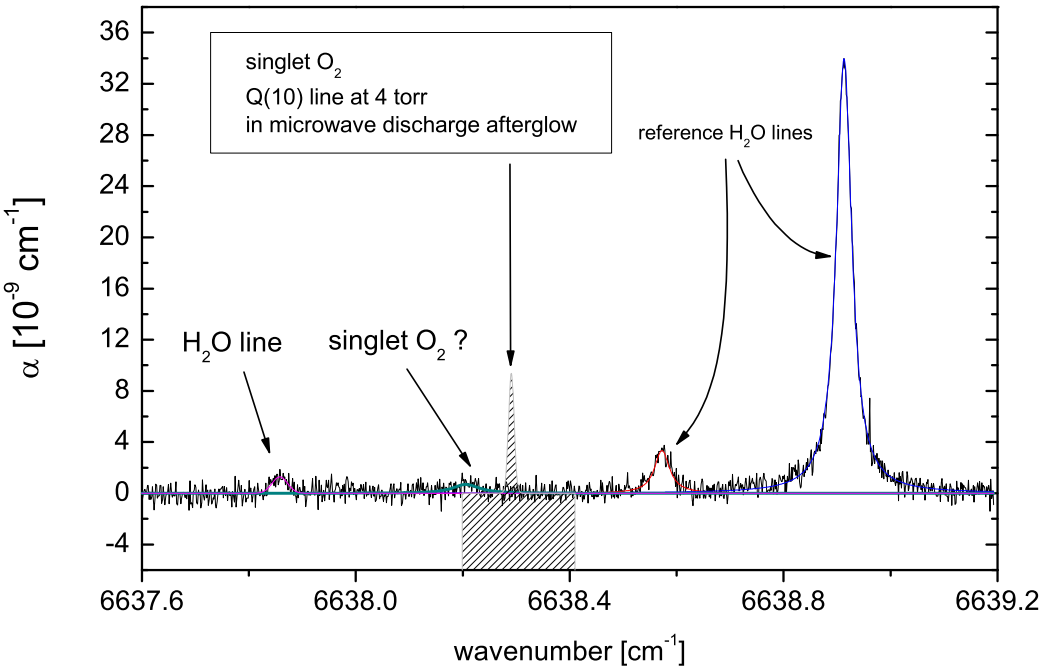

Figure 2.10: Measured DBD afterglow CRDS spectra at 150 torr total pressure in the CRDS cavity and 450 torr pressure in the DBD reactor. The gas mixture was composed of 200 sccm O_2 and 6100 sccm He. The fitted peak at 6638.21 is a good candidate for the Q(10) line of the singlet O_2 transition. The residual water lines are fitted by HITRAN and correspond to water abundance of 0.26 ppm.

2.4 Conclusion

To compare the production of the excited states of nitrogen, mainly the $N_2(A^3\Sigma_u^+)$ metastable state, we investigated the behaviour of discharges with two different thicknesses of the barrier. We were able to generate the diffuse mode of the discharge only when using the 1 mm barriers and 1 mm gas gap. From the voltage-current behaviour we determined the character of the discharge to be Townsend. This means we did not create plasma inside the reactor. This result is in coherence with experiments with similar parameters (e.g. [51]). The production of the $N_2(A^3\Sigma_u^+)$ metastable state was monitored through the relative emissivity of the HIR system compared to the 2PS and the NOγ systems. Its highest production was found in the case of 2 mm barriers and 2 mm

gas gap. It was mainly due to higher discharge voltage, which was about twice as high as in the case of thin barriers.

Although the diffuse regime of the DBD offers a homogeneous distribution of active particles, their higher production is achieved in the filamentary regimes where higher powers could be delivered to the discharge. Following this results in the second part we tried to measure the singlet oxygen production in the configuration with thicker barriers on the electrodes. Using our CRDS setup we were not able to detect any singlet oxygen absorption above $5 \times 10^{-10}\,\mathrm{cm}^{-1}$ which was our detection limit (Fig. 2.10). We assume that the main reason for not observing its presence was due to its collisional de-exitation on the way from the DBD discharge to the CRDS detector.

Chapter 3

VECSEL based spectrometer

3.1 Introduction

The region around 2.3 μm is of particular interest for spectroscopic investigation. Present absorption lines of water and carbon dioxide are sparse and weak causing little interference to other atmospheric trace molecules. Indeed, known as H_2O or CO_2 "absorption window", this region is very suitable for *in situ* absorption measurements. For example together with water vapour we can detect the presence of two other greenhouse gases. These are the third most important greenhouse contributor – methane [39] and nitrous oxide currently considered as the dominant ozone-depleting substance emitted by humans [70]. Among other pollutants ammonia and hydrogen fluoride are also observable in this region. Secondly the well resolved spectroscopic data from weak molecular transitions from this part of spectra are important for complementing spectroscopic databases such as HITRAN [76] or confronting recent theoretical predictions like the CDSD for CO_2 [85]). Subsequently this knowledge could be used for example in global modelling of Earth atmosphere [39] or interpretation of astronomical measurements (e.g. [83, 86]). A good example is the observation of CO on Venus and Mars. Firstly discovered in 1968-69 by Connes et al. on Venus [14] and by Kaplan et al. on Mars [36], nowadays the CO2 window is the target of many space missions like Venus Express[1] with the VIRTIS (Visible and Infrared Thermal Imaging Spectrometer) instrument

[1] http://sci.esa.int/science-e/www/area/index.cfm?fareaid=64

on board. Figure 3.1 shows an overlay of two night side emission spectra of Venus around 2.35 μm acquired by the VIRTIS instrument (H and M stands for acquisition channels with different resolution). The color bar indicates three minor constituents in the lower atmosphere (CO, H2O and OCS) [49].

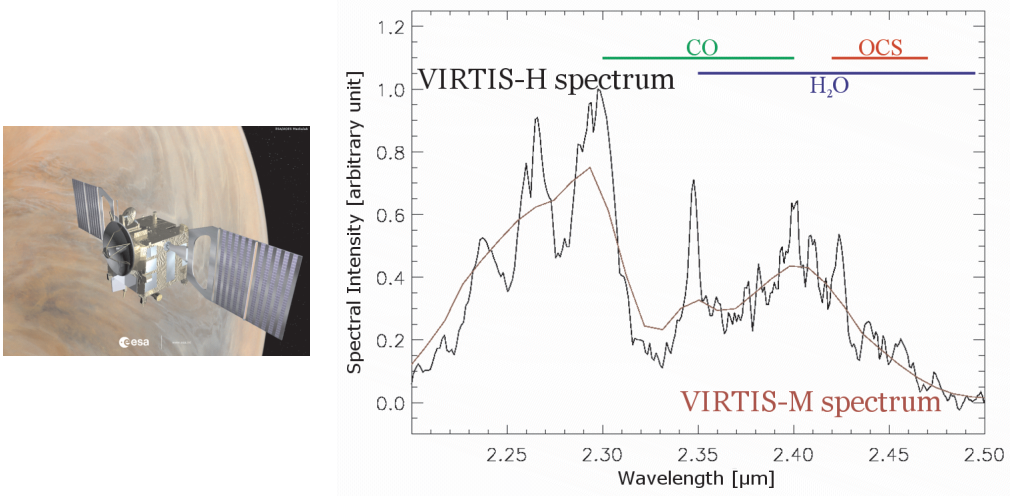

Figure 3.1: Example of Venus atmospheric spectra in the 2.3 μm region collected by the VIRTIS instrument on board the Venus Express mission [49].

Nowadays most of the laboratory spectroscopic measurements in this region are performed by Fourier transform spectroscopy (FTS) equipped with incoherent sources like glow bar or halogen light e.g. [91], [83] or [86]. FTS offers a broad band coverage with excellent frequency precision but has limited sensitivity and resolution compared to methods exploiting high finesse cavities (HFC) coupled with laser sources. Indeed in the past twenty years HFC in CRDS or CEAS like schemes demonstrated high performance in terms of absorption sensitivity, frequency resolution and precision. Narrowband continuous wave (CW) lasers with stable polarisation and Gaussian beam profile allow high injection efficiency into a HFC [34, 56]. Wide frequency operation range with the ability of (mode–hop free) continuous tuning of such sources allow well–resolved simultaneous absorption measurements of different chemical species. Finally compactness, low power requirements and room temperature (RT) operation are fundamental for the realization of portable instrumenta-

Parameter (CW,RT)	unit	OPO Argos▼	DFB MQW diodes★	μVCSEL†	VECSEL† L_{cav}=4 mm
Output power	mW	>1000	~ 5	~ 3	~ 3
Laser linewidth	MHz	<1	3	3	$<20\times10^{-3}$
Beam quality M^2	–	<1.1	$\sim 1.3\times3.5$	1.5	<1.2
Mode–hop free tuning	GHz	50	150	42	250
Total tuning	THz	>10	~ 0.7	0.6	1.4
Size	m	1	<.01	<.01	<0.1
Availability		on market	on market	prototype	prototype

▼ http://www.aculight.com
★ http://www.nanoplus.com
† [25, 63]

Table 3.1: Characteristics and state of development of some laser sources in the 2.3 μm region.

tion.

Among coherent sources capable of single transverse and longitudinal mode continuous wave (CW) operation suitable for such applications there are two principal technologies for the 2.3 μm region. These are the Optical Parametric Oscillators (OPO) and the Sb–based multiple quantum well (MQW) semiconductor lasers. In case of Sb–based sources there exists three main designs: distributed feedback (DFB) laser diodes, vertical surface emitting lasers (VCSEL) and external cavity VCSELs (VECSEL). Table 3.1 summarizes most important characteristics and state of development for each source.

From sources available on market the OPOs offers excel in all parameters but the continuous tuning range. The price we pay for such a performance is the size and the cost of the system. Compared to that the DFB laser diode is the most compact technology offering a mode–hop free tuning range twice as large. Recently Sb–based MQW DFBs proved their capability coupled with Optical Feedback (OF) CEAS detector [72]. A DFB laser based system was used for the simultaneous detection of CO, NH_3 and CH_4 in volcanic gases [37]. Compared to FTS, the OF-CEAS technique achieved about 100 times better performance with a detection down to $\alpha_{min.} \sim 1 \times 10^{-9}\,\mathrm{cm}^{-1}$. The drawback of system is a limited spectral range and frequency sampling. The spectral step is given by the fixed resonator length which for the cavity of 1 m to 2 m

gives 150 MHz to 75 MHz. This values are sufficient for the medium pressure trace detection (to 100 Torr) but prevent the technique to be used in more extensive spectroscopic studies at low pressures.

The VCSELs and VECSELs represent an interesting alternative to DFBs and OPOs. In particular the combination of stable external cavity and optical pumping for a VECSEL has a number of advantages over the electrical pumping with microcavity configuration of VCSELs. The structure does not need any heavy post–growth processing, carriers are generated directly in the gain zone which limits self-heating, and the use of undoped semiconductors reduces optical losses especially in the Bragg mirror [25]. As a result, we get very narrow linewidth, broad band coverage and a diffraction limited Gaussian beam profile in a relatively compact setup operating at RT in CW.

Garnache et al. [24] used the VECSEL structure with intra–cavity laser absorption spectroscopy (ICLAS) to enhance the sensitivity in this region. The ICLAS achieves similar performance as OF-CEAS in terms of detection limits $\alpha_{min.} \sim 1.5 \times 10^{-9}\,\mathrm{cm}^{-1}$ ($3 \times 10^{-10}\,\mathrm{cm}^{-1}/\sqrt{Hz}$) but the complex dynamics of laser—absorbent interaction render the the absorption line strengths determination unreliable. Also, ICLAS is laboratory spectroscopic technique, with complex and bulky setup (long cavity, high resolution spectrograph, *etc.*) and high power requirements.

In this chapter we present VECSEL development aiming at going beyond the drawbacks of DFB lasers currently employed in the OF-CEAS based detectors. The goal was to extend both the frequency operation and continuous (mode hop free) tuning range of a prototype unit in collaboration with Institut d'Electronique du Sud (IES) Montpellier (providing the VECSEL structure) in the frame of a ANR-financed project. A second step was coupling of the VECSEL with the HFC to create a OF-CEAS or CRDS like system. In the following I show the road we took from the theoretical background to VECSEL successful application in spectroscopy measurements.

3.2 VECSEL design and theory of operation

VECSEL belongs to the family of surface emitting lasers initially designed by Kenichi Iga [35]. It is composed by a 1/2-VCSEL semiconductor structure, an external mirror and an optical pump system (Fig. 3.2). The temperature stabilized 1/2-VCSEL structure contains the laser active layer on top of a high-reflectivity Bragg mirror. Due to the short length of the gain region compared to edge emitting lasers the total gain per pass is relatively low. To achieve the lasing condition a high quality resonator is needed. Therefore the open air cavity is formed by a high reflective (R $>$ 99%) dielectric mirror. The optical pump is placed independently on the laser resonator with its beam directly focused into the active zone of the 1/2-VCSEL.

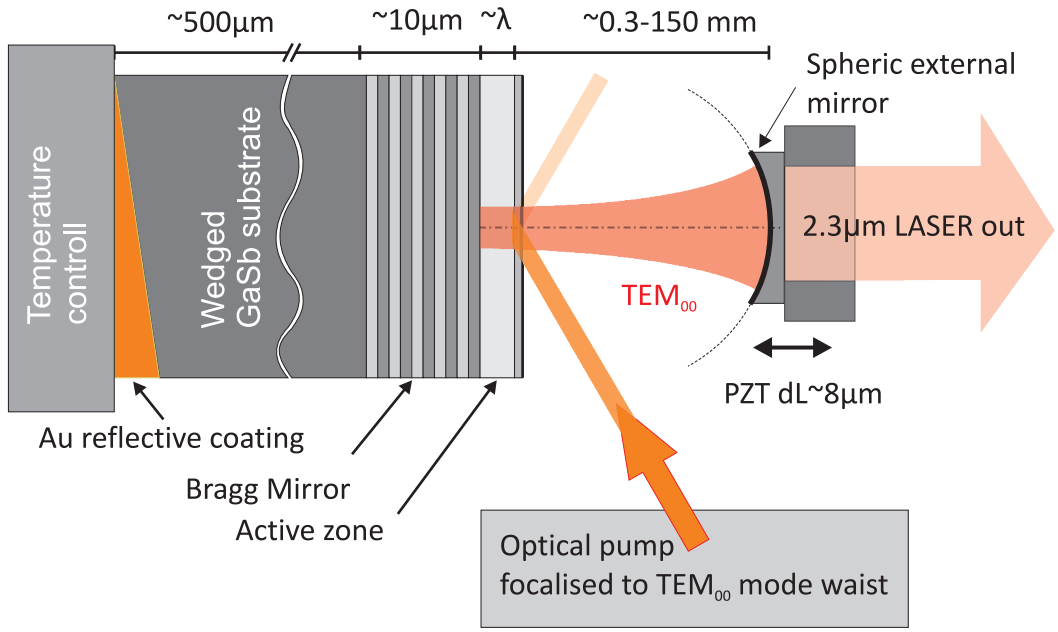

Figure 3.2: Scheme of the VECSEL setup.

The 1/2-VCSEL (Fig. 3.3) used in this work was grown by molecular beam epitaxy (MBE) on a 500 μm thick GaSb substrate. First on substrate is the 24.5 pairs Bragg mirror (8.1μm thick) with 99.9 % reflectivity. It is followed by the lambda long gain region. The active layer is formed by an AlGaAsSb/InGaAsSb type-I multiple quantum well (MQW) system capable

of emitting between 2 to 3 μm [46, 88]. Our 2.3 μm VECSEL contains 5 compressively-strained 10 nm thick $Ga_{0.65}In_{0.35}As_{0.1}Sb_{0.9}$ quantum wells, separated by 20 nm thick $Al_{0.35}Ga_{0.65}As_{0.03}Sb_{0.97}$ barriers located on the antinode of the electric field. The top of the design is composed by the $AlAs_{0.05}Sb_{0.95}$ layer acting both as a heat spreader and a carrier confinement layer. Finally a 5 nm GaSb layer is placed to protect against oxidation. The high electron and hole confinement in the wells (490 meV for the electrons and 170 meV for the heavy holes) ensures high quantum efficiency and high temperature operation. The barrier bandgap is 1.05 μm allowing efficient optical pumping with a commercial and low cost 0.8 to 1 μm laser diodes. The optical in-well pumping is also possible as was shown by N. Schulz et al. [79] but only with the help of $\sim$2 μm laser source which penalizes this approach. More detail on the structure or its fabrication may be found in [25, 27, 63].

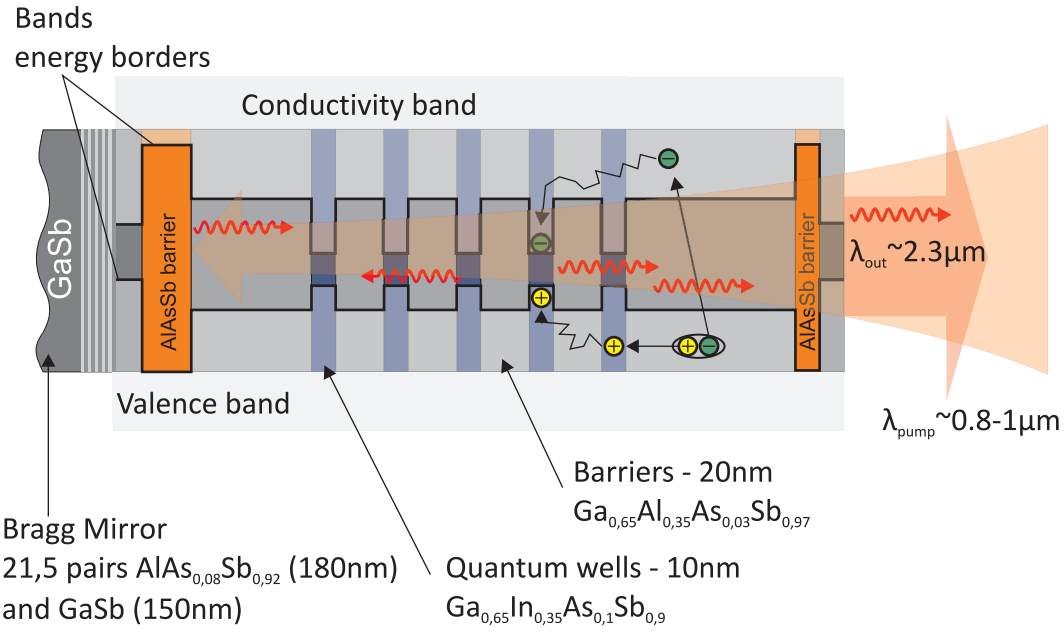

Figure 3.3: The detail of the 1/2-VECSEL structure with the description of the laser field build–up

3.2.1 Emission properties

To achieve single frequency operation the laser cavity has to oscillate on a single transverse (preferably TEM_{00}) and longitudinal mode with one selected polarisation state. In case of VECSEL the TEM_{00} operation is promoted by the stable plano–concave design of the laser resonator (1.42). In order to correctly describe the cavity modes the effect of the thermal lens induced on the 1/2-VECSEL by the incident pump beam has to be taken into account. For example Garnache et al. measured for with similar 1/2-VECSEL structure, 55 mW pump on 26 μm spot the thermal lens effect equivalent to concave mirror with curvature radius of about 8.5 mm [25]. To achieve both selective and efficient excitation of the cavity TEM_{00} mode, the pump beam incidence is set close to the Brewster angle and its projection onto the 1/2-VCSEL surface matches the waist of laser cavity TEM_{00} mode. The use of a half-wave-plate for adjusting the pump beam polarisation and an incident angle of around 70° resulted in more than more 90 % of pump power absorption and an almost circular pump region on the semiconductor surface. Choosing the dielectric mirror curvature and cavity distance we can then control the size of the VECSEL beam waist and through that the beam divergence. The VECSELs suffer to the natural instability of polarisation due to the circular symmetry of the cavity TEM_{00} promoting equally polarisation along both [110] and $[1\bar{1}0]$ crystal axis. To break this symmetry a slightly elliptic pump spot in the [110] direction is used to amplify the small gain difference along crystal axes and therefore stabilize a linear laser polarisation [25]. Finally the single longitudinal mode selection within the 4 THz wide gain (Fig. 3.4-b) is obtained by modal gain competition. To increase the efficiency of this process the active zone was designed as low finesse micro–cavity. This additional spectral filter about 700 GHz wide strengthens the single longitudinal mode operation [25]. To prevent the modulation of the gain curve due to parasitic reflections from the back of the substrate a wedge covered by an Au reflective coating is used.

Another important parameter is the linewidth of laser emission. As described in the first chapter it is a key element defining the character of the

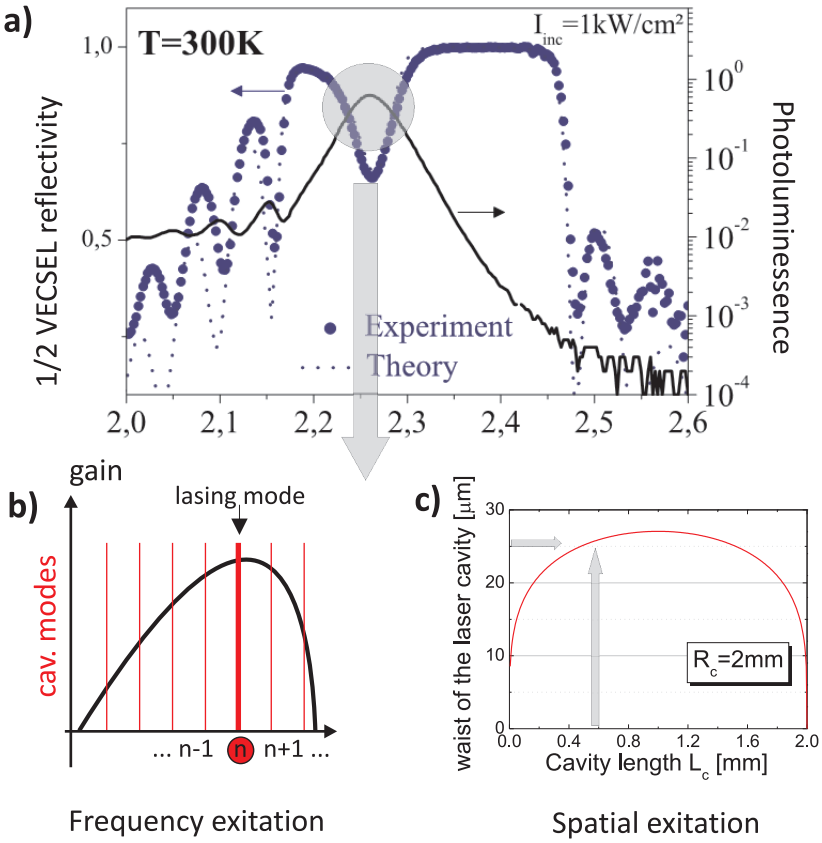

Figure 3.4: Principal parameters of VECSEL design determining the frequency of emission: a–Reflectivity (measured and calculated) and photoluminescence of the 1/2-VCSEL at 300K showing a good matching between total reflectivity and MQW gain wavelengths, taken from [25]. b–total gain function for cavity modes, maximum of the curve corresponds to the maximal frequency excitation for the closest cavity mode leading to laser operation at this mode frequency. c–size of laser beam waist as a function of cavity length for mirror with R_c=2mm

HFC laser interaction. According to the modified Schawlow and Townes (S.T.) theory [13] (where the phase–amplitude coupling is taken into account through the Henry factor α_H) we can calculate the linewidth of VESCEL emission as

$$\delta\nu = \frac{hc}{2\pi\lambda}\left(T_{ext}\frac{c}{2L_c}\right)^2 \frac{1}{P_{out}}\xi(1+\alpha_H^2) \tag{3.1}$$

where ξ is the spontaneous emission to stimulated emission ratio, T_{ext} is the external mirror transmittance. Using the values for 2.3 μm VECSEL $\xi = 1.4$, $T_{ext} = 1\%$ and $\alpha_H = 3$ according to [26] we obtain for 1 mW output power and 1 mm long cavity the linewidth about 500 Hz or 3 kHz for a 300 μm long cavity.

In practice acoustic and thermal noise limit the laser linewidth to the kHz level [42, 63] (for a 4 mm cavity). Anyway these values (specially for long cavity VECSELs) are orders of magnitude smaller than for the DFB or VCSELs and confirms the spectroscopic potential of VECSELs.

3.2.2 Frequency tuning

As described above the lasing frequency of VECSEL is determined by the frequency of the external cavity mode closest to the gain curve maximum (Fig. 3.4-b). Therefore the tuning of the laser frequency (Fig. 3.5) can be controlled by two principles. It is the position of the gain curve and modes of the laser cavity.

The shape of the active layer gain function is determined by the composition and dimension of the quantum well. Therefore the gain curve is sensitive to temperature variations. In this case the thermal tuning rate for the structure is about -75 GHz/K over about 1.4 THz range [25]. In practice, controlled change of temperature could be obtained either by the thermal regulation of the 1/2-VCSEL using a Peltier cooler coupled to a regulation PID circuit or by variation of pump power. The two approaches differ mainly in the response time. In case of pump power modification, the change of temperature is very fast (several μs) mainly due to fact that it is localized only on the small region of beam waist. Contrary to that, the Peltier controls the temperature of the whole system therefore needs some time to reach a given temperature setting (several s). The effect on the frequency is shown on the figure 3.5-a. The displacement of gain curve does not affect the emission frequency until the gain maximum moves closer to the next cavity mode, then the higher gain per pass for photons with this mode frequency will cause the laser "to jump" to this frequency. Globally we observe discrete steps in laser frequency across the whole operational range.

In the second case, the frequency of cavity modes is determined by the optical length of the cavity. To control it the external mirror is placed on a piezoelectric transducer. The variation of mode frequency with the cavity

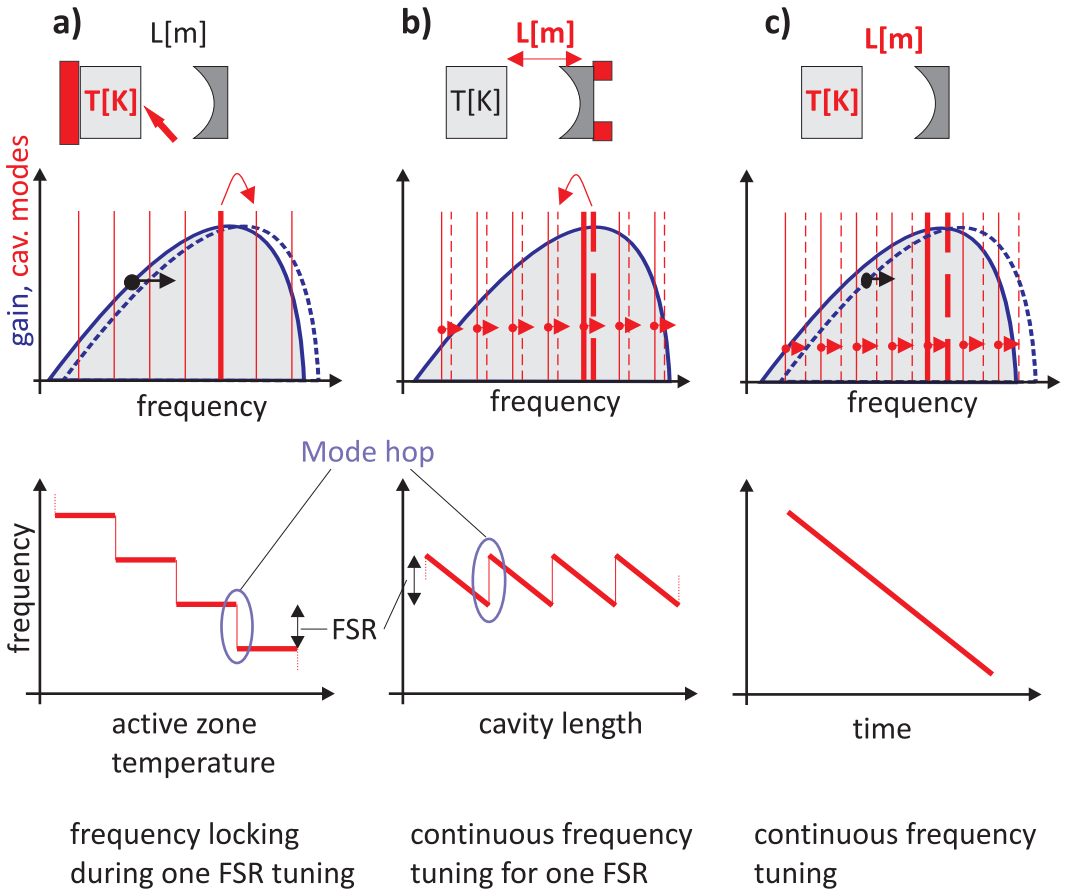

Figure 3.5: VECSEL frequency tuning. Unlike to DFB lasers [25] in VECSEL the tuning of active zone (a) is decoupled from the laser resonator length tuning (b), therefore broad mode-hop free tuning could be achieved by synchronizing both effects (c).

length could be deduced by differentiating the equation 1.38

$$\Delta\nu = \nu_{VECSEL} \cdot \frac{\Delta L}{L_c} \tag{3.2}$$

Figure 3.6 shows the tuning capabilities for resonators of different length. Contrary to the gain tuning case here the laser frequency follows the cavity mode, thus continuous tuning is observed (Fig. 3.5-b). Similarly to gain tuning a mod–hope appears when the gain becomes higher for a different mode. The spectral distance between mode–hops is one FSR of laser cavity. The frequency tuning pattern has then a form of sawtooth function with amplitude equal to the FSR and offset given by the position of the gain.

In practice Ouvrard et. al [62] showed that the continuous mode–hop free tuning of several times the FSR (220 GHz for 4 mm cavity VECSEL) could be also achieved by thermal induced gain tuning. This effect occurs due to the active layer non–uniform temperature distribution induced by the pump beam. As a consequence during the cavity length scanning (mainly when the cavity is in the close to a concentric limit geometry, $L \rightarrow R_c$) the variation of waist dimension changes the average temperature integrated over the waist surface, thus shifting the gain maximum frequency.

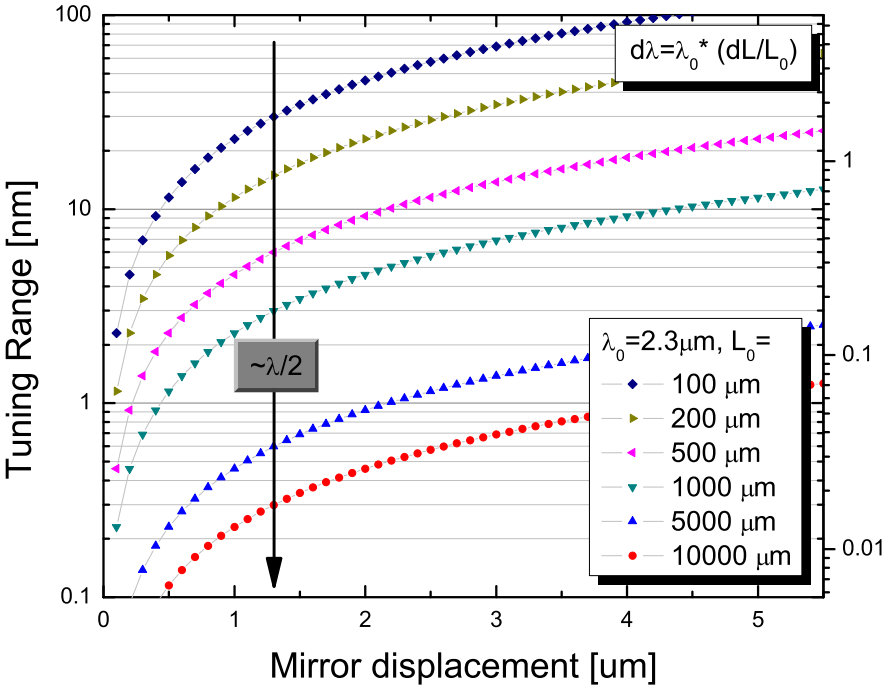

Figure 3.6: The effect of external cavity length on the frequency tuning range.

In VECSELs we have the possibility to achieve mode–hop free tuning across the whole operational frequency range by synchronizing both tuning of the gain and cavity modes (Fig. 3.5-c). In such case theoretically mode–hop free tuning ranges more than THz order are achievable (e.g. ΔT=20 K corresponds to 1.5 THz tuning) which about factor 10 larger than for a DFB diode (see Tab.3.1).

3.3 VECSEL construction and characterisation

In this section a chronological description of the VECSEL prototypes we developed is presented. The design of each one is placed into the context by analysing the characteristics of previous setups. Regarding the various parameters we initially focused on stable CW operation and broadband tuning. Later the character of HFC-VECSEL interaction was studied with respect to possible high sensitivity spectroscopic applications.

1.4mm cavity VECSEL

The starting point of development was a 4 mm long cavity VECSEL developed at IES at Montpellier by the collaborating group of Garnache et al. [25]. On this model we developed a VECSEL (Fig. 3.7) composed of the same Sb-based 1/2-VCSEL structure and a tiny external concave mirror (99.2 $\pm$ 0.25% reflectivity, 2 mm radius of curvature, custom design by BFI Optilas MI-2300-4-1.9-UV-2.089) mounted on a piezoelectric translator to form a lasing cavity about 1.4 mm long. We used a 20-mm diameter piezo tweeter disk, capable of displacements of about 8 μm for 20 V applied to it. The disk was glued around its edge to a ring mounted on a tilt stage. We made a hole at its center and glued the small cavity mirror inside. The 1/2-VCSEL structure was fixed onto a small copper plate using thermal paste, mounted on a thermoelectric cooling system trough which we could control its temperature.

Diode pumping was achieved using a commercial 830 nm single transverse mode laser diode (Sanyo DL7032) with about 100 mW output power. The pump beam was coupled into the active region via collimating and focusing lenses with focal lengths of 4.5 and 50 mm, respectively according to previously described pumping scheme. A gentle flow of dry nitrogen was used in order to flush the semiconductor surface continuously and minimize effects of condensation.

In order to monitor the output frequency behaviour of the VECSEL, we used an uncoated CaF_2 étalon (length 5 cm with FSR=2.1 GHz) and a 5 cm cell containing CH_4 at 1 Bar (also needed for demonstrating an absorption spec-

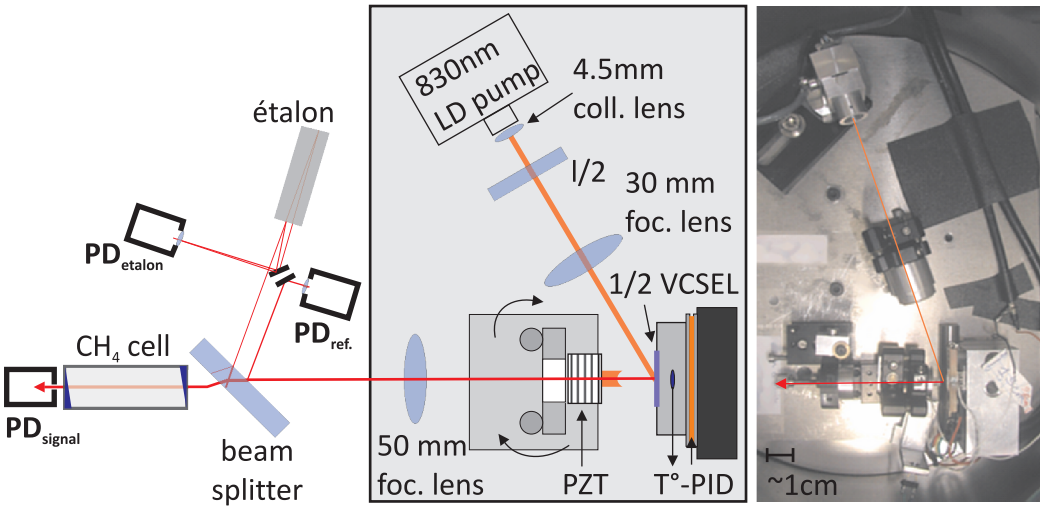

Figure 3.7: Scheme of experimental setup on left and photo of VECSEL on right.

trum). For a higher fringe contrast, we monitored the étalon signal in reflection as shown in figure 3.7. The signals from the étalon, through the methane cell, and a reference beam, were provided by 2.6 μm extended InGaAs photodiodes (Hamamatsu). We controlled the system and acquired signals using a digital-to-analog and analog-to-digital conversion card (National Instruments USB 6251). Standard Labview I/O routines were used to simultaneously control the setpoint voltage of the laser temperature stabilization electronics (home-made) and the external-cavity piezo disk voltage, while sampling signals from the photodiodes. Automatic mode-hops detection algorithms based on monitoring the continuity of the derivative of the étalon and methane absorption signals were implemented. For frequency scale relative calibration we used the étalon fringes, while comparison of the methane absorption spectrum with a HITRAN simulation allowed absolute frequency determination.

Emitted power was measured as a function of the chip temperature and of the 830-nm pump power (Fig. 3.8) using a calibrated thermal power meter (Melles–Griot,13PEM001 model). The maximum measured output power in CW operation was 2.8 mW at 5 °C with 140 mW maximum pump power. A roll–off at high pump power was observed only at higher temperatures. In

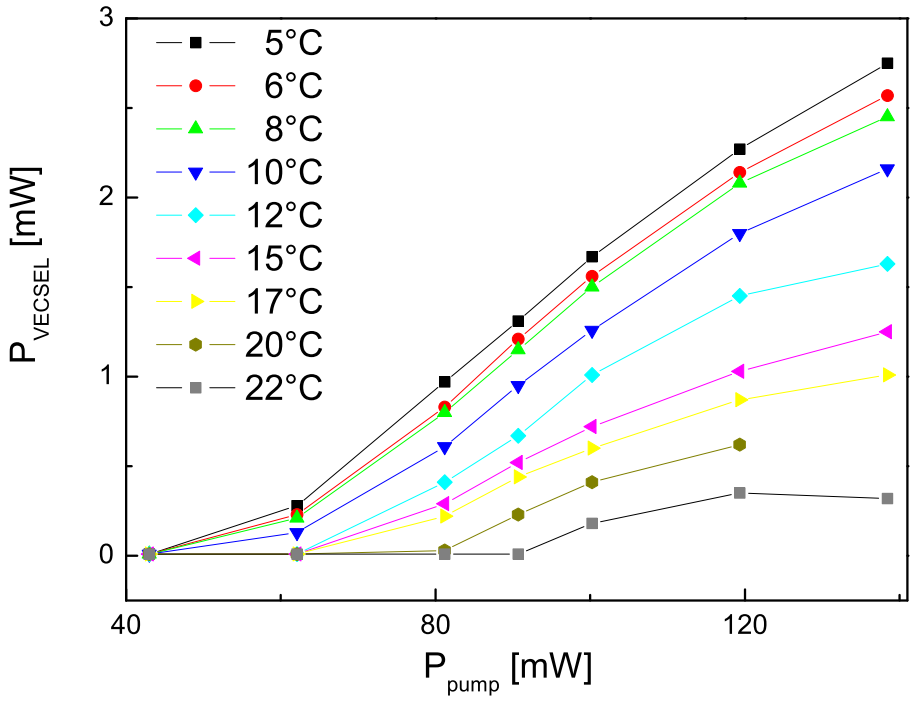

Figure 3.8: Power curves for different laser chip temperatures at 2.3 μm.

order to determine the length of the laser cavity, we examined the position of mode hops occurring over a cavity-length scan at constant temperature. Since in these conditions the gain curve does not move, mode hops occur when two longitudinal laser cavity modes are symmetrically placed with respect to the maximum of the gain-minus-losses curve, when they are in direct competition. As a result, mode hops are separated by one FSR of the laser cavity. It is to be noted that this simple behaviour is not observed in the absence of a wedge in the gain medium substrate, in which case cavity loss modulation induced by substrate étaloning result in a complex mode-hop pattern with non uniform and smaller mode-hop separations. Finally, we obtained FSR=3.6 cm^{-1} which corresponded to a resonator length of 1.39±0.08 mm. From a linear fit of frequency dependence on PZT voltage we determined a tuning rate of about 30 GHz/V.

Similarly the same FSR value could be retrieved from the temperature

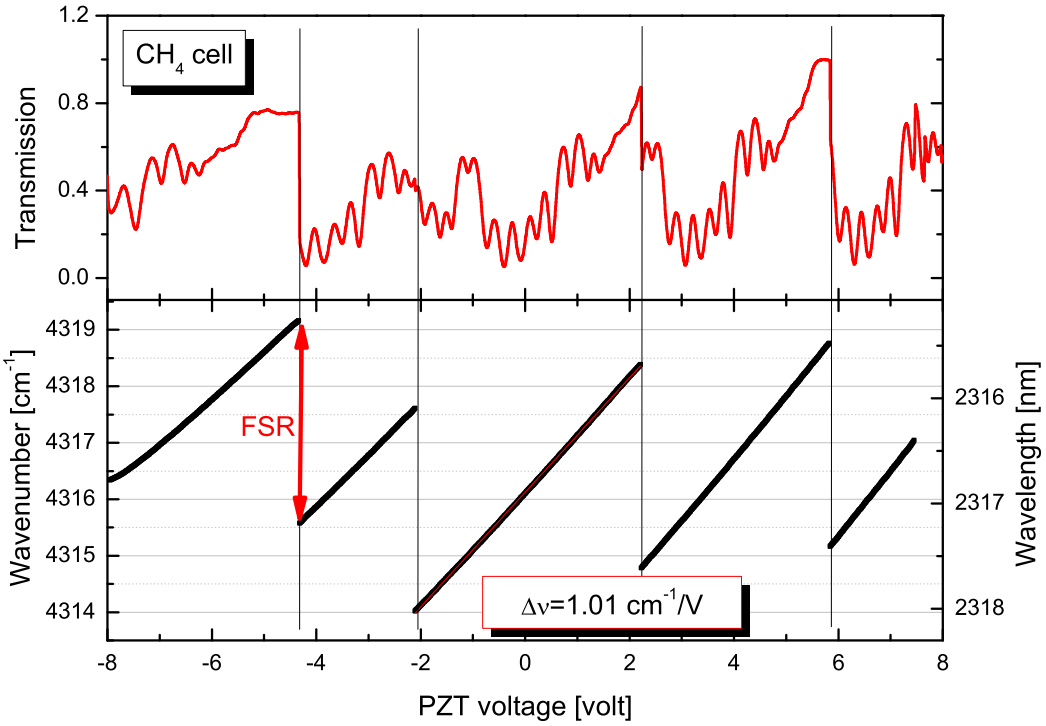

Figure 3.9: VECSEL frequency tuning by the cavity length scanning. We estimated the tuning rate from linear fit to by about $1\,\mathrm{cm}^{-1}/\mathrm{V}$ (30 GHz/V) and the VECSEL cavity FSR to be $3.6\,\mathrm{cm}^{-1}$ (108 GHz).

frequency tuning function (Fig. 3.10). In this case we observed also continuous tuning of about 11 GHz/K between mode-hops which resulted in reduced effective temperature frequency tuning of ∼-55 GHz/K. This effect could be attributed to the thermal effects on the 1/2-VECSEL support (expansion of the copper substrate holder and contraction of the peltier cooler).

To characterize more finely the VECSEL tuning behaviour, we determined the map of mode hops experimentally as a function of laser gain temperature and cavity length. We recorded étalon signal and methane cell transmission for a series of laser cavity length scans (PZT voltage from -10 to 10 V), each at constant temperature (in steps of 0.25 °C from 6 to 20 °C). For each scan, the methane absorption and the étalon signal traces were analysed to give a pattern of mode hops. When plotting all resulting patterns next to each other on a two-dimensional map (Fig. 3.11), it is easy to recognize the almost linear

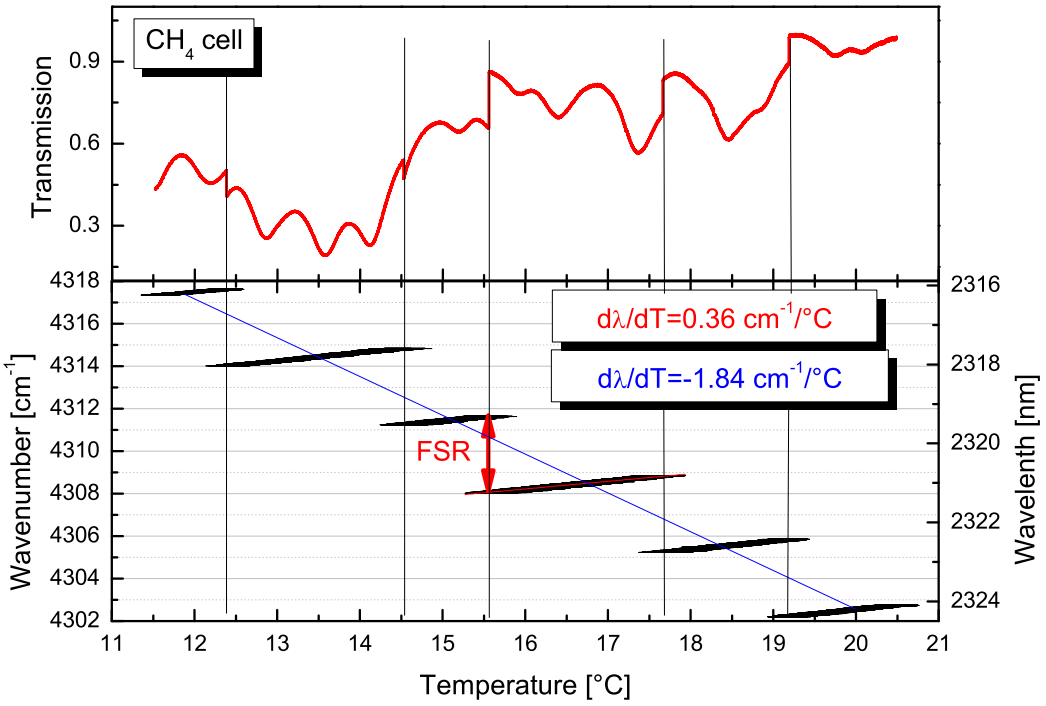

Figure 3.10: VECSEL frequency tuning by 1/2-VCSEL temperature variations. The effective tuning rate was estimated to be only -1.84 cm^{-1}/K (∼-55 GHz/K) due to the additional presence of thermal dilatation effect of 0.36 cm^{-1}/K (∼11 GHz/K).

behaviour of mode hops with both parameters. Some defects in the map are caused by imperfect mode-hop recognition.

On this map, it is possible to choose slightly curved diagonal paths which correspond to mode-hop-free scans. One such optimized tuning path is shown by the curved diagonal line in figure 3.11. We applied this synchronous curved ramp of both parameters and obtained a mode–hop–free continuous tuning. The speed of scan was relatively low (scan lasted about 2 min.) in order to allow the 1/2-VCSEL follow the temperature scan. The resulting methane absorption spectrum is shown in figure 3.12. This spectrum matched almost perfectly with a HITRAN simulated absorption spectrum. The scan range was about 500 GHz (16.5 cm^{-1}).

In the second part of prototype characterisation we tried to couple this

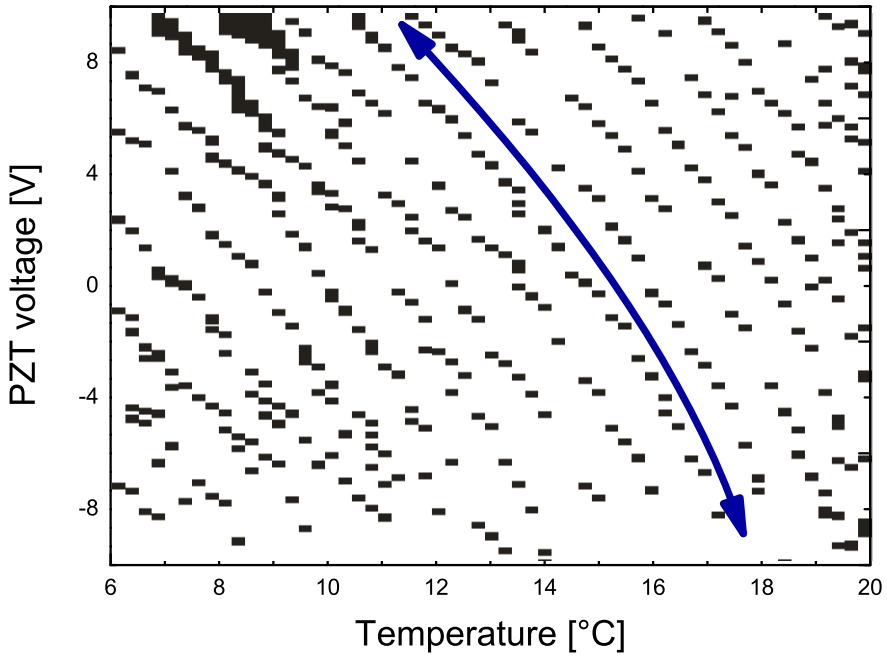

Figure 3.11: Mode–hop distribution acquired by PZT–voltage scans (from 6 °C to 20 °C). An optimal mode–hop–free tuning path is shown as a continuous curved line.

VECSEL with V–shape cavity according to the OF-CEAS scheme discussed in the introduction. The cavity was placed in place of the CH_4 cell. Two mirrors and a lens of 500 mm focal distance were used to match the TEM_{00} mode of V–shape cavity. The cavity mirrors were of moderate reflectivity (99.1%) and curvature of 500 mm. The length of the cavity arm was 38 cm corresponding to a FSR of 197.36 MHz.

Figure 3.13 shows an example of transmission signal from the cavity and étalon for a VECSEL operating at 10 °C with about 2 mW output. We can observe almost chaotic behaviour of the output signal when the laser enters in resonance with the cavity (Fig. 3.13-B). The étalon signal reveals (Fig. 3.13-A) that the optical feedback induces mode–hopping between two longitudinal modes of laser cavity. This effect could be explained by the variation of the VECSEL gain curve by the optical feedback. Due to resonant optical feedback

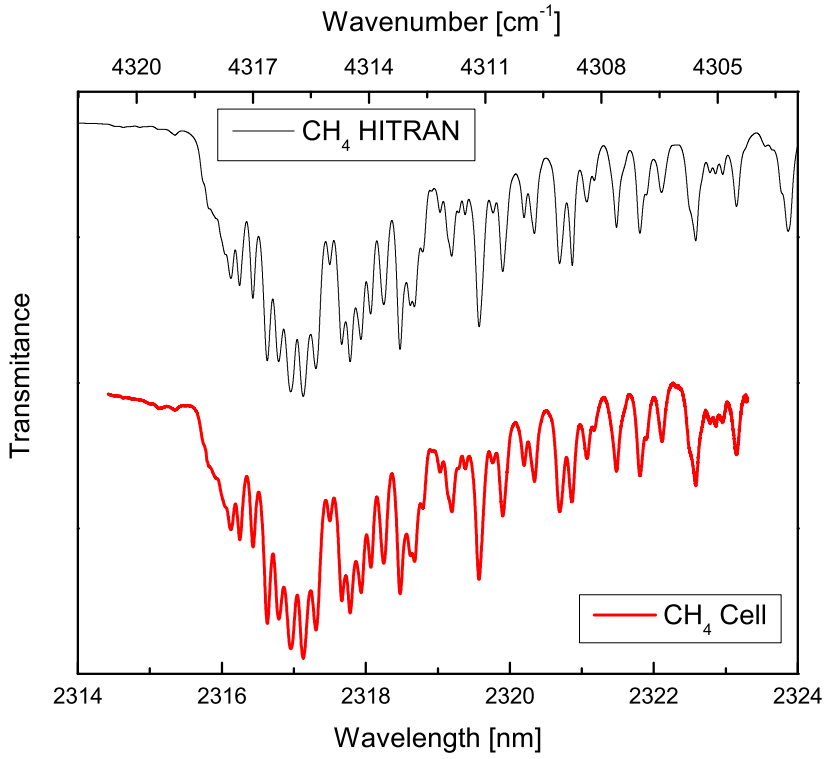

Figure 3.12: CH_4 direct absorption spectrum (5 cm, 1 Bar) obtained from the tuning path marked in figure 3.11. The HITRAN spectrum simulated for the same conditions is also plotted.

presence in the laser cavity the temperature of the active layer is modified, thus moving the gain frequency maximum. Consequently if maximum shift is large enough it could affect the mode beating in favour of different mode than lasing one and produce a mode–hop.

Shorter cavity VECSEL

The achieved mode–hop–free tuning range of 500 GHz with the 1.4 mm long cavity VECSEL offered significant improvement compared to the previous prototypes of VECSELs or DFBs [25]. Nevertheless the tuning was limited by the necessary complex control (synchronisation of piezo voltage and active layer temperature) and not completely predictable mode–hop positions. As a consequence the tuning was slow and not perfectly reproducible. Moreover the

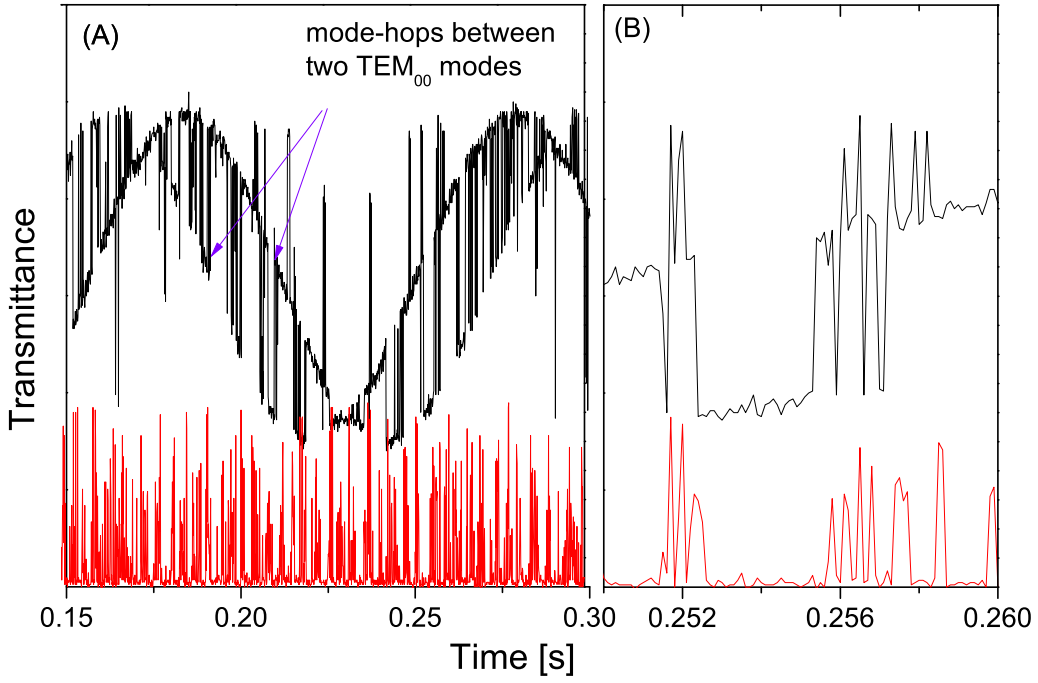

Figure 3.13: Transmission signal from the étalon (black) and V-shape cavity (red) obtained when injecting the VECSEL radiation in the cavity modes with the use of OF. The mode–hopping between two longitudinal modes is visible on the wide scale-(A). (B)-shows a detail of the signals confirming that the laser mode hops each time the cavity is injected and resonant OF comes back to the laser.

chaotic response of the laser to resonant OF from a V shaped cavity made the laser not useful for coupling with the OF-CEAS technique (CW-CRDS cavity injection could have been used, but it requires use of a fast optical switch and more control electronics). A possible way to addressing both these issues was shortening the VECSEL external cavity. With a shorter cavity the FSR is increased which allows broader mode–hop–free frequency tuning by cavity length only (according to eq.3.2). Secondly, the wider frequency separation of laser modes makes the laser less prone to mode–hops induced by gain displacement in the presence of resonant OF. Furthermore the reduction of laser dimensions (closer to telecom diode laser packaging) is favourable for developing a portable

spectroscopic instrument.

On the other hand according to the the modified S.T. theory (Eq. 3.1) limited by quantum noise the linewidth of the emission is inversely dependant on the square of cavity length. Therefore a reduction of the cavity length would cause the increase laser linewidth. For example for L=0.3 mm cavity the linewidth would be around 3 kHz which is still well below value to the DFB-MQW laser diodes used in OF-CEAS schemes [37, 72].

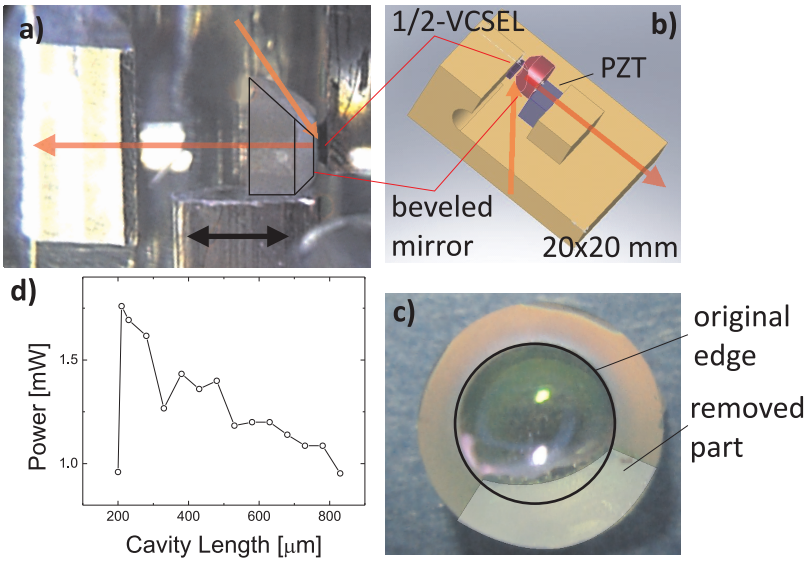

Figure 3.14: Prototype unit for VECSEL design testing: a-photograph of real setup, b-3D model of the prototype, c-treated external mirror (99.2 $\pm$ 0.25% reflectivity, 2 mm radius of curvature by BFI Optilas MI-2300-4-1.9-UV-2.089); d-output intensity as function of cavity length demonstrating minimal cavity length

For this prototype we used a small piece (2×2 mm) of the same 1/2-VCSEL structure as for the previously described 1.4 mm VECSEL. The pump scheme remained the same. To be able to assembly a short cavity VECSEL we beveled the edge of our mirror in order not to block the pump beam (Fig.3.14-c). With such mirror laser with cavity as short as 200 μm could be realized (Fig.3.14-a,b). This limit distance was determined from the decrease of the VECSEL output power when the mirror (mounted on a translation system for positioning) started to block the pump beam (Fig.3.14-d).

Later on for the frequency tuning and HFC injection measurements the mirror was fixed on a miniature $3 \times 3 \times 2\,\mathrm{mm}$ (Fig. 3.14-b) multilayer piezo stack actuator (PZT, by Physik Instrumente PL033.30). The mirror holder and the 1/2-VCSEL were mounted on a small metal base-plate ($20 \times 20\,\mathrm{mm}$) glued on a peltier for fine thermal control by a PID regulation circuit. The whole setup was placed in a sealed box flushed with dry nitrogen.

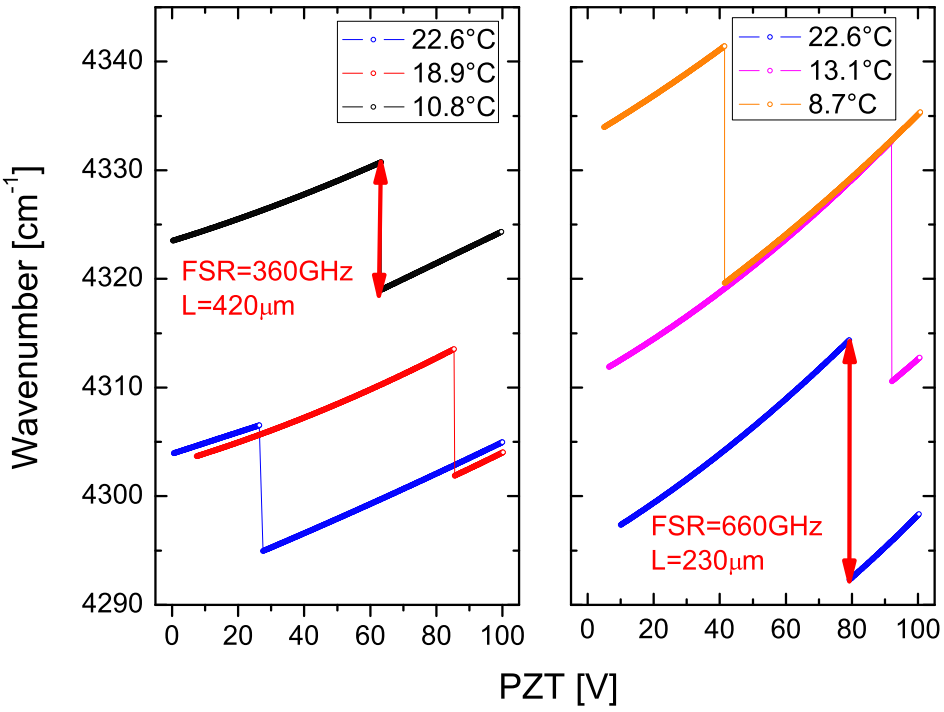

Figure 3.15: VECSEL frequency tuning by the cavity length scanning for different temperatures (from 9 to 22 °C) and cavity lengths of 420 and 230 μm.

On figure 3.15 we show the frequency tuning by cavity length scanning for two VECSEL cavity lengths (as determined from the mode–hop frequencies). Scans were made for different gain medium temperatures to demonstrate the total operation frequency potentially accessible with the slow synchronized temperature and cavity tuning. Maximal mode–hop free tuning range corresponded to the FSR value for a given length (360 GHz for L=420 μm and 660 GHz for L=230 μm) with repetition rate limited by the mirror moving

piezo (about 1 kHz). This tuning exceeded the one obtained for 1.4 mm cavity VECSEL both in range and speed.

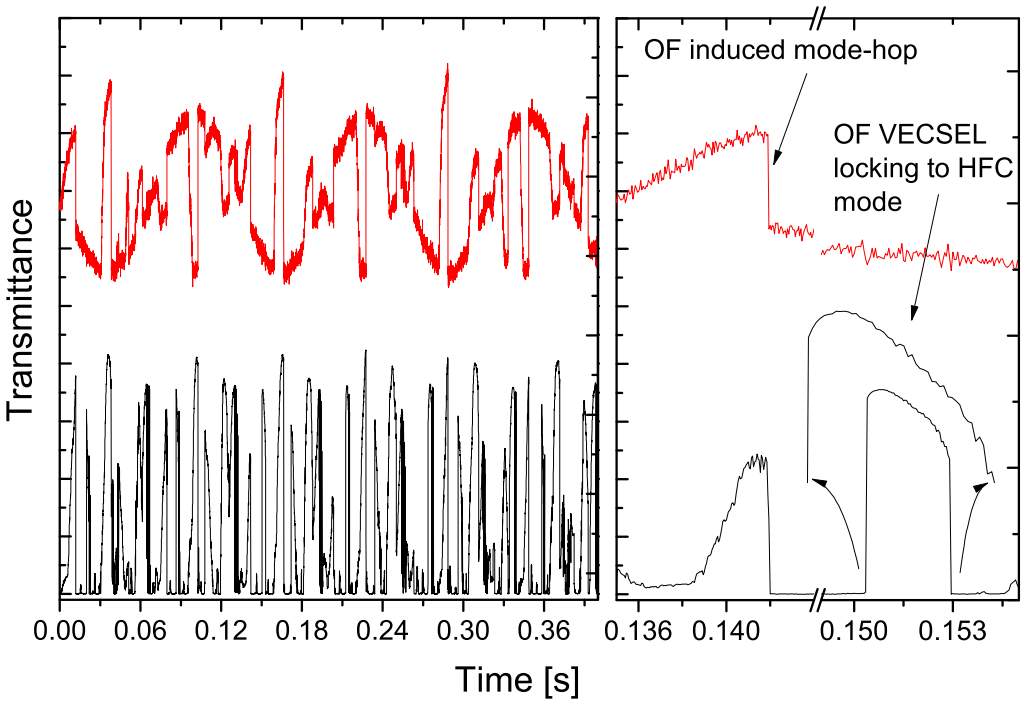

Figure 3.16: Transmission signal from the étalon (black) and V-shape cavity (red) obtained when injecting the ∼300 μm VECSEL radiation in the cavity modes with the use of OF.

With this setup we also performed measurements of the V-shape cavity transmittance with the presence of OF (Fig. 3.16). The optical coupling scheme and V-shape resonator were the same used in case of 1.4 mm VECSEL OF measurements. Compared to that case the transmittance signal was less chaotic but still with the presence of OF-induced mode–hops. On the other hand we could also observe sporadic laser locking without the mode–hops. From the analysis of the transmitted signal we deduced two principal remarks.

The resonant OF from the V-shape cavity was still strong for the VECSEL to handle and even when locking was achieved the cavity transmittance signal contained amplitude fluctuations (above the detector noise). This was in con-

trast with OF theory where the smooth shape is expected due to the significant spontaneous emission induced phase noise reduction by resonant OF.

Indeed in the ideal case the noise induced by spontaneously emitted photons with random phase is significantly suppressed by OF photons returning to laser with well defined phase (filtered by passage through HFC) identical to the phase of oscillating laser field. In practice however the optical length of laser cavity could be affected (e.g. by pump power noise or mechanical vibrations at times larger than 100 μs). As a consequence the phase of all photons oscillating in the laser cavity varies following these length fluctuations. So for longer integration times (over 100 μs) OF has very little effect on reducing this type of phase noise. To circumvent these problems we redesigned the setup to increase mechanical stiffness. To reduce the the amount of OF returning to laser we used a V-shape resonator composed from mirrors with higher reflectivity (R >0.999). Indeed according to equation 1.61 the transmittance of ideal V-shape cavity with no losses is proportional to 1/2(R+1).

300μm cavity VECSEL

Figure 3.17 shows both the design of the VECSEL prototype and the experimental setup used to characterize its optical properties. With respect to previous prototype the mirror holder and the 1/2-VCSEL were mounted on in a small metal cube with clearings for the beams and assembling tools. The miniature piezo was replaced with the piezoelectric tubular translator (by Physik Instrumente P-007.00) to provide low noise cavity length tuning. We also replaced the pump diode for a commercial 980 nm single transverse mode laser with higher pumping power (up to 400 mW). Unfortunately we did not observe the effect on output power due to the smaller active layer barrier absorption at this wavelength.

Laser output power ranged from 0.7 to 1.5 mW depending on the pump power (up to 300 mW) and lasing medium temperature. Scanning the VECSEL cavity length by the PZT voltage from 0 to about 400 V resulted in a frequency scan close to 1 FSR (about 550 GHz). The temperature of the las-

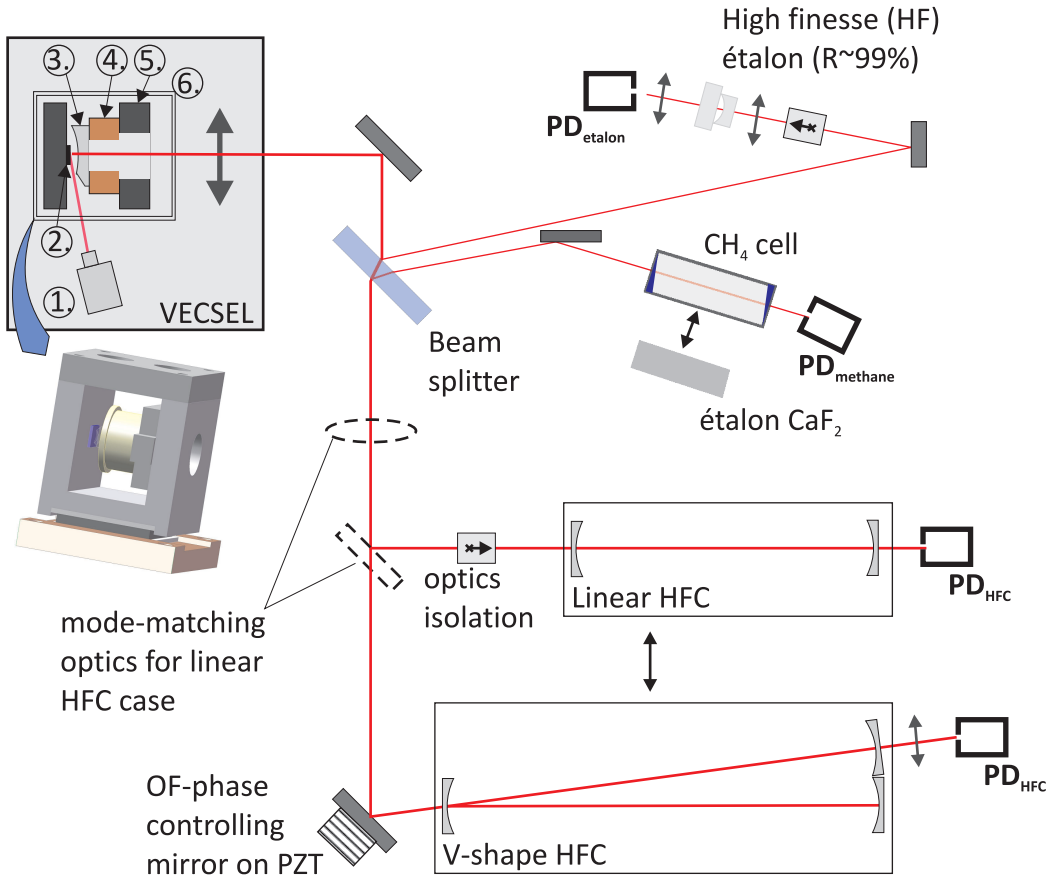

Figure 3.17: Experimental setup (not to scale) with 3D model of VECSEL cavity. VECSEL (12×8 cm) parts: 1.Pump laser, 2. 1/2-VCSEL structure, 3.External mirror, 4.PZT, 5.Mirror holder, 6.Peltier. Scheme shows alternative setups for work with either with a V-shape HFC (using OF) or a linear HFC (no OF). The HF étalon is plan–concave cavity with high reflective mirrors (99.1%) and length about 2 mm.

ing medium could be modified either by changing the diode pump power (local heating) or by changing the temperature of the whole laser cavity. In the first case, the change of active layer temperature caused tuning of the gain (about -75 GHz/K [25]) but with negligible effect on the lasing mode frequency because of the minor change of external cavity length by thermal stress. In the second case, tuning of gain went together with that of the external cavity length (material thermal expansion). The distance between the 1/2-VCSEL structure holder and external mirror holder was about 1.5 cm corresponding to a temperature scanning rate of about -70 GHz/K (aluminium has a thermal

expansion coefficient $22 \times 10^{-6}\,\mathrm{K}^{-1}$). As this was close to the quantum well gain wavelength tuning a broad frequency operation range from $4340\,\mathrm{cm}^{-1}$ to $4290\,\mathrm{cm}^{-1}$ (for approximately 5 °C to 25 °C) became accessible.

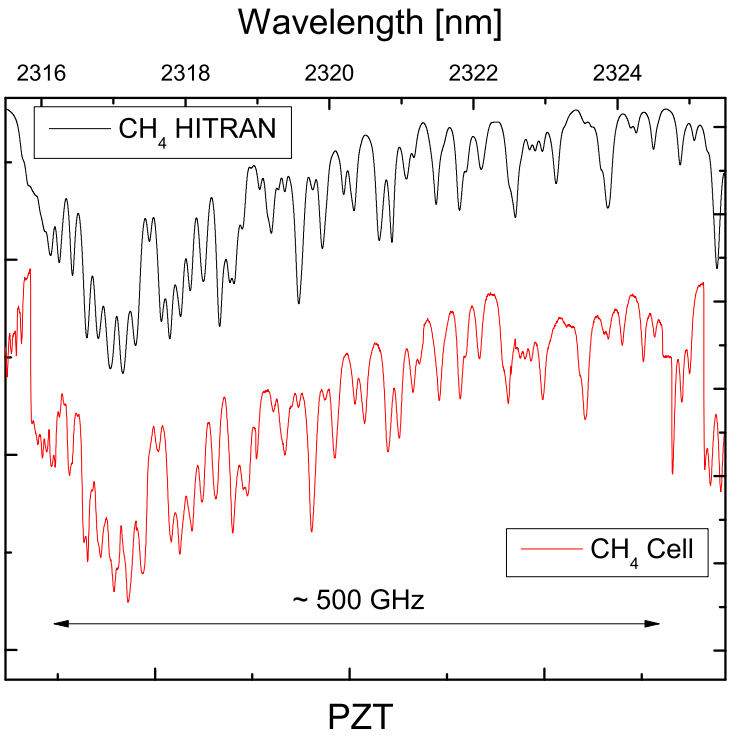

Figure 3.18: CH_4 direct absorption spectrum, obtained with cavity length scan (PZT voltage from 0 to 400V) of a ∼300 μm VECSEL resulted in close to 1 FSR long mode–hop free tuning. We obtained very similar spectra than for the 1.4 mm VECSEL (Fig. 3.12) but in much shorter time, 20 ms here compared to 2 s for the complex tuning of 1.4 mm VECSEL.

Laser frequency fluctuations were monitored using projection of frequency noise to amplitude variations by transmission on the slope side of an optically–isolated plano–concave étalon resonance. The full width at half maxima (FWHM) of étalon resonances was about 210 MHz leading to minimum observable frequency excursions around 500 kHz (limited by the detector noise). On the 10 ms integration time we observed frequency jitter bellow 3 MHz peak to peak (Fig. 3.19-A). From the corresponding frequency noise spectral density (Fig. 3.19-B) we calculated the RMS laser noise to be around 1 MHz (for 10 ms

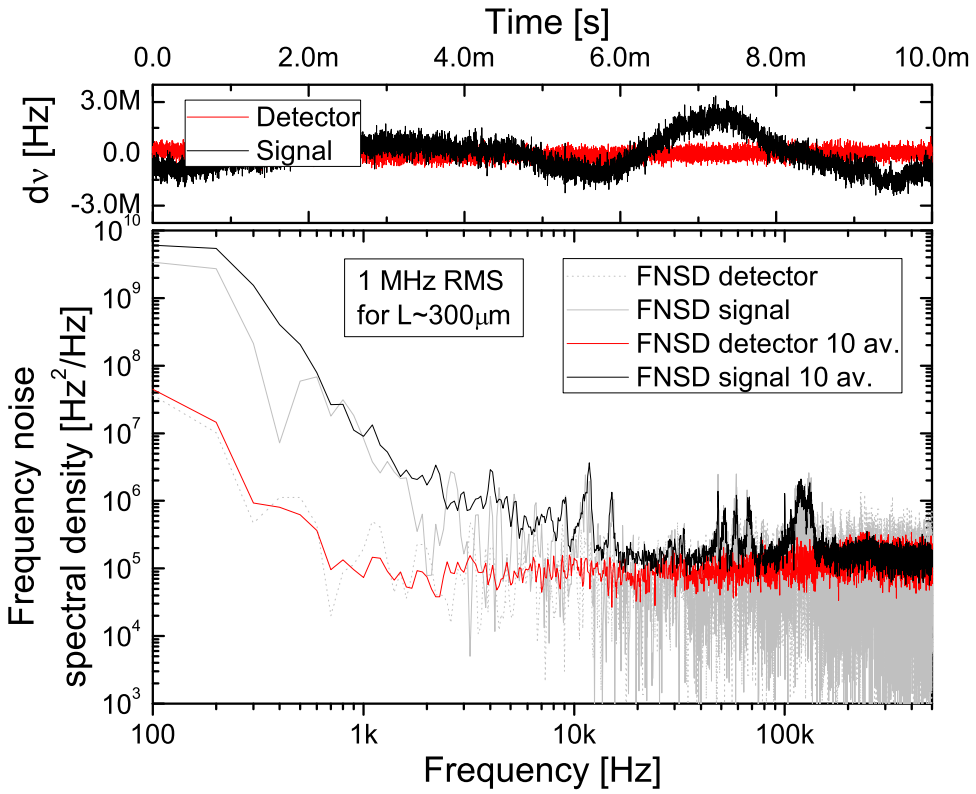

Figure 3.19: Laser frequency fluctuations as measured by the Fabry-Perot étalon on the slope of the resonance – Signal. The detector signal represents zero signal from photodiode. On the bottom corresponding frequency noise spectral densities for single scans and for the average of 10 measurements. On the 10 ms integration time we measured a RMS laser frequency noise about 1 MHz.

integration time). Also we found that the contribution of the technical frequency noise ends around 10 kHz. This shows that to suppress this noise in CEAS measurements the interaction time between HFC and VECSEL should be shorter than 100 μs.

Firstly we investigated the capability of laser injection into a HFC without OF. A linear cavity of 60 cm length was composed from two low loss mirrors (Layertec, R_c=1 m and R=99.97%). Mode matching was achieved by two mirrors and a focussing lens. To block OF from the HFC we used an optical isolator. Figure 3.20 shows transmission of HFC for one mode scan at different tuning speeds (from 75 to 700 GHz/s). To be able to recognize the fine features of HFC transmission we used the 20 MHz A/D card (with 12 bit resolution)

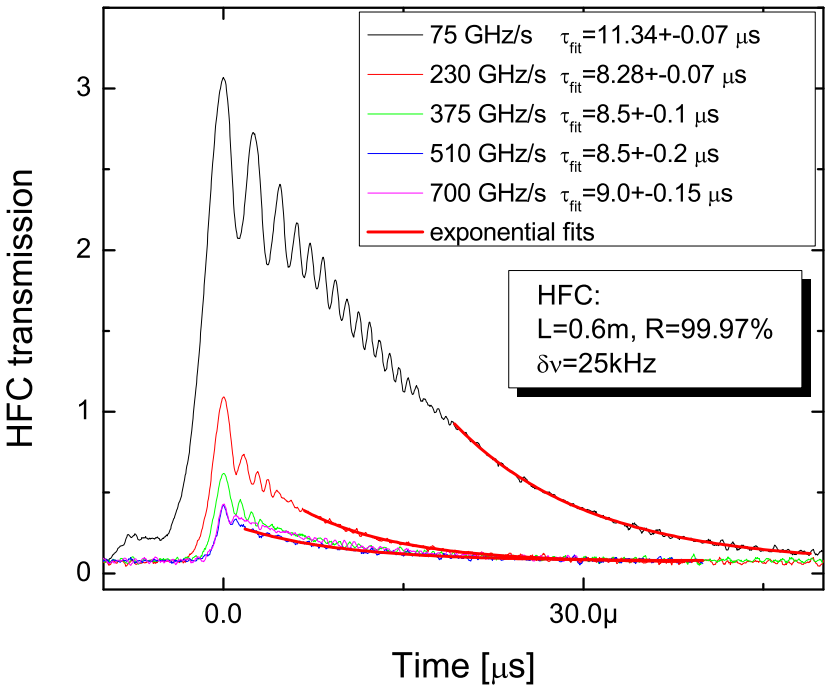

Figure 3.20: Transmission signal from the linear HFC cavity for different tuning rates.

for signal digitalisation.

For all tuning rates we observed well–resolved ringing structure in a close agreement with the theory of monochromatic source injection to HFC presented in the introduction. Indeed comparing the interaction time between laser and HF (from 300 μs to 30 μs for given tuning rates and 25 kHz width of the HFC mode resonance) and the frequency characteristic of laser noise (Fig. 3.19-B) we see that for all cases the corresponding frequency of interaction is above the major low frequency noise component (ends around 5 kHz). This means that for a very short integration times the laser linewidth is close to the theoretical value ($\sim$3 kHz) according to modified S.T. theory (eq. 3.2). Also for tuning rates over 500 GHz the ringing almost disappeared and only the exponential decay form remained. In such conditions the straightforward intra–cavity absorption retrieval by ring–down fit is possible [16]. The intra–

cavity absorption could be calculated also from the slower rate data where the amplitude is much higher. However, this could be done only by the cavity transmission modelling as described in the introduction. Indeed the exponential fitting of smooth (without ringing) part of transmission decays (Fig. 3.20) showed discrepancy between the ring–down times obtained for the slow tuning (about 11 μs for 75 GHz/s tuning speed) and the fastest tuning (about 9 μs for 700 GHz/s tuning speed) which is according to theory [16] closest to the real cavity ring-down.

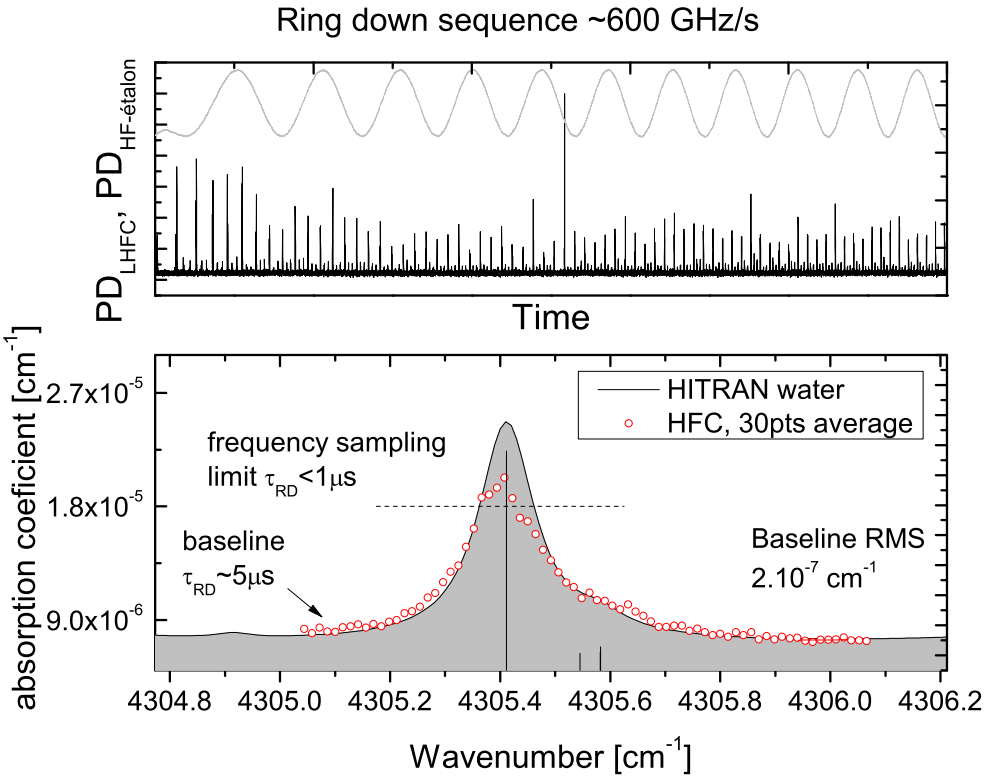

Figure 3.21: CRDS absorption spectra of atmosphere obtained by fast (600 GHz/s) VECSEL scanning through several HFC resonances. Plotted spectra represents average of 30 scans obtained in 1.5 s. The achieved sensitivity was 2×10^{-7} cm^{-1} measured as RMS of baseline linear fit. The dynamics of absorption measurements was limited by long signal sampling and poor injection efficiency at used tuning speed.

To demonstrate this capability we performed a small spectral scan(1 cm^{-1}) at rate 600 GHz/s (Fig. 3.21). The VECSEL was rapidly tuned across several

HFC resonances without any interruption to obtain smooth decay signals. We recorded 30 scans to create the spectrum (in total time about 1.5 s). For the faster data treatment with higher precision we used only 600 kHz signal sampling but with 16 bit amplitude resolution. The detection sensitivity of about $2\times10^{-7}\,\mathrm{cm}^{-1}$ was evaluated as the RMS of baseline linear fit. Rather large noise value was caused both by the relatively low cavity quality (baseline ring-down was only around 5 μs) and acquisition frequency sampling (problems with under sampling in case of short ring-downs in the higher absorptions). Also due to the fast passage through resonance the amplitude of transmitted signal was limited.

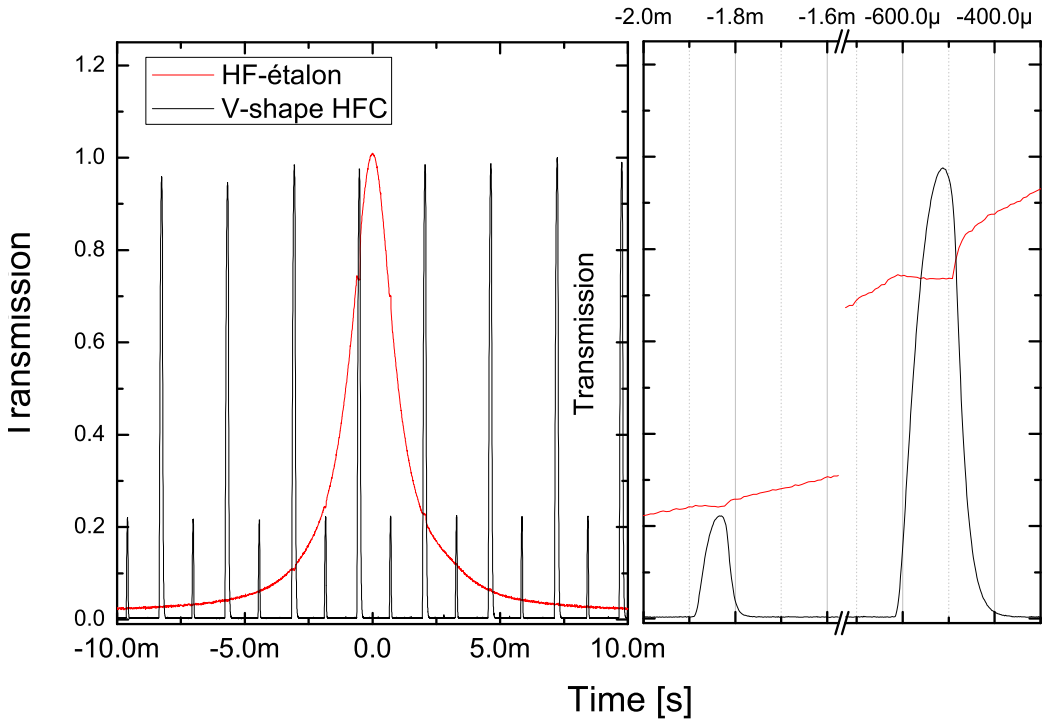

Figure 3.22: Transmission of HFC and HF étalon confirming good behaviour of the laser in the presence of OF.

In a second time we were interested in the short VECSEL behaviour in the presence of OF. For this experience we used the scheme with V-shape cavity proposed by Morville et al. [55] and exploited in OF–CEAS [72]. The

HFC cavity (Fig. 3.17) was a pre-aligned V-shape resonator with 50 cm arms and mirrors of 99.99 % reflectivity. The fine control of HFC laser distance was handled by the second mode–matching mirror mounted on a piezoelectric transducer.

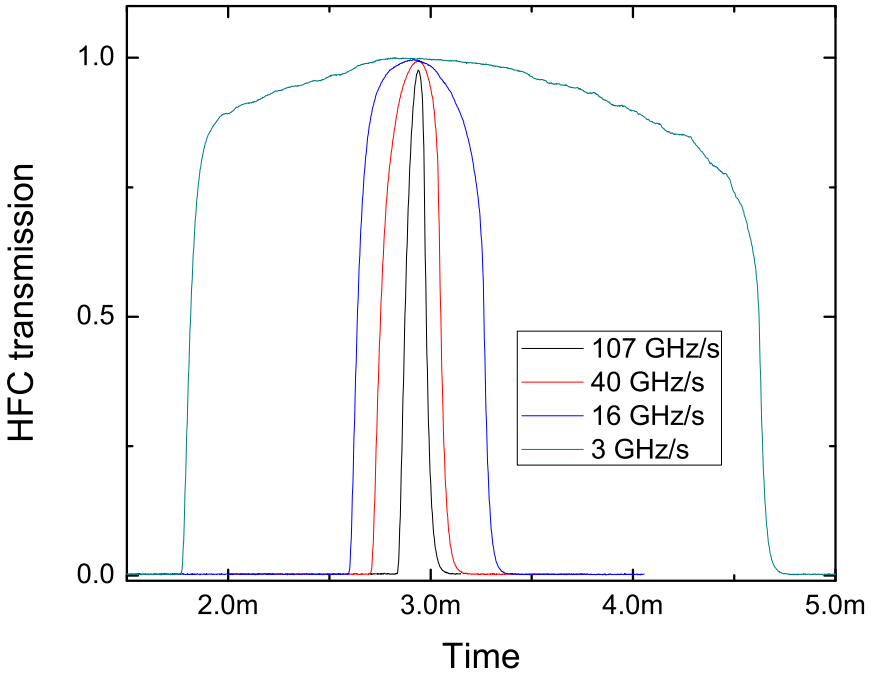

Figure 3.23: The effect of tuning speed on the HFC transmission.

The transmission signals for V-shape HFC and the frequency monitoring étalon are shown in figure 3.22. In this case we observed unperturbed transmission peaks corresponding to HFC resonances as predicted by the theory describing OF-laser interaction. Due to their relatively high laser cavity finesse, VECSELs are more likely to suffer by insufficient OF compared to other lasers which have been applied to OF-CEAS: Distributed feed–back [55] and extended-cavity [15] diode lasers. Unusually large even-odd difference (Fig.3.22) in the ring–down time and in the transmitted intensity for the present case is indication of a large inhomogeneity or the presence of a defect on the folding mirror of the V-cavity. As a consequence in the present

case the observed locking range was about 10 times smaller than the HFC FSR even after optimising the laser–cavity coupling, notably by transverse mode matching (Fig. 3.22).

The maximum exploitable frequency tuning speed (Fig.3.22) was then about 120 GHz/s corresponding to a time of passage through resonance (broadened by the OF locking) of about 20 μs, which was comparable with the cavity ring–down time. Above this rate the interaction time between laser and HFC was too short to achieve adiabatic behaviour of this process. At low tuning rates the limit was determined by the mechanical/thermal laser noise. We observed smooth transmission for rates down to 16 GHz/s. This corresponded to time of interaction in order of 100 μs which was in agreement with the measured frequency noise characteristic (Fig.3.19-B).

3.4 Optimization of a OF-CEAS spectrometer

The 300 μm VECSEL showed stable and predictable behaviour in the interaction with the OF from HFC. Together with very good spectral properties this makes it a very good candidate for spectroscopic applications. In this section we describe the optimization of a spectrometer (Fig. 3.24) based on the coupling of the short cavity VECSEL to a V-shaped HFC (the same as described in previous section) according to the optical feedback cavity enhanced spectroscopy (OF-CEAS) scheme developed by Morville et al. [55].

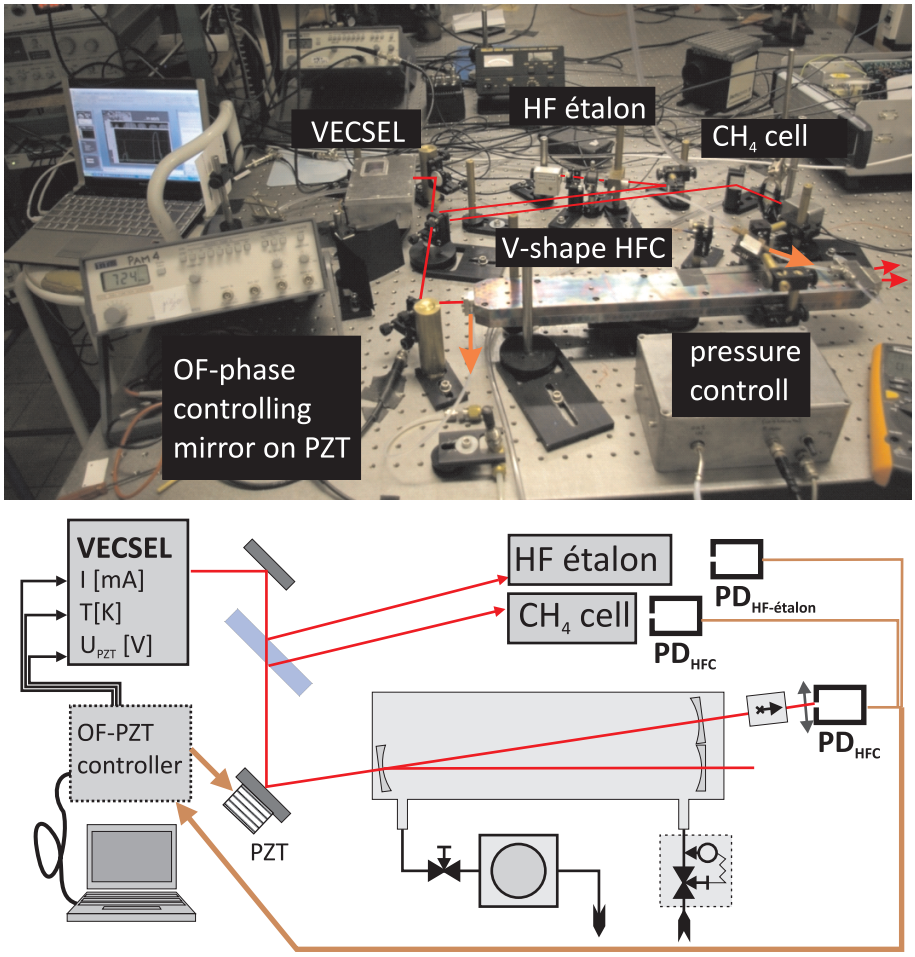

Figure 3.24: Scheme and photograph of VECSEL based OF-CEAS spectrometer.

3.4.1 OF–CEAS operation

In OF–CEAS setup [72] when laser scans through the HFC resonance the HFC output mode profile appear with a smooth rounded shape (see Fig.3.25) whose maximum corresponds, according to the theory, to the transmission which would be obtained at the resonance center with a perfectly monochromatic source. Low noise mode-by-mode CEAS spectra are then obtained with data points uniformly spaced by exactly the FSR of the HFC. To achieve suitable OF as defined in [55] a piezo–mounted mirror is used to control the OF phase by acting on the laser–cavity distance. This signal is generated automatically by an analogic electronic card analysing the HFC transmittance signal symmetry [72].

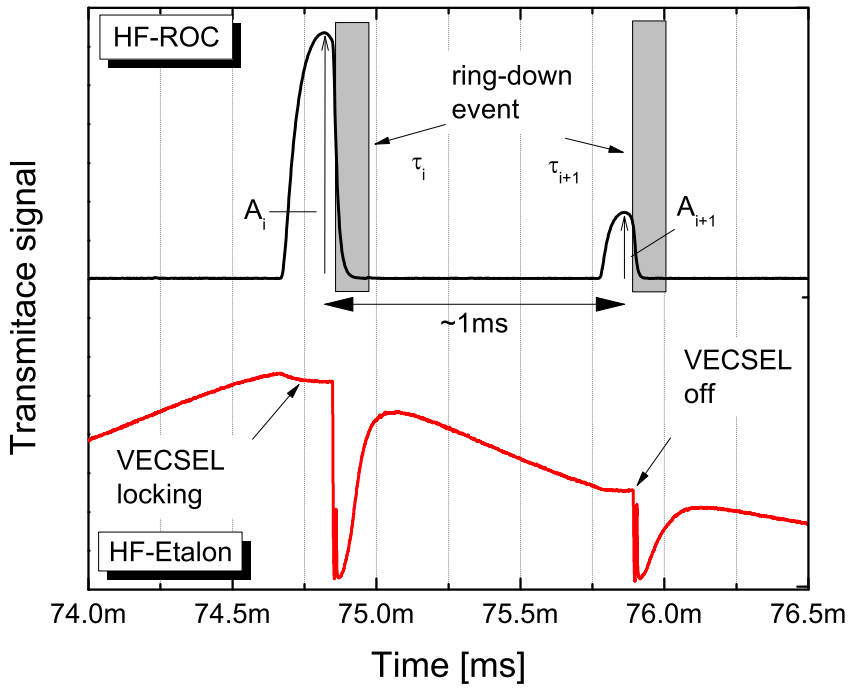

Figure 3.25: HFC and Frequency monitoring étalon signals.

In order to acquire absorption spectra, we implemented an approach similar to the combined mode-by-mode OF-CEAS + CRDS scheme by Motto–Ros et

al. [59]. The maximum of mode transmittance H_i^{max} for the i-th mode is to a very good approximation inversely proportional to the square of total HFC optical losses per pass γ_i which may also be derived from a measurement of the ring-down time τ_i [38, 58]:

$$\sqrt{H_i} \simeq \xi\, L/\gamma_i = \xi\, c\, \tau_i \tag{3.3}$$

where ξ is a constant, c the speed of light and L the cavity length. Notice that $L/\gamma_i = c\,\tau_i$ is the HFC internal loss per unit length, the correct unit for absorption spectra. For practical reasons we did not use a photodiode sampling the laser power incident on the HFC. However, in Eq.3.3 we may use the transmitted intensity T_i^{max} as an approximation for H_i^{max} and consider that $\xi\, L$ is now a slowly frequency dependent function ($\xi\, L \rightarrow \xi_i^{norm}$) due to the small changes in VECSEL power during PZT tuning (about 2% for the 20V scan applied, as explained below). To obtain best determination of normalisation function ξ_i^{norm} a low order polynomial fit of $\gamma_i\sqrt{T_i}$ was used (Fig. 3.26). Subsequently the OF-CEAS spectrum (in absolute units of absorption per unit length) was obtained simply as $\xi_i^{norm}/\sqrt{T_i}$. While we could have used the ring–down values in order to directly obtain the absorption spectrum, this procedure exploits fully the significantly higher S/N of the transmission maxima under OF locking conditions.

Finally in order to obtain abundances a_k (k stands for a molecule) of species using the absorption lines present in the spectra, a multi–parametric nonlinear fit was used. The algorithm was based on the Levemberg–Marquard method with fitting function

$$F(i) = \left\{ \sum_{\forall k} HITRAN_{p,T,k}(X(i)) \cdot a_k \right\} + B(i) + M(i)\ .$$

Where $HITRAN_{p,T,k}$ is the simulated absorption spectrum of molecule k at pressure p and temperature T for frequency given by x-scaling linear polynomial $X(i)$, $B(i)$ is the baseline and $M(i)$ is a polynomial correcting even–odd mode difference. Free parameters were: the abundances a_k and coefficients of

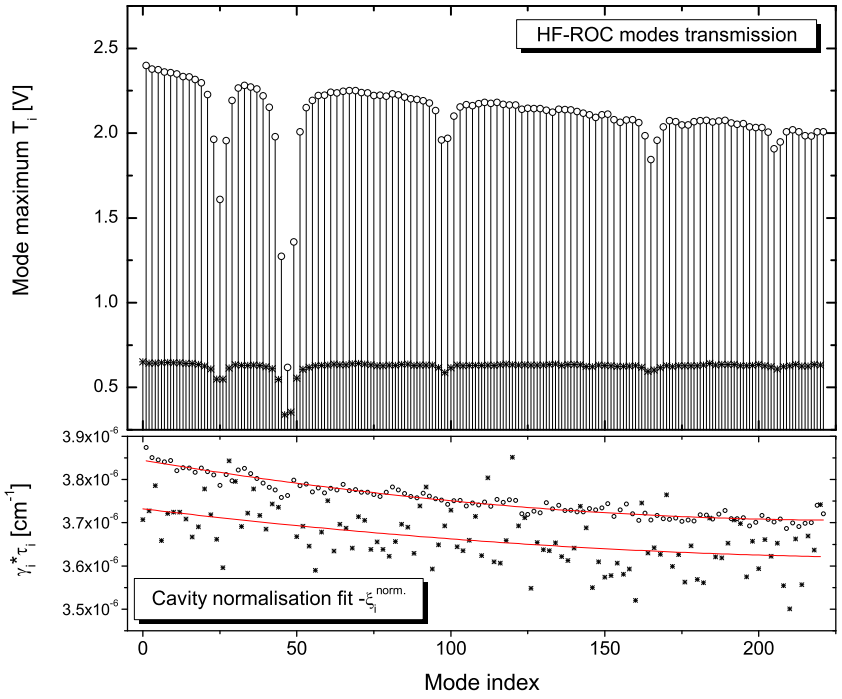

Figure 3.26: Cavity transmittance normalisation $\xi_i^{norm} = \gamma_i\sqrt{T_i}$.

polynomials $X(i)$, $BL(i)$ and $M(i)$.

3.4.2 Results

The spectrometer operated around 4315 cm^{-1}. As a sample we used dry nitrogen mixed with ambient air at a pressure of 100 mbar. Initially, we tuned the VECSEL frequency by a ramp applied through a high voltage amplifier to the external cavity PZT. The high voltage resulted too noisy, with a clear correlation of amplitude fluctuations in the HFC transmission signal with voltage fluctuations. For this reason we applied directly to the PZT a low voltage ramp (0-20 V) possessing a much lower noise level. This covers only 5% of the maximal mode–hop free range of 550 GHz given by the FSR of the VECSEL cavity. The tuning speed was set to 115 GHz/s.

In first step we evaluated the level of baseline noise (measured as RMS of baseline linear fit) and its dependence on number of averaged scans by

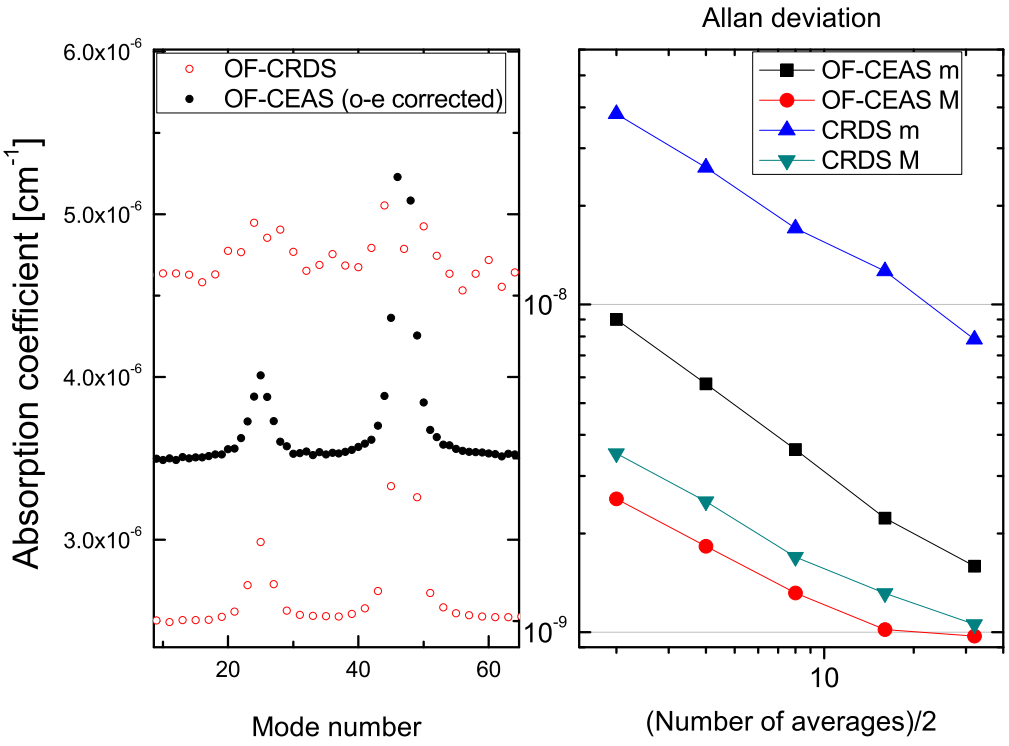

Figure 3.27: Comparison of the absorption spectra obtained directly from the ring–down times (OF-CRDS) and using the OF-CEAS approach based on eq.3.3. The OF-CEAS data are plotted with corrected odd–even modes difference. On right the measured Allan deviation plot (root of Allan variance) shows the averaging effect separately for even and odd modes and for OF-CRDS and OF-CEAS case.

using the Allan variance method (Fig. 3.27). For a single scan (comprised around 200 cavity modes) the baseline noise was about $2.5 \times 10^{-8}\mathrm{cm}^{-1}$ or $9 \times 10^{-10}\,\mathrm{cm}^{-1}Hz^{-1/2}$ given the 760 Hz acquisition rate of cavity modes. Averaging was able to reduce the baseline noise up to about 100 scans, to the value $2.5 \times 10^{-9}\mathrm{cm}^{-1}$.

In order to obtain a larger continuous scan a slow temperature ramp was applied simultaneously to PZT scans. The laser assembly temperature was varied about 2 °C in 2.5 minutes resulting in a frequency coverage from 4311.2 to 4318.5 cm^{-1}. During the scan approximately 500 PZT scans were performed passing over each mode about 80 times. To obtain the complete spectrum (Fig. 3.28) we firstly retrieved absorption coefficients from each scan and

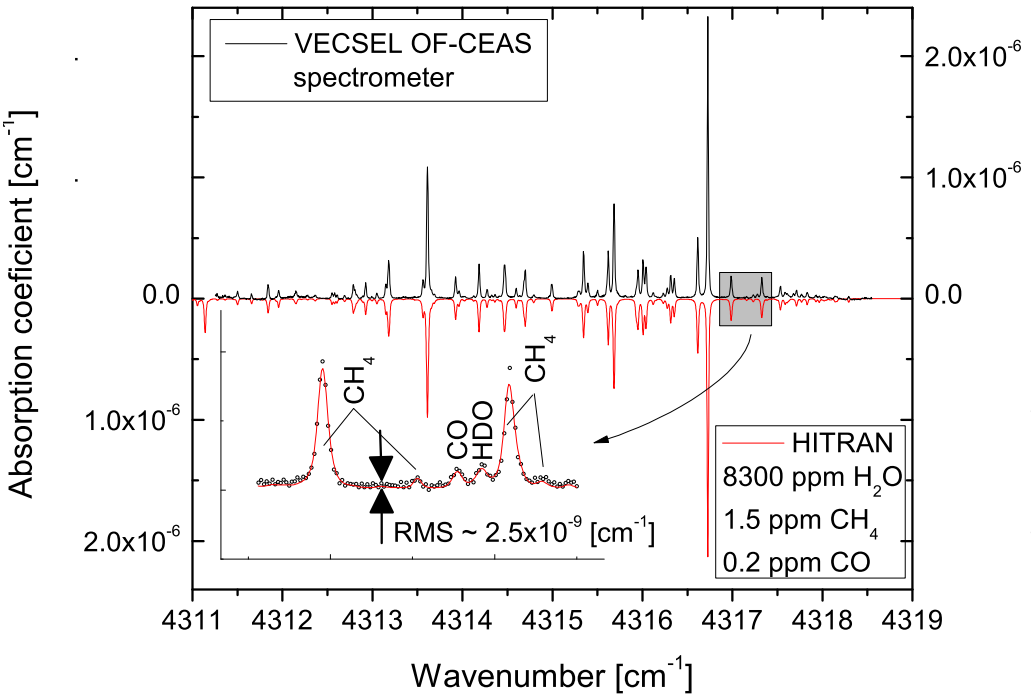

Figure 3.28: Absorption spectrum of N_2–diluted air (100mbar) acquired by simultaneous temperature and PZT VECSEL frequency tuning over 2.5 min. The zoomed detail permits to appreciate the level of baseline noise.

then averaged corresponding values for each mode. The exact frequency given by linear function of mode index ($= i * FSR + X_0$), as well as molecular abundances, were determined from HITRAN [76] simulation. We determined the concentrations 8300 ± 40 ppm for H_2O, 1.5 ± 0.01 ppm for CH_4 and 0.2 ± 0.1 ppm for CO. We were able to recognize even weak HDO peaks (during the fit we used natural isotopic ratio), one example is shown in the zoomed detail on Fig. 3.28.

3.5 Conclusion

In conclusion a short–cavity VECSEL is capable to operate single–frequency and low–noise in the presence of resonant OF from a HFC. We demonstrated that for spectroscopic applications the short cavity (0.2 mm-0.3 mm) has numerous advantages over long (e.g. 1.4 mm) cavity VECSELs. The easier and more stable frequency tuning together with smaller dimensions of device came at cost of wider linewidth but still lower to DFB sources. Reduced length helped also eliminated the mode-hopping in the presence of the OF allowing us efficient coupling with HFCs. The presented OF-CEAS spectrometer achieved sensitivity comparable to that of other reported OF-CEAS systems based on DFB or ECDL and a frequency coverage of about $50\,\mathrm{cm}^{-1}$. This prove of capability of coupling VECSEL to HFCs by use of OF opens the possibilities of larger spectroscopic application.

Moreover, the limitations presented by our setup (finesse of the HFC, VECSEL frequency fluctuations) are clearly subject to improvement in order to produce portable and easy operation laser source. For example miniaturized opto–mechanical assemblies such as in telecommunication devices could be exploited to still improve mechanical stability and reducing size of VECSEL assembly. A low–noise high–voltage ramp generator would allow fast cavity scans over the full FSR of the VECSEL, about $20\,\mathrm{cm}^{-1}$ in our case and slower temperature synchronized scans over whole operation range (about $50\,\mathrm{cm}^{-1}$). Further shortening of laser resonator is also possible but would lead to increase of laser linewidth above 2 MHz (10 ms integration time, 300 μm long cavity) which would subsequently affect the HFC injection efficiency. Currently a new spectrometric system is being build including improved VECSEL to allow broad-band measurement in the 2.3μm region.

Conclusions et perspectives

Dans ce travail nous nous sommes concentrés sur le développement et l'application de plusieurs méthodes spectroscopiques de haute sensibilité dans l'étude de la physique des gaz et du plasma. La spectroscopie d'émission à large bande rapide (FBES) a été utilisée pour caractériser la décharge à barrière diélectrique. Nous avons également développé les algorithmes nécessaires au traitement spectral des données. L'observation de l'émission de trois transitions rovibrationnelle dans une décharge de gaz N2-O2 mélange N2-O2 a été utilisée pour caractériser les différents régimes de la décharge dans les deux configurations différentes. Nous avons réussi à produire et mesurer l'oxygène singulet dans une décharge micro-ondes. Nous avons réussi à mesurer 21 nouvelles transitions spectroscopiques que nous avons attribuées à des branches O, P, Q et R du système bb$^1\Sigma_g^+$(v=1)-a$^1\Delta_g$(v=0). La génération d'oxygène singulet dans le DBD n'a pas été confirmée. Pour obtenir des résultats dans ce domaine, des améliorations seront apportées à la fois sur le réacteur et sur le détecteur de CRDS à la fois pour augmenter la production de radicaux et la sensibilité de la détection par CRDS. Les schémas optiques ainsi que les logiciels pour le traitement des données (par exemple, l'étalonnage et le montage des spectres échelle) développées ont été également exploités avec succès dans différentes expériences dans le laboratoire (spectroscopie induite par laser, spectroscopie d'émission de différents types de décharges, etc.).

L'application d'IBB-CEAS couplé avec une source LED s'est présentée comme une méthode très prometteuse. Avec un schéma optique simple et robuste à faible coût, le paramètres attendu a été concurrentiel par rapport à des techniques de détection similaires (principalement la limite de détec-

tion de $5\times10^{-9}\,\mathrm{cm}^{-1}$). Le développement de cette technique se poursuit au LSP Grenoble afin d'assembler un détecteur transportable pour des mesures *in situ*. En ce qui concerne le développement du VECSEL, nous avons réussi à concevoir et assembler un prototype approprié à l'application spectroscopique. Sa capacité a été illustrée en le couplant à la HFC à la fois selon les schémas CRDS et OF-CEAS. La sensibilité atteinte ($9 \times 10^{-10}\,\mathrm{cm}^{-1}Hz^{-1/2}$) est comparable à la sensibilité d'autres systèmes OF-CEAS basés sur les DFB ou ECDL, mais avec une couverture spectral d'environ $50\,\mathrm{cm}^{-1}$ plus importante. Les perspectives d'avenir du système sont principalement dans la détection de traces atmosphériques simultanées de plusieurs éléments et dans le couplage avec une HFC linéaire afin de réaliser des mesures d'absorption ultra sensibles de dioxyde de carbone et de méthane, principalement pour les besoins planétologiques (atmosphère de Vénus et de Mars).

Conclusions and perspectives

In this work we were focused on the development and application of several high-sensitivity spectroscopic methods in the study of gas and plasma physics. The Fast broadband emission spectroscopy was used to characterize the dielectric barrier discharge. We also developed the algorithms necessary for spectral data treatment. The observation of the emission of three ro-vibrational transitions in N_2-O_2 gas mixture discharge was used to characterize different regimes of discharge in two different configurations. We were able to successfully generate and measure the singlet oxygen in a microwave discharge. We succeeded in measuring 21 new spectroscopic transitions that we assigned to the O, P, Q and R branches of the $b^1\Sigma_g^+$(v=1)-$a^1\Delta_g$(v=0) system. The generation of singlet oxygen in DBD was not confirmed. To obtain results in this area, further improvements will be made both on the reactor and the CRDS detector in order to both increase the production of radicals and the sensitivity of the CRDS setup. The developed optical schemes together with support software for data treatment (e.g. calibration and fitting of echelle spectra) were successfully exploited also in different experiments in the laboratory (laser induce spectroscopy, emission spectroscopy of various kinds of discharges, *etc.*).

The application of IBB-CEAS coupled with a LED source showed to be a very promising technology. With simple and robust optical layout at low-cost the achieved parameters were competitive compared to other common detection techniques (mainly the detection limit of $5\times10^{-9}\,\mathrm{cm}^{-1}$). The development of this technique continues at the LSP Grenoble in order to assembly transportable detector for *in situ* measurements. Regarding the development of the VECSEL, we succeeded in designing and assembling prototype suitable for

spectroscopic applications. We demonstrated its capability by coupling it to HFC according to both the CRDS and OF–CEAS scheme. The achieved sensitivity ($9 \times 10^{-10}\,\mathrm{cm}^{-1}Hz^{-1/2}$) is comparable to sensitivity of other reported OF-CEAS systems based on DFB or ECDL but with higher frequency coverage of about $50\,\mathrm{cm}^{-1}$. The future prospects of the system are mainly in the use in simultaneous multi-element atmospheric trace detection and combination with linear HFC in order to perform ultra sensitive absorption measurements of carbon dioxide and methane mainly for planetology purposes (atmosphere of Venus and Mars).

Appendix

Simulation of HFC injection

The injection of a monochromatic coherent source with a linear frequency modulation into a linearly swept cavity is the closest case to the stationary solutions for FPR transmittance function presented in equation 1.26. The model is developed in the 1D approximation of TEM_{00} FPR mode excitation by the electromagnetic wave propagating in the direction of axe x. Situation is described on space–time plot on figure 1.19. The source of radiation is placed at the entrance mirror of the cavity. This mirror is considered fixed and only output mirror change its position in time. The temporal behaviour of radiation source frequency $\omega(t)$ and cavity length $L(t)$ is studied around a FPR resonance

$$L(t) = L_0 + v \cdot t \tag{3.4}$$

$$\omega(t) = \omega_0 + W \cdot t \tag{3.5}$$

where v and W are the cavity tuning speed in $\mathrm{m.s^{-1}}$ and angular frequency scanning speed in $\mathrm{rad.Hz.s^{-1}}$ respectively. The initial ($t = 0$) frequency ω_0 and cavity length L_0 obey the condition for FPR resonance from 1.38

$$\omega_0 = 2\pi \cdot \frac{c}{2L_0} \tag{3.6}$$

The electromagnetic field from the source measured at position x at time t after n full round trips in cavity is

$$E_{in}(t, x, n) = \sqrt{T} \cdot R^n \cdot A \cdot \exp\left\{ i \left[\omega_0 + \frac{W}{2} \left(t - \xi_n(x, t) \right) \right] \left(t - \xi_n(x, t) \right) \right\} \tag{3.7}$$

where $\xi_n(t)$ is the residence time of wave arrived at coordinate x the time t after n round trips. For the $n = 0$ we define

$$\xi_0(t) = \frac{x}{c} \tag{3.8}$$

The analytical expression for $\xi_n(t, x)$ could be found by use of the recurrent relation between $\xi_n(t)$ and $\xi_{n-1}(t)$ (Fig. 1.19). The difference between the times corresponds to the excess of travelled distance for waves entered cavity in time $t - \xi_n$ and $t - \xi_{n-1}$

$$\xi_n(t) = \xi_{n-1}(t) + 2\frac{L(t_x)}{c} \tag{3.9}$$

where t_x is the moment when the beam who entered the cavity at $t-\xi_n$ reflected on the back mirror. Because both waves exit the cavity in the same moment t we have also $c(t - t_x) = \xi_{n-1} + L(t_x)$ which leads to

$$t_x(t) = \left(t - \xi_{n-1} - \frac{L_0}{c}\right)\left(1 + \frac{v}{c}\right)^{-1} \tag{3.10}$$

By inserting the t_x into 3.9 we can do the following operation with this relation

$$\begin{aligned}
\xi_n(t) &= \xi_{n-1} + \frac{2}{c}\left[L_0 + v\left(t - \xi_{n-1} - \frac{L_0}{c}\right)\left(1 + \frac{v}{c}\right)^{-1}\right] \\
&= \xi_{n-1}\left(1 - 2\frac{v}{c}\frac{1}{1+\frac{v}{c}}\right) + t\left(2\frac{v}{c}\frac{1}{1+\frac{v}{c}}\right) + \frac{2L_0}{c}\left(1 - \frac{v}{c}\frac{1}{1+\frac{v}{c}}\right) \\
&= \xi_{n-1}\left(\frac{1-\frac{v}{c}}{1+\frac{v}{c}}\right) + t\left(2\frac{v}{c}\frac{1}{1+\frac{v}{c}}\right) + \frac{2L_0}{c}\left(\frac{1}{1+\frac{v}{c}}\right) \\
&= \xi_0\left(\frac{1-\frac{v}{c}}{1+\frac{v}{c}}\right)^n + \left\{t\left(2\frac{v}{c}\frac{1}{1+\frac{v}{c}}\right) + \frac{2L_0}{c}\left(\frac{1}{1+\frac{v}{c}}\right)\right\}\sum_{p=0}^{n-1}\left(\frac{1-\frac{v}{c}}{1+\frac{v}{c}}\right)^p
\end{aligned}$$

After the substitution $k = v/c$ and $\gamma = (1-k)/(1+k)$ we obtain the exact formula for $\xi_n(t)$

$$\xi_n(t) = \xi_0\gamma^n + \left[t(1-\gamma) + \frac{2L_0}{c}\frac{1}{1+k}\right]\sum_{p=0}^{n-1}\gamma^p \tag{3.11}$$

Considering cavity tuning speed much smaller that the speed of light we can make the 1st order expansion in k around $k = 0$ ($v/c = 0$) and using the

relations $\gamma'(0) = -2$ and $[\gamma^n]'(0) = -2n$ to obtain

$$\begin{aligned}
\xi_n(t) &= \left(\xi_0 + n\frac{2L_0}{c}\right) + \left\{\xi_0(-2n) + \left[2t - \frac{2L_0}{c}\right]\sum_{p=0}^{n-1} 1 + \left[\frac{2L_0}{c}\right]\sum_{p=0}^{n-1}(-2p)\right\} k \\
&= \xi_0 + n\left[\frac{2L_0}{c} - 2\xi_0 + 2t - \frac{2L_0}{c} + \frac{2L_0}{c}\right] k - \frac{2L_0}{c} k n^2 \\
\xi_n(t) &= \xi_0 + \frac{2}{c}\left\{\left[L_0 + v\left(t - \xi_0 + \frac{L_0}{c}\right)\right] n - \frac{v}{c} L_0 n^2\right\} \qquad (3.12)
\end{aligned}$$

The output electromagnetic field $E_{out}(t)$ at the output mirror ($x = L(t)$) could be evaluated as a sum of all waves leaving the cavity in the time t after different number of round trips

$$E_{out}(t, L(t)) = T \cdot \sum_{n=0}^{\infty} R^n \cdot E_{in}(t, L(t), n) \qquad (3.13)$$

To compare the different cases of tuning we develop the equation 3.13 in the limit cases of $W = 0$ and $v = 0$. When the frequency of source is constant in time we can write

$$\begin{aligned}
E^v_{out}(t, L(t)) &= T \cdot A \cdot \sum_{n=0}^{\infty} R^n \cdot \exp\left\{i\omega_0\left(t - \xi_n(t)\right)\right\} \\
&= T \cdot A \cdot \exp\left\{i\omega_0\left(t - \xi_0\right)\right\} \cdot \\
&\quad \cdot \sum_{n=0}^{\infty} R^n \cdot \exp\left(-i\frac{2\omega_0}{c}\left\{\left[L_0 + v\left(t - \xi_0 + \frac{L_0}{c}\right)\right] n - \frac{v}{c} L_0 n^2\right\}\right)
\end{aligned}$$

using the expression for input field 3.7 we obtain

$$\begin{aligned}
E^v_{out}(t, L(t)) &= T \cdot E_{in}(t, L(t)) \cdot \\
&\quad \cdot \sum_{n=0}^{\infty} R^n \cdot \exp\left(-i\frac{2\omega_0}{c}\left\{\left[L_0 + v\left(t - \frac{L(t) - L_0}{c}\right)\right] n - \frac{v}{c} L_0 n^2\right\}\right)
\end{aligned}$$

Similarly in case of constant cavity length we have

$$\begin{aligned}
E^W_{out}(t, L(t)) &= T \cdot A \cdot \sum_{n=0}^{\infty} R^n \cdot \\
&\quad \cdot \exp\left\{ i \left[\omega_0 + \frac{W}{2} \left(t - \xi_0(t) - n\frac{2L_0}{c} \right) \right] \left(t - \xi_0(t) - n\frac{2L_0}{c} \right) \right\} \\
&= T \cdot A \cdot \sum_{n=0}^{\infty} R^n \cdot \exp\left\{ i \left[\omega_0 + \frac{W}{2} \left(t - \xi_0(t) \right) \right] \left(t - \xi_0(t) \right) \right\} \cdot \\
&\quad \cdot \exp\left\{ i \left[\omega_0 + \frac{W}{2} \left(t - \xi_0(t) \right) \right] \left(-n\frac{2L_0}{c} \right) \right\} \\
&\quad \cdot \exp\left\{ i\frac{W}{2} \left(-n\frac{2L_0}{c} \right) \left(t - \xi_0(t) \right) \right\} \\
&\quad \cdot \exp\left\{ i\frac{W}{2} \left(-n\frac{2L_0}{c} \right)^2 \right\} \\
&= T \cdot A \cdot \exp\left\{ i \left[\omega_0 + \frac{W}{2} \left(t - \xi_0(t) \right) \right] \left(t - \xi_0(t) \right) \right\} \cdot \sum_{n=0}^{\infty} R^n \cdot \\
&\quad \cdot \exp\left(-i\frac{2\omega_0}{c} \left\{ \left[L_0 + W\frac{L_0}{\omega_0} \left(t - \xi_0(t) \right) \right] n - \frac{W}{2}\frac{2L_0}{\omega_0 c} n^2 \right\} \right)
\end{aligned}$$

which gives

$$\begin{aligned}
E^W_{out}(t, L(t)) &= T \cdot E_{in}(t, L(t)) \cdot \\
&\quad \cdot \sum_{n=0}^{\infty} R^n \cdot \exp\left(-i\frac{2\omega_0}{c} \left\{ \left[L_0 + W\frac{L_0}{\omega_0} \left(t - \xi_0(t) \right) \right] n - \frac{W}{2}\frac{2L_0}{\omega_0 c} n^2 \right\} \right)
\end{aligned}$$

The dependencies deduced here are principally the same we can found foe example in [56]. The difference with other works is usually in the sign in the exponent which is due to the definition of input electromagnetic field (wrong combination in the Morville et. all work).

Abreviations

2PS	2nd PoSitive (emission system)
AS	Absorption Spectroscopy
CCD	Charge Coupling Device
CEAS	Cavity Enhanced Spectroscopy
CMOS	Complementary Metal Oxide Semiconductor
CRDS	Cavity Ring-Down Spectroscopy
CW	Continuous Wave
DBD	Dielectric Barrier Discharge
DFB	Distributed Feed-Back
emCCD	electron multiplying Charge Coupling Device
ES	Emission Spectroscopy
FBES	Fast Broadband Emission Spectroscopy
FNSD	Frequency Noise Spectral Density
FTS	Fourier Transform Spectroscopy
FPR	Fabry-Pérot Resonator
HFC	High Finesse Cavity
HIR	Herman infrared
iCCD	intensified Charge Coupling Device
MQW	Multiple Quantum Well
NIR	Near Infra Red (emission system)
NOγ	NOγ (emission system)
OF	Optical Feedback
OPO	Optical Parametric Oscillator
OS	Optical Spectroscopy
PZT	PieZo-electric Transducer
RT	Room Temperature
sCMOS	scientific
SNR	Signal to Noise Ration
S.T.	Schawlow and Townes
UV	Ultra Violet
VECSEL	Vertical External-Cavity Surface-Emitting Laser
VCSEL	Vertical Cavity Surface-Emitting Laser

Bibliography

[1] Digital camera fundamentals, 2006.

[2] Mortimer Abramowitz and Michael W. Davidson. Electronic shutters.

[3] J. Altmann, R. Baumgart, and C. Weitkamp. Two-mirror multipass absorption cell. *Applied Optics*, 20(6):995, 1981.

[4] C. Aragon and J.A. Aguilera. Characterization of laser induced plasmas by optical emission spectroscopy: A review of experiments and methods. *Spectrochimica Acta Part B*, 63:893, 2008.

[5] D.S. Baer, J.B. Paul, M. Gupta, and A. O'Keefe. Sensitive absorption measurements in the near–infrared region using off–axis integrated–cavity output spectroscopy. *Applied Physics B: Lasers and Optics*, 75:261, 2002.

[6] K. H. Becker, U. Kogelschatz, K. H. Schoenbach, and R.J. Barker. *Non-Equilibrium Air Plasmas at Atmospheric Pressure*. Institute of Physics Publishing, 2005.

[7] A. Bogaerts, E. Neyts, R. Gijbels, and J. van der Mullen. Gas discharge plasmas and their applications. *Spectrochimica Acta Part B*, 57:609, 2002.

[8] N. Britun, M. Gaillard, A. Ricard, Y.M. Kim, K.S. Kim, and J. G. Han. Determination of the vibrational, rotational and electron temperatures in N_2 and Ar-N_2 RF discharge. *Journal of Physics D: Applied Physics*, 40:1022, 2007.

[9] L. Cadwell and L. Huwel. Time-resolved emission spectroscopy in laser-generated argon plasmas determination of Stark broadening parame-

ters. *Journal of Quantitative Spectroscopy and Radiative Transfer*, 83:579, 2004.

[10] P. Cermak, J. Varga, P. Macko, V. Martisovits, and P.Veis. Study of nitrogen molecular systems observed in NIR spectra in DBD at near and over atmospheric pressure. In *28th ICPIG, July 15-20, 2007, Prague, Czech Republic*, 2007.

[11] J. H. Choi, J.H. Kim, and Y.S. Hwang. Investigation of the transition between glow and streamer discharges in atmospheric air. *Plasma Sources Science and Technology*, 15:416, 2006.

[12] C. Coates, B. Fowler, and G. Holst. Scientifc CMOS technology a high-performance imaging breakthrough, 2009.

[13] L. A. Coldren and S. W. Corzine. *Diode lasers and Photonic Integrated Circuits*. Wiley, New York, 1995.

[14] P. Connes, J. Connes, L.D. Kaplan, and W.S. Benedict. Carbon monoxide in the Venus atmosphere. *The Astrophysical Journal*, 152:731, 1968.

[15] I. Courtillot, J. Morville, V. Motto-Ros, and D. Romanini. Sub-ppb NO_2 detection by optical feedback cavity-enhanced absorption spectroscopy with a blue diode laser. *Applied Physics B: Lasers and Optics*, 85:407, 2006.

[16] I. Debecker, A. K. Mohamed, and D. Romanini. High-speed cavity ring-down spectroscopy with increased spectral resolution by simultaneous laser and cavity tuning. *Optics Express*, 13(8):2906, 2005.

[17] W. Demtröder. *Laser Spectroscopy: Basic Concepts and Instrumentation, Ed.: 3*. Springer-Verlag, 2002.

[18] L. Deng, X. Gao, Z. Cao, W. Chen, W. Zhang, and Z. Gong. Empirical line intensities of methane at 1.53 μm. *Journal of Quantitative Spectroscopy and Radiative Transfer*, 103(2):402, 2007.

[19] S. Engman, P. Lindblom, and B. Sandberg. An Echelle spectrograph for an image dissector tube with a 100 mm photocathode diameter. *Physica Scripta*, 24:965, 1981.

[20] T.J. Fellers and M.W. Davidson. CCD noise sources and signal-to-noise ratio.

[21] S.E. Fiedler, A. Hese, and A.A. Ruth. Incoherent broad-band cavity-enhanced absorption spectroscopy. *Chemical Physics Letters*, 371:284, 2003.

[22] T. Foldes, P. Cermak, M. Macko, P. Veis, and P. Macko. Cavity ring-down spectroscopy of singlet oxygen generated in microwave plasma. *Chemical Physics Letters*, 467(4-6):233, 2009.

[23] A. Fridman and L.A. Kennedy. *Plasma Physics and Engineering*. Taylor & Francis Books, 2004.

[24] A. Garnache, A. Liu, L. Cerutti, and A. Campargue. Intracavity laser absorption spectroscopy with a vertical external cavity surface emitting laser at 2.3 μm: Application to water and carbon dioxide. *Chemical Physics Letters*, 416:22, 2005.

[25] A. Garnache, A. Ouvrard, L. Cerutti, D. Barat, A. Vicet, F. Genty, Y. Rouillard, D. Romanini, and E. Cerda-Mendez. 2–2.7μm single frequency tunable Sb based lasers operating in CW at RT: Microcavity and external cavity VCSELs, DFB. *Proc. of SPIE*, 6184:61840N, 2006.

[26] A. Garnache, A. Ouvrard, and D. Romanini. Single-frequency operation of external-cavity VCSELs: Non-linear multimode temporal dynamics and quantum limit. *Optics Express*, 15(15):9403, 2007.

[27] F. Genty, L. Cerutti, A. Garnache, A. Ouvrard, A. Pérona, P. Grech, D. Romanini, and F. Chevrier. Room temperature Sb-based mid-infrared vcsels. *Physica status solidi*, 4(5):1591, 2007.

[28] N. Gherardi, Et. Es-Sebbar, C. Sarra-Bournet, N. Naudé, F. Massines, D. Tzyganov, P. Ségur, and S. Pancheshnyi. Active species generation of homogeneous DBD in N_2: experiment and modelling. In *Hakone XI, France*, 2008.

[29] N. Gherardi, G. Gouda, E. Gat, A. Ricard, and F. Massines. Transition from glow silent discharge to micro-discharges in nitrogen gas. *Plasma Sources Science and Technology*, 9(3):340, 2000.

[30] F. R. Gilmore and R. R. Laher. Franck-Condon factors, r-centroids, electronic transition moments, and einstein coefficients for many nitrogen and oxygen band systems. *Journal of Physical and Chemical Reference Data*, 21:1005, 1992.

[31] H.R. Griem. *Spectral Line Broadening by Plasmas*. Academic Press, 1974.

[32] G.R. Harrison. The production of diffraction gratings: II. The design of echelle gratings and spectrographs. *Journal of the Optical Society of America*, 39:522, 1949.

[33] D. Herriot, H. Kogelnik, and R. Kompfner. Off-axis paths in spherical mirror interferometers. *Applied Optics*, 3(4):523, 1964.

[34] Haifeng Huang and Kevin K. Lehmann. Effects of linear birefringence and polarization-dependent loss of supermirrors in cavity ring-down spectroscopy. *Applied Optics*, 47(21):3817, 2008.

[35] K. Iga. Surface emitting lasers. *Electronics and Communications in Japan (Part II: Electronics)*, 82(10):70, 1999.

[36] L.D. Kaplan, J. Connes, and P. Connes. Carbon monoxide in the martian atmosphere. *The Astrophysical Journal*, 157:187, 1969.

[37] S. Kassi, M. Chenevier, L. Gianfrani, A. Salhi, Y. Rouillard, A. Ouvrard, and D. Romanini. Looking into the volcano with a Mid-IR DFB diode laser and cavity enhanced absorption spectroscopy. *Optics Express*, 14(23):11442, 2006.

[38] E.R.T. Kerstel, R.Q. Iannone, M. Chenevier, S. Kassi, H.J. Jost, and D. Romanini. A water isotope (^{2}H, ^{17}O, and ^{18}O) spectrometer based on optical feedback cavity–enhanced absorption for in situ airborne applications. *Applied Physics B: Lasers and Optics*, 85:397, 2006.

[39] J. T. Kiehl and Kevin E. Trenberth. Earth's annual global mean energy budget. *Bulletin of the American Meteorological Society*, 78:197, 1997.

[40] J.W. Kim, J.W. Hahn, Y.S. Yoo, J.Y. Lee, H.J. Kong, and H.W. Lee. Measurement of the linewidth of a continuous-wave laser with a cavity-length modulation technique. *Applied Optics*, 38:1742, 1999.

[41] R. R. Laher and F. R. Gilmore. Improved fits for the vibrational and rotational constants of many states of nitrogen and oxygen. *Journal of Physical and Chemical Reference Data*, 20:685, 1991.

[42] A. Laurain, M. Myara, G. Beaudoin, I. Sagnes, and A. Garnache. Multiwatt-power highly-coherent compact single-frequency tunable vertical-external-cavity-surface-emitting-semiconductor-laser. *Optics Express*, 18(14):14627, 2010.

[43] P. Laurent, A. Clairon, and C. Breant. Frequency noise analysis of opticallly self-locked diode lasers. *IEEE Journal of Quantum Electronics*, 25(6):1131, 1989.

[44] K. K. Lehmann. Ring down cavity spectroscopy cell using continuous wave excitation for trace species detection., 1996.

[45] K. K. Lehmann and D. Romanini. The superposition principle and cavity ring down spectroscopy. *Journal of Chemical Physics*, 105:10263, 1996.

[46] C. Lin, M. Grau, O. Dier, and M.-C. Amann. Low threshold room-temperature continuous-wave operation of 2.24–3.04 μm GaInAsSb/AlGaAsSb quantum-well lasers. *Applied Physics Letters*, 84(25):5088–5090, 2004.

[47] Peter Lindblom. New compact Echelle spectrographs with multichannel time-resolved recording capabilities. *Analytica Chimica Acta*, 380:353, 1999.

[48] Erwin Loewen and Christopher Palmer. *Difraction Grating Handbook sixth edition.* Newport Corporation, 2005.

[49] E. Marcq, B. Bezard, P. Drossart, G. Piccioni, and VIRTIS Team. Variability of CO, OCS and H_2O below the clouds of Venus from VIRTIS-H night-side spectra. *Bulletin of the American Meteorological Society*, 39:503, 2007.

[50] F. Massines, N. Gherardi, A. Fornelli, and S. Martin. Atmospheric pressure plasma deposition of thin films by Townsend dielectric barrier discharge. *Surface and Coatings Technology*, 200:1855, 2005.

[51] F. Massines, N. Gherardi, N. Naude, and P. Segur. Recent advances in the understanding of homogeneous dielectric barrier discharges. In *Hakone XI, France*, 2008.

[52] F. Massines, A. Rabehi, P. Decomps, R. Ben Gadri, P. Segur, and C. Mayoux. Experimental and theoretical study of a glow discharge at atmospheric pressure controlled by dielectric barrier. *Journal of Applied Physics*, 83:2950, 1998.

[53] F. Massines, P. Segur, N. Gherardi, C. Khamphan, and A. Ricard. Physics and chemistry in a glow dielectric barrier discharge at atmospheric pressure: diagnostics and modelling. *Surface and Coatings Technology*, 174-175:8, 2003.

[54] L. Matone, M. Barsuglia, F. Bondu, F. Cavalier, H. Heitmann, and N. Man. Finesse and mirror speed measurement for a suspended Fabry-Perot cavity using the ringing effect. *Physics Letters A*, 271:314, 2000.

[55] J. Morville, S. Kassi, M. Chenevier, and D. Romanini. Fast, low-noise,

mode-by-mode, cavity-enhanced absorption spectroscopy by diode-laser self-locking. *Applied Physics B: Lasers and Optics*, 80:1027, 2005.

[56] J. Morville, D. Romanini, M. Chenevier, and A. Kachanov. Effects of laser phase noise on the injection of a high-finesse cavity. *Applied Optics*, 41:6980, 2002.

[57] J. Morville, D. Romanini, A. Kachanov, and M. Chenevier. Two schemes for trace detection using cavity ring-down spectroscopy. *Applied Physics B: Lasers and Optics*, 78:465, 2004.

[58] V. Motto-Ros, M. Durand, and J. Morville. Extensive characterization of the optical feedback cavity enhanced absorption spectroscopy (OF-CEAS) technique: ringdown-time calibration of the absorption scale. *Applied Physics B: Lasers and Optics*, 91:203, 2008.

[59] V. Motto-Ros, J. Morville, and P. Rairoux. Mode–by–mode optical feedback: cavity ringdown spectroscopy. *Applied Physics B: Lasers and Optics*, 87:531, 2007.

[60] H. Nassar, S. Pellerin, K. Musiol, O. Martinie, N. Pellerin, and J.-M. Cormier. N_2^+/N_2 ratio and temperature measurements based on the first negative N_2^+ and second positive N_2 overlapped molecular emission spectra. *Journal of Physics D: Applied Physics*, 37:1904, 2004.

[61] A. O'Keefe and D. A. G. Deacon. Cavity ringŰdown optical spectrometer for absorption measurements using pulsed laser sources. *Review of Scientific Instruments*, 59:2544, 1988.

[62] A. Ouvrard, L. Cerutti, and A. Garnache. Broad continuous tunable range with single frequency Sb-based external-cavity VCSEL emitting in MIR. *Electronics letters*, 45(12):629, 2009.

[63] A. Ouvrard, A. Garnache, L. Cerutti, F. Genty, and D. Romanini. Single-frequency tunable Sb-based VCSELs emitting at 2.3 μm. *IEEE Photonics Technology Letters*, 17(10):2020, 2005.

[64] H. Partridge, S.R. Langhoff, Ch.W. Bauschlincer Jr., and D.W. Schwenke. Theoretical study of the $A'\,^5\Sigma_g^+$ and $C''\,^5\Pi_u$ states of N_2 – implications for the N_2 afterglow. *Journal of Chemical Physics*, 88:3174, 1988.

[65] J. B. Paul, L. Lapson, and J. G. Anderson. Ultrasensitive absorption spectroscopy with a high-finesse optical cavity and off-axis alignment. *Applied Optics*, 40:4904, 2001.

[66] S. S. Penner. *Quantitative Molecular Spectroscopy and Gas Emissivities*. Addison-Wesley, Reading, MA, 1959.

[67] K. Petermann. *Laser Diode Modulation and Noise*. Kluwer Scientific, Tokio, 1991.

[68] J. Poirson, F. Bretenaker, M. Vallet, and A.L. Floch. Analytical and experimental study of ringing effects in a Fabry-Perot cavity. Application to the measurement of high finesses. *Journal of the Optical Society of America B*, 14:2811, 1997.

[69] Yu. Ralchenko, A.E. Kramida, J. Reader, and NIST ASD Team. Nist atomic spectra database (version 3.1.5), 2008. National Institute of Standards and Technology, Gaithersburg, MD.

[70] A. R. Ravishankara, J. S. Daniel, and R. W. Portmann. Nitrous oxide (n_2o): The dominant ozone-depleting substance emitted in the 21st century. *Science*, 326(5949):123, 2009.

[71] C. Robert. Simple, stable, and compact multiple-reflection optical cell for very long optical paths. *Applied Optics*, 46(22):5408, 2007.

[72] D. Romanini, M. Chenevier, S. Kassi, M. Schmidt, C. Valant, M. Ramonet, J. Lopez, and H.-J. Jost. Optical-feedback cavity-enhanced absorption: a compact spectrometer for real-time measurement of atmospheric methane. *Applied Physics B: Lasers and Optics*, 83(4):659, 2006.

[73] D. Romanini, A. A. Kachanov, N. Sadeghi, and F. Stoeckel. CW-cavity ring down spectroscopy. *Chemical Physics Letters*, 264:316, 1997.

[74] D. Romanini, A. A. Kachanov, and F. Stoeckel. Diode laser cavity ring down spectroscopy. *Chemical Physics Letters*, 270:538, 1997.

[75] L. S. ROTHMAN, C. P. RINSLAND, A. GOLDMAN, S. T. MASSIE, D. P. EDWARDS, J-M. FLAUD, A. PERRIN, C. CAMY-PEYRET, V. DANA, J. Y. MANDIN, J. SCHROEDER, A. MCCANN, R. R. GAMACHE, R. B. WATTSON, K. YOSHINO, K. V. CHANCE, K. W. JUCKS, L. R. BROWN, V. NEMTCHINOV, and P. VARANASI. The HITRAN molecular spectroscopic database and HAWKS (HITRAN atmospheric workstation): 1996 edition. *Journal of Quantitative Spectroscopy and Radiative Transfer*, 60(5):665 – 710, 1998.

[76] L.S. Rothman, I.E. Gordon, A. Barbe, D.Chris Benner, P.F. Bernath, M. Birk, V. Boudon, L.R. Brown, A. Campargue, J.-P. Champion, K. Chance, L.H. Coudert, V. Dana, V.M. Devi, S. Fally, J.-M. Flaud, R.R. Gamache, A. Goldman, D. Jacquemart, I. Kleiner, N. Lacome, W.J. Lafferty, J.-Y. Mandin, S.T. Massie, S.N. Mikhailenko, C.E. Miller, N. Moazzen-Ahmadi, O.V. Naumenko, A.V. Nikitin, J. Orphal, V.I. Perevalov, A. Perrin, A. Predoi-Cross, C.P. Rinsland, M. Rotger, M. Simecková, M.A.H. Smith, K. Sung, S.A. Tashkun, J. Tennyson, R.A. Toth, A.C. Vandaele, and J. Vander Auwera. The HITRAN 2008 molecular spectroscopic database. *Journal of Quantitative Spectroscopy and Radiative Transfer*, 110(9-10):533 – 572, 2009. HITRAN.

[77] M. Sabsabi, R.Heon, and L. St-Onge. Critical evaluation of gated CCD detectors for laser-induced breakdown spectroscopy analysis. *Spectrochimica Acta Part B*, 60:1211, 2005.

[78] A. L. Schawlow and C. H. Townes. Infrared and optical masers. *Physical Review*, 112:1940, 1958.

[79] Nicola Schulz, Marcel Rattunde, Christian Ritzenthaler, Benno Rosener, Christian Manz, Klaus Kohler, Joachim Wagner, and Uwe Brauch. Resonant optical in-well pumping of an (AlGaIn)(AsSb)-based vertical-

external-cavity surface-emitting laser emitting at 2.35 μm. *Applied Physics Letters*, 91(9):091113, 2007.

[80] M. Simek. Determination of $N_2(A\ ^3\Sigma_u^+)$ metastable density produced by nitrogen streamers at atmospheric pressure: 1. Design of diagnostic method. *Plasma Sources Science and Technology*, 12:421, 2003.

[81] M. Simek. Determination of $N_2(A\ ^3\Sigma_u^+)$ metastable density produced by nitrogen streamers at atmospheric pressure: 2. Experimental verification. *Plasma Sources Science and Technology*, 12:454, 2003.

[82] M. Simek, V. Babicky, M . Clupek, and Pavel Sunka. Observation of the N_2 Herman infrared system in pulsed positive streamer induced emission at atmospheric pressure. *Journal of Physics D: Applied Physics*, 34:3185, 2001.

[83] K. Sunga and P. Varanasi. CO_2-broadened half-widths and CO_2-induced line shifts of $^{12}C^{16}O$ relevant to the atmospheric spectra of Venus and Mars. *Journal of Quantitative Spectroscopy and Radiative Transfer*, 91:319, 2005.

[84] Z. Tan and X. Long. Off-axis integrated cavity output spectroscopy and its application. *Optics Communications*, 283:1406, 2010.

[85] S. A. Tashkun, V. I. Perevalov, and J. L. Teffo. *Remote Sensing of the Atmosphere for Environmental Security*, chapter CDSD-296, The High-Precision Carbon Dioxide Spectroscopic Databank: Version for Atmospheric Applications, pages 161–169. Springer Netherlands, 2007.

[86] M. V. Tonkov, N. N. Filippov, V. V. Bertsev, J. P. Bouanich, Nguyen Van-Thanh, C. Brodbeck, J. M. Hartmann, C. Boulet, F. Thibault, and R. Le Doucen. Measurements and empirical modeling of pure CO_2 absorption in the 2.3-μm region at room temperature: far wings, allowed and collision-induced bands. *Applied Optics*, 35(24):4863, 1996.

[87] M. Triki, P. Cermak, G. Mejean, and D. Romanini. Cavity-enhanced absorption spectroscopy with a red LED source for NOx trace analysis. *Applied Physics B: Lasers and Optics*, 91(1):195, 2008.

[88] G. W. Turner, H. K. Choi, and M. J. Manfra. Ultralow-threshold (50 A/cm[sup 2]) strained single-quantum-well GaInAsSb/AlGaAsSb lasers emitting at 2.05 μm. *Applied Physics Letters*, 72(8):876–878, 1998.

[89] S. Voigt, J. Orphal, and J. Burrows. The temperature and pressure dependence of the absorption cross-sections of NO_2 in the 250-800 nm region measured by Fourier-transform spectroscopy. *Journal of Photochemistry and Photobiology A: Chemistry*, 149:1, 2002.

[90] H.-E. Wagner, R. Brandenburg, K. V. Kozlov, A. Sonnenfeld, P. Michel, and J. F. Behnke. The barrier discharge: basic properties and applications to surface treatment. *Vacuum*, 71(3):417 – 436, 2003. Symposium on Plasma Surface Engineering at the Spring Meeting of the German Physical Society, Regensburg, Germany, March 11-15 2002.

[91] L. Wang, V.I. Perevalov, S.A. Tashkun, Y. Ding, and S.M. Hu. Absolute line intensities of $^{13}C^{16}O_2$ in the 4200-8500 cm^{-1} region. *Journal of Molecular Spectroscopy*, 234:84, 2005.

[92] P. Werle and F. Slemr. Signal-to-noise ratio analysis in laser absorption spectrometers using optical multipass cells. *Applied Optics*, 30(4):430, 1991.

[93] J. White. Long optical paths of large aperture. *Journal of the Optical Society of America*, 32(5):285, 1942.

[94] C. Wichaidit and W.N.G. Hitchon. Enhanced performance of light-emitting diodes based on a nanocomposite of dehydrated nanotube titanic acid and poly(vinylcarbazole) (PVK). *Physics Letters A*, 335(1):50, 2005.

[95] S. Williams, M. Gupta, T. Owano, D.S. Baer, A. O'Keefe, D. R. Yarkony,

and S. Matsika. Quantitative detection of singlet O_2 by cavity-enhanced absorption. *Optics Letters*, 29(10):1066, 2004.

Title

High sensitivity optical spectroscopy of plasma and gases

Abstract

The project of this thesis was developed as a joint supervision project between the Department of Experimental Physics at Comenius University in Bratislava and Laboratoire de Spectrometrie Physique at Joseph Fourier University in Grenoble. The aim of the project is the development and application of some of these new spectroscopic methods for the study and diagnostics of gases and plasma. In Bratislava the work under the supervision of prof. Pavel Veis and Doc. Peter Macko was oriented towards the optical diagnostics of plasma environments. Beside the principal experiments concerning the dielectric barrier discharge (DBD) and production of the singlet oxygen state, the goal was to develop spectroscopic methods capable of providing physical measurements related to this applications. In the DBD the interest was focused on the description of the excited electronic states population variations during the period of discharge. We used fast broad–band emission spectroscopy (FEBS) comprising the instrument and data treatment process to achieve this goal. In case of singlet oxygen production we developed a Cavity ring–down spectrometer (CRDS) to detect the singlet oxygen by its infrared absorption in the microwave plasma afterglow. In Grenoble under the supervision of Dr. Daniele Romanini the principal line of work consisted in the development of a new laser source - Vertical external cavity surface emitting laser (VECSEL) and its application to absorption spectroscopy. The work was held in collaboration with the Institude d'electronique du Sud in the frame of the joint ANR MIREV project. A period was also dedicated to the developing of a small, fast, robust and low-cost NO_2 and NO_3 detector based on the Incoherent broad–band cavity enhanced absorption spectroscopy (IBB–CEAS).

Key-words

high finesse optical cavity - absorption laser spectroscopy - optical-feedback - semiconductor laser - dielectric barrier discharge - emission spectroscopy.

Titre

Spectroscopie optique de haute sensibilité dans les plasmas et les gazes

Résumé

Le travail de thèse a été réalisé dans le cadre d'une cotutelle entre le Département de Physique Expérimental à l'Université Comenius à Bratislava et Laboratoire de Spectrométrie Physique à l'Université Joseph Fourier à Grenoble. Le but de la thèse était le développement et l'application de nouvelles méthodes spectroscopiques pour l'analyse de plasma et de gaz. A Bratislava, mon travail était supervisé par le prof. Pevel Veis et le Doc. Peter Macko . Il s'est orienté vers le diagnostique optique de plasma. Mon travail principal a été d'étudier le comportement de la décharge à barrière diélectrique(DBD) ainsi que la production d'oxygène dans l'état singulet. En parallèle, j'ai développé des méthodes de mesures des propriétés physiques liées à cette expérience. Dans le DBD, l'objectif était d'écrire l'évolution temporelle des états électroniques excités au cours de la décharge. La méthode utilisée était la spectroscopie rapide et large bande. Mon travail a consisté à mettre en place l'instrumentation ainsi que les algorithmes pour le traitement de données. Concernant l'étude de la production de l'oxygène singulet, on a développé un système CRDS (Cavity-Ring-Down Spectroscopy) capable de le détecter dans la post-décharge de plasma. A Grenoble, sous la supervision du Dr. Daniele Romanini, l'objectif principal de mon travail a consisté dans le développement d'une nouvelle source laser - Vertical External Cavity Surface Emitting Laser (VECSEL) et son application dans la spectroscopie d'absorption. Le travail a été réalisé en collaboration avec l'Institut d'électronique du Sud dans le cadre du projet ANR MIREV. En plus de ce travail, j'ai participé au développement d'un détecteur portable et bon marché pour l'analyse quantitative de NO_2 et NO_3 dans l'atmosphère par la technique Incoherent Broadband Cavity Enhanced Absorption Spectroscopy.

Mots clefs

cavité optique de haute finesse - spectroscopie d'absorption laser - rétroaction optique - laser semiconducteur - décharge à barriere dielectrique - spectroscopie d'emission.